Dynamic nuclear polarization in solids and diffusion in liquids

Behdad Aghelnejad

PSL UNIVERSITÉ PARIS

THÈSE DE DOCTORAT
DE L'UNIVERSITÉ PSL

Préparée à l'École Normale Supérieure (ENS)-Paris

Dynamic nuclear polarization in solids and diffusion in liquids

Polarisation nucléaire dynamique dans les solides et diffusion dans les liquides

Soutenue par
Behdad AGHELNEJAD
Le 20 mai 2021

Ecole doctorale n° 388
Chimie Physique et Chimie Analytique de Paris-Centre

Spécialité
La spectroscopie par résonance magnétique nucléaire (RMN)

Composition du jury :

Nicolas, GIRAUD Professeur Université de Paris	*Président*
Charlotte, MARTINEAU Maître de conférences Institut Lavoisier de Versailles (ILV)	*Rapporteur*
Patrick, BERTHAULT Directeur de recherche CEA & Université Paris Saclay	*Rapporteur*
Martial, PIOTTO Responsable des projets collaboratifs Bruker France	*Examinateur*
Pierre-Jean, NACHER Directeur de recherche École Normale Supérieure-Paris	*Examinateur*
Anne-laure, ROLLET Chargé de recherche Sorbonne Université	*Examinateur*
Geoffrey, BODENHAUSEN Professeur émérite École Normale Supérieure-Paris	*Directeur de thèse*
Philippe, PELUPESSY Ingénieur de recherche École Normale Supérieure-Paris	Co-*directeur de thèse*

ENS ÉCOLE NORMALE SUPÉRIEURE — PSL RESEARCH UNIVERSITY PARIS

Dynamic nuclear polarization in solids and diffusion in liquids

PhD thesis

Written by: Behdad Aghelnejad

Supervisor: Prof. Geoffrey Bodenhausen

Co-supervisor: Dr. Philippe Pelupessy

Laboratoire des Biomolécules (LBM), UMR 7203

Département de Chimie

École Normale Supérieure Paris

Table of Contents

Acknowledgements

I would like to start by thanking my PhD supervisor and co-supervisor at ENS, Prof. Geoffrey Bodenhausen and Dr. Philippe Pelupessy. They spent so much time teaching me. Our discussions always aided me to move forward in my research. They supported me and every time that I asked them for any kind of help, they graciously helped me. This research would not have been possible without their guidance.

I also had two supervisors at Bruker. I would like to express my gratitude to Dr. James Kempf and Dr. Fabien Aussenac. They were always there for me if I needed anything. They were in contact with me during my PhD. They followed my progress closely and gave my many ideas during our discussions.

I would like to thank Dr. Dennis Kurzbach who was my co-supervisor at the beginning of my thesis and I learned a lot from him. I thank Dr. Daniel Abergel, our group leader, who I also learned from.

This research is not just the result of my work. I wish to acknowledge the support of all my group members at ENS Paris. However, I have to thank some of my colleagues specifically because of their direct involvement in parts of my thesis.

I built a d-DNP probe with the help of Dr. Sina Marhabaie. He was my partner from the beginning when we came up with the idea of building the probe until the end when it was operational and half of the credit goes to him. I would also thank David le Gallo who provided us with the technical assistance that we needed.

The spin thermometry project would not have been possible without Dr. Diego Carnevale. I went to him and asked for his expertise in solid-state NMR. He led us through the whole project and he thought me a lot while doing that. I would like to express my sincerest gratitude to him.

A huge thanks to Dr. Nicolas Birlirakis who was indispensable during the course of building the magnetic tunnel. He performed essential simulations and provided me with plenty of ideas during our discussions.

I wish to thank Dr. Mathieu Baudin for his crucial role in building a control unit for our system. He was involved in the planning, assembling, and operating the control unit and provided me with much needed consult every time I needed it.

I thank Karen Dos Santos for helping me perform most of the dissolution experiments and always encouraging me with her new ideas. I also thank David Guarin for our discussions and the suggestions he made every time that I encountered new problems during my experiments.

I express my deepest gratitude and appreciation for my parents, my brother, and my friends who always supported me. I am particularly grateful to Bahar for all she has done for me. I couldn't have gone through this stage of my life without her unconditional support.

This work was made possible thanks to the support of Bruker Biospin France and the ANRT (contract CIFRE no 2017/1489).

Finally, I thank all the members of the jury for taking the time to read this thesis and participate in my defense.

Abstract

Nuclear magnetic resonance (NMR) spectroscopy is a powerful technique that has the capability to characterize a wide variety of molecules and can give insights into chemical processes. However, this spectroscopic method suffers from a lack of sensitivity. Dissolution dynamic nuclear polarization (d-DNP) is currently at the core of many new developments in view of boosting the sensitivity of NMR.

D-DNP probes are usually designed for one or at most two specific nuclei. Investigations of multiple nuclei usually requires manufacturing a number of costly probes. In addition, changing the probe is a time-consuming process since a system that works at low temperatures (usually between 1.2 and 4.2 K) must be warmed up, thus increasing the risks of contamination. Here, an efficient apparatus is described for d-DNP, designed not only for microwave-enhanced direct observation of a wide range of nuclei S such as ^{1}H, ^{13}C, ^{2}H, ^{23}Na, and ^{17}O, but also for cross-polarization (CP) from I = ^{1}H to such S nuclei. Unlike most conventional designs, the tuning and matching circuits are partly immersed in superfluid helium at temperatures down to 1.2 K. Intense radio-frequency (rf) fields with amplitudes on the order of 50 kHz or better can be applied simultaneously to both nuclei I and S using rf amplifiers with powers on the order of 90 W.

This probe is ideally made for “bullet-DNP” which is a new d-DNP method that has recently been gaining importance. In this method, a polarized sample is transferred to a spectrometer in the solid state and dissolved after the transfer, rather than being dissolved in the polarizer, as in conventional dissolution DNP. The bullet-DNP setup has the advantage of significantly decreasing the dilution factor and provides the possibility to use organic solvents for dissolution. This setup is developed further with the development of a contamination-free insert and fast ejection of the sample, the construction of a magnetic tunnel with a homogeneous field near 0.34 T to preserve the polarization during the transfer of the solid sample from the polarizer to the spectrometer, and the beginning of the assembly of an efficient dissolution system to dissolve the bullets with adjustable amounts of liquid in the bore of the spectrometer magnet.

Dynamic nuclear polarization of samples at low temperatures, typically between 1.2 and 4.2 K, allows one to achieve spin temperatures as low as 2 mK, so that for many nuclear isotopes the high-temperature approximation is violated for the nuclear Zeeman interaction. This leads to characteristic asymmetries in powder spectra. We show that the line shapes due to the quadrupolar couplings of deuterium spins present in virtually all solvents used for such experiments (‘DNP juice’) allows the quick yet accurate determination of the deuterium spin temperature or, equivalently, the deuterium polarization. The observation of quadrupolar echoes excited by small flip-angle pulses allows one to monitor the build-up and decay of the positive or negative deuterium polarization.

NMR is established as one of the most potent methods of measuring self-diffusion coefficients (D) which is an important transport parameter of molecules in liquids. An alternative method is put forward as a proof of concept in which the diffusion process is followed directly by recording 1D images at different intervals. While this method is not meant to replace established methods of measuring diffusion, it exploits a simple idea which results in consistent diffusion coefficients obtained at different temperatures for H_2O and DMSO.

Résumé en français

Partie A: le nouveau système d-DNP

La spectroscopie par résonance magnétique nucléaire (RMN) est une méthode puissante qui peut donner un aperçu de processus chimiques et qui a la capacité de caractériser une grande variété de molécules. La simplicité de la préparation, l'absence de dommages aux échantillons et les volumes modérés d'échantillons nécessaires sont parmi les raisons importantes qui font de la RMN une méthode de spectroscopie largement utilisée. Bien que la technique soit très puissante, la RMN souffre d'un manque de sensibilité. Il existe plusieurs méthodes pour améliorer la sensibilité de la RMN. L'un des moyens les plus puissants pour augmenter la sensibilité de la RMN est la polarisation nucléaire dynamique (DNP pour *dynamic nuclear polarization*) qui est au cœur de ce travail.

La DNP consiste à transférer la polarisation des spins électroniques qui est élevée (l'électron ayant un rapport gyromagnétique d'environ 660 fois plus grand que celui des protons) vers les spins nucléaires à l'aide d'une irradiation par micro-ondes, ce qui conduit à une amélioration substantielle de la polarisation nucléaire et donc à une augmentation de la sensibilité de la spectroscopie RMN.

L'une des grandes avancées dans le domaine de la DNP s'est produite en 2003 où le travail d'Ardenkjær-Larsen *et al.* [1] a démontré que l'hyperpolarisation peut survivre à un saut de température causé par la dissolution rapide d'un échantillon congelé à des températures d'hélium liquide ($1{,}2 < T < 4{,}2$ K) suivie d'une acquisition de signal à l'état de solution (généralement > 300 K) qui donne des gains de sensibilité qui peuvent être aussi élevés que 10^4. Ce procédé, appelé dissolution-DNP (d-DNP), fait actuellement l'objet de nombreux efforts en vue d'augmenter la sensibilité de la RMN et de l'imagerie par résonance magnétique (IRM).

Dans les expériences d-DNP, les échantillons contenant les molécules cibles sont dopés avec des radicaux ou d'autres agents polarisants (AP) paramagnétiques. L'amélioration est générée par un transfert de la polarisation électronique élevée des AP vers les spins nucléaires cibles via une irradiation micro-ondes à basse température ($1{,}2 < T < 4{,}2$ K) et dans des champs magnétiques élevés (généralement $3{,}35 < B_0 < 10$ T). L'échantillon est ensuite rapidement dissous et transféré à l'état liquide vers un spectromètre RMN. À ce stade, tout programme d'impulsions RMN à l'état liquide peut être appliqué pour la détection, à condition qu'il soit terminé avant que les noyaux hyperpolarisés ne reviennent à l'équilibre thermique.

Cette méthode est bien établie et elle est aujourd'hui mise en œuvre dans de nombreux laboratoires. L'un de ses principaux avantages est que la solution contenant la substance hyperpolarisée subit des temps de relaxation T_1 relativement longs pendant le transfert (qui dure environ 10 s). Ceci est obtenu grâce au facteur de dilution élevé d'environ 100x. La dilution

augmente la distance moyenne entre les radicaux et les noyaux. Cela augmente le temps de relaxation T_1 car les interactions dipolaires entre les radicaux et les noyaux sont la principale source de relaxation lors du transfert. Cependant, le facteur de dilution élevé mentionné et la perte de sensibilité qui l'accompagne sont indésirables dans de nombreux cas, comme pour les substances biologiques, et peut être compté comme l'un des principaux inconvénients de la d-DNP. Un autre gros inconvénient de cette méthode est la limitation des solvants. Par exemple, on ne peut pas utiliser de solvants organiques pour la dissolution car un solvant organique à haute température (*ca.* 180 °C) sous pression (*ca.* 1 MPa) risque d'endommager la « cocotte minute ». Par ailleurs, la capacité thermique des solvants organiques n'est pas suffisante pour dissoudre les échantillons congelés dans le polariseur.

Récemment, une autre méthode a été développée qui surmonte ces inconvénients et est appelée DNP « par projectile » (*bullet* DNP). Dans cette méthode qui a été introduite par Benno Meier et *al.* [2], le solide hyperpolarisé est transféré dans un spectromètre où il est fondu et dissous à température ambiante avant détection.

Un projectile contenant l'échantillon congelé et hyperpolarisé est éjectée à l'aide d'hélium gazeux sous pression. Un champ magnétique d'au moins 0,1 T doit être maintenu tout au long du trajet depuis le polariseur jusqu'au spectromètre pour limiter la relaxation à faible champ induite par les radicaux. Benno Meier et *al.* [2] ont proposé à cet effet l'usage d'un solénoïde, enroulé le long de la totalité du trajet de transfert, mais on peut utiliser n'importe quelle construction telle qu'un tunnel magnétique avec des aimants permanents, similaire à ce qui a été décrit précédemment. Transférer le projectile très rapidement, et éviter à tout prix un passage par des bas champs, sont des éléments cruciaux de ce système, bien plus que dans la d-DNP traditionnelle. Cela est dû au fait que les radicaux et les noyaux hyperpolarisés sont proches dans un solide compact (d'un volume de 10-50 µL) qui rend la relaxation T_1 provoquée par les interactions dipolaires d'autant plus efficace. Le temps de relaxation T_1 pendant le transfert est d'environ 1 s. Le transfert est ensuite suivi d'une dissolution rapide et homogène avant détection dans le spectromètre. La conception et la mise en œuvre d'un tel système à partir de zéro est la partie principale de ce travail de thèse.

Les principaux avantages du système DNP par projectile sont le contrôle du facteur de dilution qui peut être aussi bas qu'un facteur 10 et la possibilité d'utiliser divers solvants aqueux ou organiques pour la dissolution. Ces avantages ouvrent de nouvelles possibilités d'utilisation de la d-DNP pour des échantillons qui ne sont pas compatibles avec les configurations traditionnelles. Par exemple, il permet d'effectuer le d-DNP sur une large gamme de polymères qui ne sont pas solubles dans l'eau mais peuvent être dissous dans des solvants organiques.

Outre le circuit radio-fréquence (rf), une sonde d-DNP doit être adaptée à l'insertion et à l'éjection d'un projectile tout en restant à basse température. Étant donné que nos sondes d-DNP conventionnelles ne sont pas compatibles pour l'insertion et l'éjection d'échantillons solides, il a donc fallu construire une autre sonde adaptée à un tel système. Les sondes D-DNP sont généralement conçues pour un noyau, ou tout au plus deux noyaux spécifiques. L'étude de

plusieurs noyaux nécessite généralement la fabrication de plusieurs sondes coûteuses. De plus, le changement de sonde est un processus qui prend du temps car un système fonctionnant à basse température doit être réchauffé, augmentant ainsi les risques de contamination.

Dans cette thèse, nous décrivons une sonde large bande ^{1}H-X à double résonance adaptée pour un système DNP par projectile. Le canal X peut couvrir une gamme de noyaux de ^{15}N à ^{23}Na (c'est-à-dire de 28,9 à 75,5 MHz à 6,7 T). Cette sonde permet non seulement d'observer l'accumulation de la polarisation « directe » sur les deux canaux, mais également d'effectuer la polarisation croisée (CP pour *cross-polarization*) entre ^{1}H et tout autre noyau accessible au canal X. Cette sonde est équipée d'une bobine rf horizontale pour générer un champ magnétique B_1 homogène. Contrairement à la plupart des configurations conventionnelles qui ont au moins quelques condensateurs à l'extérieur du polariseur pour le réglage fin de l'accord et de l'adaptation, dans notre cas, le circuit rf tout entier est immergé dans le cryostat à basse température à l'intérieur du polariseur. Les condensateurs et les inductions peuvent être ajustés par des tiges en laiton à partir du haut du cryostat. Habituellement, dans d'autres conceptions, on ne peut changer la fréquence rf que sur une plage d'environ 6 MHz pour compenser les petits changements d'accord qui peuvent se produire lors du changement d'échantillons avec des susceptibilités différentes. Avec la conception actuelle, nous avons réussi à régler le canal X sur une très large plage de 50 MHz, fournissant ainsi une sonde unique d-DNP pour une large bande de fréquences à basse température. De plus, en déplaçant diverses parties du circuit rf depuis haut de la sonde vers le cœur du cryostat, les pertes d'énergie sont considérablement réduites, de sorte que des longueurs d'impulsion plus courtes peuvent être obtenues avec moins de puissance rf. Des champs rf intenses avec des amplitudes de l'ordre de 50 kHz ou mieux peuvent être appliqués simultanément aux noyaux I (^{1}H) et X en utilisant des amplificateurs rf avec des puissances de l'ordre de 90 et 80 W respectivement.

La Figure 1 montre la détection de différents noyaux dans un échantillon contenant 50% d'éthanol-d_6, 40% D_2O, 10% $H_2{}^{17}O$ avec 1,5 M d'acétate de sodium (enrichi en ^{13}C à 99% dans la position carboxylique), 1 M d'urée (enrichi en ^{15}N à 98%) et 40 mM de TEMPOL. L'échantillon a été placé dans la bobine et vitrifié à 4 K, et tous les spectres ont été enregistrés l'un après l'autre, simplement en accordant pour les fréquences souhaitées. Les spectres en rouge ont été obtenus sans micro-ondes, les spectres en noir avec DNP positif et les spectres en bleu avec DNP négatif.

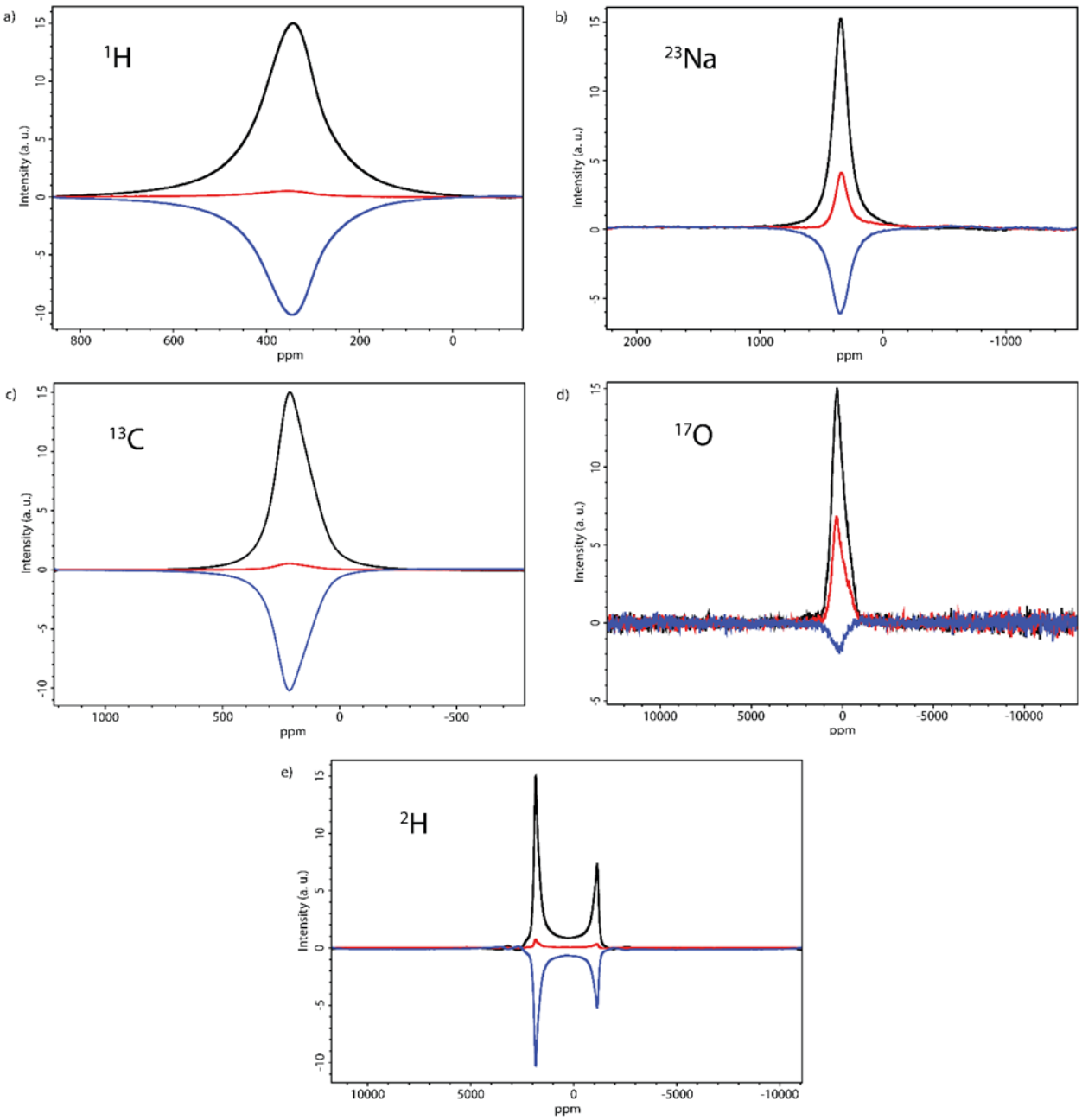

Figure 1- Spectres RMN de divers noyaux avec et sans DNP à 4 K et 6,7 T. a) Spectres de noyaux ^{1}H à 285,3 MHz avec détection de la décroissance de l'induction libre (FID, *pour free induction decay*) après une impulsion à 90° de 3 µs. b) Spectres de noyaux ^{23}Na à 75,5 MHz avec détection après une impulsion à 90° de 3 µs. c) Spectres de noyaux ^{13}C à 71,7 MHz après une seule polarisation croisée adiabatique à partir des noyaux ^{1}H qui consiste en un balayage adiabatique de 800 µs, un intervalle central de 200 µs sans balayage de fréquence et un autre balayage adiabatique de 800 µs suivi d'une impulsion à 90° de 5 µs et la détection. d) Spectres de noyaux ^{17}O à 38,7 MHz avec détection d'un écho excité par une séquence d'écho 90° - τ - 180° - τ appliquée à la transition centrale du noyau S = 5/2. e) Spectres de noyaux ^{2}H avec détection après une impulsion de 90° de 4 µs à 43,8 MHz (notez l'éclatement quadrupolaire asymétrique du noyau S = 1). En rouge: signaux observés sans irradiation micro-ondes; en noir: signaux avec DNP positif; en bleu: signaux avec DNP négatif. L'échantillon contenait 50% d'éthanol-d_6, 40% de D_2O, 10% de $H_2{}^{17}O$ avec 1,5 M d'acétate de sodium (99% 1-^{13}C), 1 M d'urée (98% ^{15}N) et 40 mM de TEMPOL.

Les spectres des noyaux ^{1}H et ^{23}Na ont été acquis simplement par une impulsion à 90° suivie de la détection de la décroissance de l'induction libre (FID, *pour free induction decay*). Comme on peut le voir sur les Figures 1a et 1b, l'effet de l'irradiation par micro-ondes est beaucoup plus important pour ^{1}H en raison de la montée rapide de la polarisation. Une séquence de polarisation croisée adiabatique a été utilisée pour enregistrer les spectres des noyaux ^{13}C sur la Figure 1c car la polarisation directe avec TEMPOL est trop lente. Pour chaque spectre, il y avait une période d'attente de 20 s pour permettre la montée de la polarisation des noyaux ^{1}H, soit à l'aide de micro-ondes (spectres noir et bleu), soit pour permettre le retour à l'équilibre thermique (spectre rouge). Un seul contact adiabatique avec un balayage adiabatique de 800 µs, un intervalle central de 200 µs sans balayage de fréquence, suivi d'un autre balayage adiabatique de 800 µs a été utilisé pour transférer la polarisation de ^{1}H à ^{13}C. Ensuite, une impulsion à 90° a été suivie de la détection du signal ^{13}C. L'observation du spectre ^{17}O à 38,7 MHz était plus difficile car une simple séquence d'acquisition d'impulsions conduit à un spectre déformé qui souffre d'artefacts, ce qui pourrait être dû à une résonance acoustique. Par conséquent, une séquence d'écho composée de $90°_{x}$ - τ - $180°_{\varphi}$ - τ - détection avec φ cyclé par incréments de 90° (EXORCYCLE [3]) a été utilisée pour acquérir les spectres de la Figure 1d. Évidemment, une partie du signal (qui est élargie par des interactions quadripolaires de second ordre inhomogènes) est perdue en raison de la décohérence, conduisant ainsi à un faible rapport signal sur bruit. Enfin, les spectres ^{2}H représentés sur la Figure 1e ont été enregistrés avec une impulsion à 90° suivie de la détection de la décroissance de l'induction libre, sans recourir à une séquence d'écho quadripolaire. Le fait intéressant à propos de ces spectres ^{2}H est l'observation d'éclatements quadripolaires. Il y a deux « cornes » intenses du motif de poudre, écartées d'environ 130 kHz, et deux épaulements extérieurs écartées d'environ 260 kHz.

La polarisation nucléaire dynamique d'échantillons à basse température, généralement entre 1,2 et 4,2 K, permet d'atteindre des températures de spin aussi basses que 2 mK, de sorte que pour de nombreux isotopes nucléaires, l'approximation à haute température est violée pour l'interaction nucléaire Zeeman. Cela conduit à des asymétries caractéristiques dans les spectres de poudre. Nous montrons que les formes de lignes dues aux couplages quadripolaires des spins de deutérium présents dans pratiquement tous les solvants utilisés pour de telles expériences (« jus de DNP ») permettent la détermination rapide mais précise de la température de spin du deutérium ou, de manière équivalente, de la polarisation du deutérium.

Un échantillon de 300 µL contenant 60% d'éthanol-d_6, 30% D_2O, 10% H_2O et 40 mM TEMPOL a été placé dans la bobine solénoïdale de la sonde RMN à large bande à basse température de fabrication maison. La sonde a été insérée dans un polariseur 6,7 T. Pour acquérir les signaux ^{2}H, le canal X a été adapté à 43,8 MHz.

La Figure 2 montre des spectres expérimentaux ^{2}H obtenus avec des échos quadripolaires [4, 5] excités par une séquence 18° - τ - 18° - τ combinée à un cyclage de phase à la manière d'Exorcycle [3].

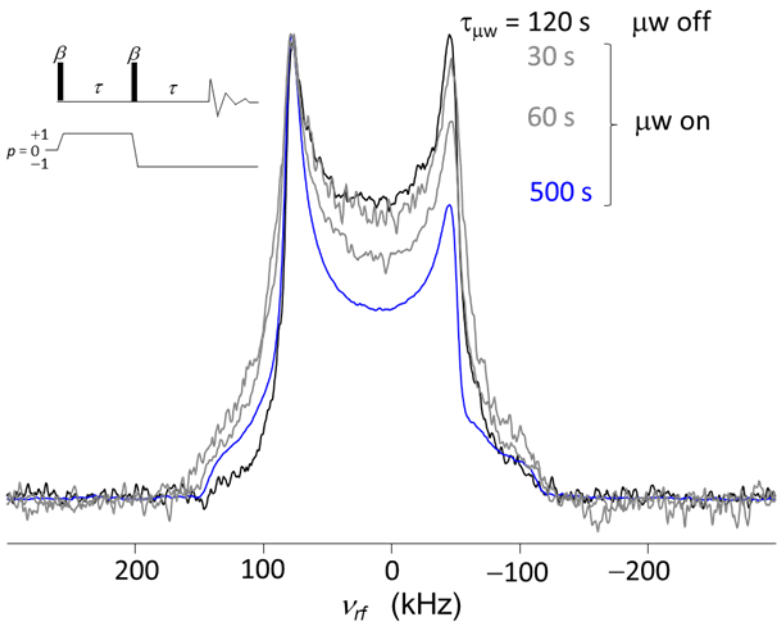

Figure 2- Spectres expérimentaux ^{2}H d'un échantillon constitué de 300 µL de 60% éthanol-d_6, 30% D_2O, 10% H_2O et 40 mM TEMPOL, obtenus avec une séquence d'écho quadripolaire « exorcyclée » $\beta - \tau - \beta - \tau$ avec β = 18° dans un champ B_0 = 6,7 T où $\upsilon_0(^1H)$ = 285,3 MHz et $\upsilon_0(^2H)$ = 43,8 MHz. Après avoir activé l'irradiation micro-ondes pendant une durée $\tau_{\mu w}$, une asymétrie de plus en plus prononcée du « spectre de Pake » quadripolaire est obtenue au fur et à mesure que la polarisation augmente. Pour des raisons de sensibilité, le spectre noir sans irradiation micro-onde a été acquis en faisant la moyenne de 16 échos à T_{sample} = 4,0 K avec β = 36 ° (τ_P = 2 µs). Tous les autres spectres ont été acquis à T_{sample} = 1,3 K en fonction de la durée de l'irradiation micro-onde $\tau_{\mu w}$ = 30, 60 et 500 s en faisant la moyenne de seulement 4 échos avec un cycle de phase et β = 18 ° (τ_p = 1 µs).

Le spectre noir de la Figure 2 a été acquis sans irradiation par micro-ondes à $T_{sample} = T_{spin}$ = 4,0 K et donne un motif quadripolaire symétrique. Lorsque la température de l'échantillon est abaissée à T_{sample} = 1,3 K et que l'irradiation par micro-ondes avec une fréquence appropriée pour induire une DNP positive est activée, une asymétrie progressive du doublet se manifeste, révélant l'abaissement de la température de spin ($T_{spin} << T_{sample}$) ou, de manière équivalente, la formation d'un état hyperpolarisé. Comme prévu, le rapport signal-sur-bruit s'améliore également à mesure que T_{spin} diminue. La polarisation la plus élevée obtenue dans cette série est représentée en bleu, tandis que les spectres obtenus à des températures de spin intermédiaires sont représentés en gris.

La Figure 3a présente le spectre ^{2}H hyperpolarisé expérimental montré précédemment (spectre bleu sur la Figure 2). L'asymétrie frappante des deux cornes du motif est mise en évidence par une flèche bleue. La Figure 3b montre une série de spectres simulés pour différentes valeurs de la polarisation $P(^2H)$, en supposant des échos quadripolaires de 18° - τ - 18°- τ avec des impulsions rf rectangulaires réalistes (υ_1 = 50 kHz) combinées à Exorcycle. Le spectre simulé qui reproduit le mieux l'asymétrie observée sur la Figure 3a est représenté en bleu, correspondant à une température de spin $T_{spin}(^2H)$ = 3,5 mK, ce qui équivaut à une polarisation $P(^2H)$ = 29%. Ces

simulations montrent que la température et la polarisation absolues du spin du deutérium peuvent être déterminées avec une précision de *ca.* ± 0,5 mK et ± 4%, respectivement.

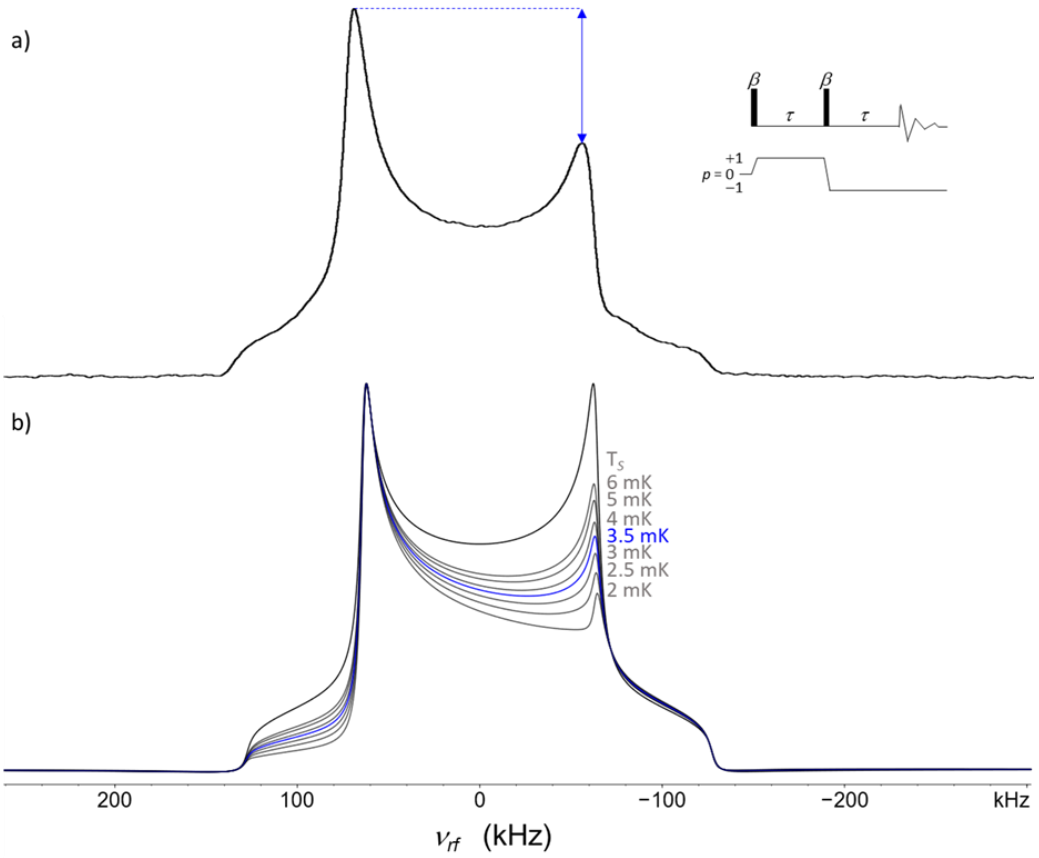

Figure 3- a) Spectre expérimental ^{2}H hyperpolarisé représenté en bleu sur la Figure 2. L'asymétrie entre les « cornes » du motif quadripolaire de Pake est mise en évidence par une flèche bleue. b) Simulations numériques en supposant différentes températures de spin T_{spin}. Le cas qui correspond le mieux à l'expérience en (a) est mis en évidence en bleu, correspondant à T_{spin}(^{2}H) = 3,5 ± 0,5 mK ou P(^{2}H) = 29 ± 4%.

La construction d'une sonde RMN basse température adaptée et efficace pour le nouveau système à projectile (bullet-DNP) n'était que la première étape. Il y a d'autres pièces dans un tel système qui doivent être conçues et optimisées une par une pour que la configuration complète fonctionne. Le processus commence par la préparation de l'échantillon et se poursuit par l'insertion de l'échantillon dans le polariseur tout en évitant les contaminations. Une fois la polarisation arrivée à son terme, l'échantillon est éjecté et transféré vers le spectromètre. Ce transfert est un aspect important et il doit être effectué le plus rapidement possible tandis que le chemin de transfert est protégé par un champ magnétique pour conserver autant de polarisation que possible (car la relaxation augmente considérablement à des champs très faibles). Enfin, l'échantillon solide doit être dissous rapidement et de manière homogène à l'arrivée avant la détection.

Étant donné que le polariseur est généralement à environ 4 K lors de l'insertion d'un échantillon, la fuite même d'une petite quantité d'air dans le système peut conduire à un blocage complet à l'intérieur de la sonde. Si cela se produit, la sonde doit être retirée du polariseur, réchauffée et séchée avant de la réinsérer. Par conséquent, une procédure stricte a été développée au fil des mois pour la préparation, l'insertion et l'éjection des échantillons afin de réduire le risque de contamination.

Puisqu'un échantillon congelé sans enveloppe s'est avéré peu pratique en raison de sa fusion rapide, un échantillon congelé contenu dans un cylindre en Téflon s'est avéré prometteur comme alternative pour notre système. Le Téflon ne contient pas de protons et ne contribue donc pas au signal des protons. De petits cylindres creux en Téflon aux extrémités ouvertes sont utilisés à cet effet. Selon leur longueur, ces cylindres peuvent contenir des échantillons de 20 à 40 µL.

Le transfert rapide et fiable des échantillons solides congelés du polariseur au spectromètre, tout en protégeant le chemin de transfert par un champ magnétique pour éviter les passages par zéro et les régions à faible champ, est une partie essentielle d'un appareil DNP par projectile. Cela est dû aux temps de relaxation très courts causés par les interactions dipolaires entre les radicaux et les noyaux cibles lorsque l'échantillon est à l'état solide. Un tube en polyéthylène avec un diamètre intérieur de 4 mm et un diamètre extérieur de 7 mm relie le polariseur au spectromètre. Ce tube est placé à l'intérieur d'un tunnel magnétique avec un champ homogène de 0,34 T.

L'utilisation de capteurs optiques révèle qu'il faut 100 à 250 ms à l'échantillon pour parcourir la distance d'environ 4,5 m entre le polariseur et le spectromètre. Après le transfert, l'échantillon doit idéalement être extrait rapidement et efficacement du cylindre en Téflon et dissous et mélangé dans un solvant correspondant.

Pour étudier l'efficacité du tunnel magnétique, deux expériences identiques ont été réalisées avec et sans le tunnel magnétique. Dans les deux expériences, le même cylindre en Téflon a été imprégné avec 25 µL d'échantillon contenant 60% de DMSO-d_6, 30% D_2O, 10% H_2O avec 1,5 M d'acétate de sodium (enrichi à 99% en ^{13}C en position carboxylique) et 5 mM de TEMPOL. Les échantillons ont été hyperpolarisés à 4 K au même niveau de polarisation en utilisant la polarisation croisée, et après le transfert de l'échantillon dans un tube RMN contenant 1,4 ml de D_2O, les spectres ^{13}C ont été enregistrés par des impulsions à 30 ° appliquées toutes les demi-secondes. Les spectres avec les plus grandes intégrales sont représentés sur la figure 4. Les spectres noir et rouge ont été obtenus après des transferts d'échantillons avec et sans tunnel magnétique, respectivement. Le tunnel magnétique a amélioré le signal d'environ un facteur 3.

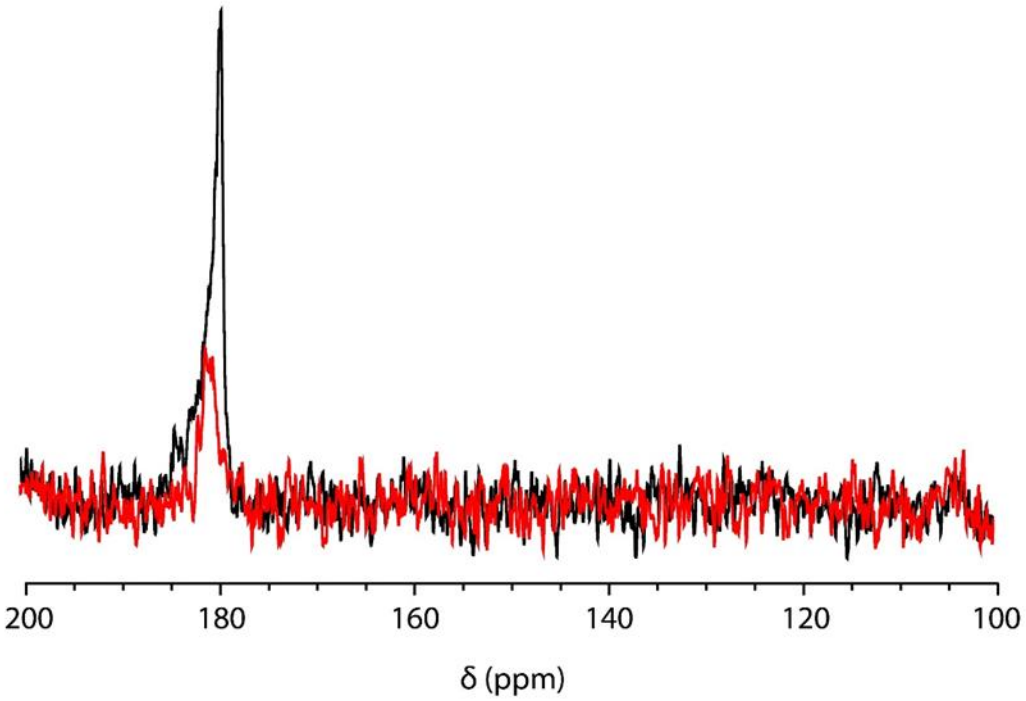

Figure 4- Spectres RMN du ^{13}C enregistrés à l'aide d'impulsions à 30 °. Le spectre noir est enregistré à l'aide du tunnel magnétique pendant le transfert tandis que le spectre rouge est obtenu après le transfert de l'échantillon sans tunnel. Les échantillons de 25 µl contenaient 60% de DMSO-d_6, 30% de D_2O, 10% de H_2O avec 1,5 M d'acétate de sodium (99% ^{13}C en position carboxylique) et 5 mM de TEMPOL. Ils ont été polarisés à 4 K et dissous dans 1,4 mL de D^2O à l'arrivée.

Partie B: mesure de la diffusion

Le coefficient d'autodiffusion translationnelle (*D*) est un paramètre de transport important des molécules dans les liquides [6]. Il peut révéler des informations chimiques telles que les masses moléculaires, les états d'agrégation ou l'association de différentes molécules [7]. Il existe deux méthodes principales pour mesurer les coefficients d'auto-diffusion. Les techniques de traceurs radioactifs sont des méthodes traditionnelles pour de telles mesures. Bien qu'ils puissent être très précis, ils souffrent de la difficulté des synthèses nécessaires, des temps de mesure longs, de l'ordre de quelques jours voire semaines pour un seul composant, et de perturbations inhérentes au système étudié en raison des substitutions isotopiques. D'autre part, les techniques de résonance magnétique nucléaire (RMN) sont capables de déterminer les coefficients d'autodiffusion dans des volumes d'échantillons modérés, sans marquage isotopique, généralement en quelques minutes [8].

Ici, nous proposons une manière directe de mesurer le coefficient de diffusion. L'aimentation d'un volume sélectionné est inversé par des gradients de champ pulsés appliqués dans trois directions. Ensuite, des images 1D de ce volume (suivant la direction du gradient de sélection) sont obtenues après un délai de diffusion variable. Les coefficients de diffusion sont calculés en comparant les images à différents temps de diffusion. Étant donné que la diffusion se produit principalement alors que la magnétisation est longitudinale, cette méthode est peu affectée par le temps de la relaxation transversale T_2. Cette technique offre un moyen saisissant de visualiser la diffusion car l'étalement des molécules peut être clairement observé d'une image à l'autre. Cela rappelle l'étalement d'une gouttelette de colorant dans une solution, peut-être la manière la plus simple d'illustrer les phénomènes diffusifs.

La figure 5 montre une série d'images 1D le long de la dimension *x* pour 4 valeurs différentes de t_D. Les effets de diffusion sont facilement saisis sur la figure. Au fur et à mesure que l'intervalle t_D augmente, le profil devient plus large et plus lisse, ce qui montre clairement la diffusion des molécules. L'intensité diminue non seulement en raison de la diffusion (qui maintient la surface constante) mais également par la relaxation longitudinale T_1.

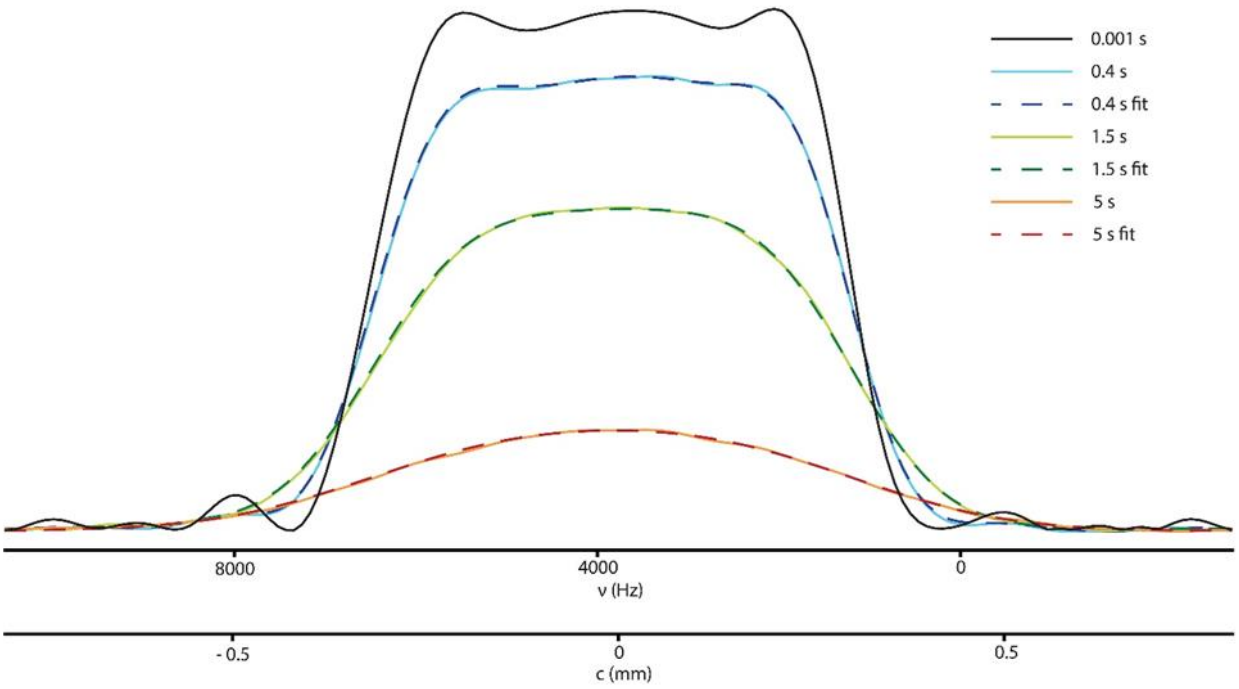

Figure 5- - Coupes obtenues par imagerie à une dimension d'un échantillon de H_2O le long de la direction *x* après des intervalles t_D = 0,001, 0,4, 1,5 et 5 s montrant l'étalement moléculaire dû à la diffusion à T = 25 °C. Les résultats des ajustements sont indiqués par des lignes pointillées.

Chapter 1

1. Introduction

1.1. Nuclear Magnetic Resonance (NMR)

Nuclear magnetic resonance (NMR) spectroscopy is a powerful method that can give insights into chemical processes and has the capability to characterize a wide variety of molecules. The simplicity of the preparation, absence of damage to the analyte, and moderate sample volumes needed are among the important reasons which make NMR a widely used spectroscopy method.

1.1.1. Historical perspective

In 1933 it was experimentally proven that certain atomic nuclei (like protons) possess spin and a magnetic moment [9, 10]. This had long been suspected since the original Stern-Gerlach experiment [11] in 1922 which proved the same characteristics for electrons [12].

The work of Rabi *et al.* [13] in 1938 lead to the first observation of NMR using a beam of LiCl molecules. This impressive achievement (which brought Rabi the Nobel Prize in 1944) was followed by NMR observations on proton and deuteron beams [14], but those studies were limited to nuclei in small molecules under very high vacuum in a molecular beam. It was not until 1946 that observation of NMR was first reported in condensed matter by two independent research groups who published their observations within weeks of one another. Namely, Bloch, Hansen, and Packard at Stanford [15-17] and Purcell, Torrey, and Pound at Harvard [18].

At the time, the continuous wave (CW) method was the standard for NMR observations in which the radio frequency (rf) circuit in the apparatus was tuned to a given frequency while magnetic field strength was varied through the resonance condition. Bloch [16] suggested as an alternative method that one can expect to obtain a nuclear induction signal in the absence of an applied rf field after having suddenly perturbed the spin ensemble by the application of a short rf pulse at the resonance condition. It was Hahn who showed this method experimentally [19, 20]. In addition, he introduced the spin echoes by using sequence of pulses [21].

Even though pulse methods were useful in some applications, they didn't gain much attraction due to complexity of the free induction decay (FID) signal obtained following the excitation pulse [12]. That changed after the introduction of Fourier transform NMR (FT-NMR) by Ernst and Anderson in 1966 [22]. Shorter acquisition times and higher inherent sensitivity of FT-NMR are the two main advantages that changed the field dramatically. Years later that led to another big milestone, the development of two-dimensional (2D) NMR [23, 24], which is crucial for assigning lines in complex spectra.

1.1.2. Basic theory

Magnetic resonance is a phenomenon found in magnetic systems that possess both magnetic moments and angular momentum. Most isotopes possess an intrinsic nuclear angular momentum. NMR involves manipulations of these so-called nuclear spins. The following is a short description of the basic theory of NMR [25-30].

The spin angular momentum ($\boldsymbol{I}$) is quantized and its magnitude can be defined as follows:

$$|\boldsymbol{I}| = \sqrt{I(I+1)}\hbar. \tag{1.1}$$

Here $\hbar = h/2\pi$, where h is Planck's constant and I is the spin quantum number which can only be integer or half integer ($I = 0, 1/2, 1, 3/2, 2, \ldots$).

The magnetic moment of a nucleus ($\boldsymbol{\mu}$) which is what brings about nuclear magnetism is proportional to its spin angular momentum ($\boldsymbol{I}$):

$$\boldsymbol{\mu} = \gamma \boldsymbol{I}. \tag{1.2}$$

The proportionality factor γ is called gyromagnetic ratio and it is an important characteristic of each nuclear isotope. Measurements on nuclei with larger (absolute values of) gyromagnetic ratios provide an advantage in sensitivity compared to ones with smaller γ. This means that, everything else being the same, nuclei with large γ are easier to observe. For example, proton with $\gamma(^1\text{H}) = 26.75 \times 10^7\ rad.T^{-1}.s^{-1}$is more sensitive than phosphorus with $\gamma(^{31}\text{P}) = 10.84 \times 10^7\ rad.T^{-1}.s^{-1}$. There are several nuclei with negative gyromagnetic ratios, one of which is nitrogen-15 with $\gamma(^{15}\text{N}) = -2.71 \times 10^7\ rad.T^{-1}.s^{-1}$. Table 1.1 provides a list of the nuclei of interest in this thesis with their corresponding characteristics.

Table 1.1- Characteristics of the nuclei of interest for this research.

Nucleus	Spin quantum number I	Natural abundance (%)	Gyromagnetic ratio γ ($10^7\ rad.T^{-1}.s^{-1}$)
^{1}H	1/2	99.9885	26.75
^{2}H	1	0.0115	4.11
^{13}C	1/2	1.07	6.73
^{15}N	1/2	0.368	-2.71
^{17}O	5/2	0.038	-3.63
^{23}Na	3/2	100	7.08

By combining the equations (1.1) and (1.2), the following equation is obtained:

$$\mu = \gamma\sqrt{I(I+1)}\hbar. \quad (1.3)$$

Nuclei with the spin quantum number $I = 0$ have no magnetic moment ($\mu = 0$) and therefore are not observable in NMR. One of the most important examples in this regard is carbon-12 which makes up for 98.9% of this element in natural abundance and has no magnetic moment. In contrast, carbon-13 with the natural abundance of 1.07% has a spin quantum number $I = 1/2$ and is one of the most important elements for the study of organic compounds by NMR spectroscopy. Nuclei with $I = 1/2$ are relatively easy to handle and detect. Nuclei with $I > 1/2$ possess a quadrupolar moment and are often more difficult to manipulate and observe.

When a nucleus with angular momentum $\boldsymbol{I}$ and magnetic moment $\boldsymbol{\mu}$ is placed in a static magnetic field $\boldsymbol{B}$ (with magnetic strength of B_0 and direction along z), the angular momentum's component I_z along the direction of the field will be an integer or half-integer multiple of $\hbar$:

$$I_z = m\hbar. \quad (1.4)$$

Here m is magnetic or directional quantum number which can take $2I$ + 1 different values between $-I$ and $+I$.

This behavior of the nuclei is called directional quantization. For example, nuclei with $I = 1/2$ (such as protons) only have two m-values of $+1/2$ and $-1/2$. On the other hand, nuclei with $I = 1$ (such as deuterons) have three m-values of -1, 0, and $+1$.

Combination of equations (1.2) and (1.4) determines the magnetic moment of a nucleus along the field direction z:

$$\mu_z = m\gamma\hbar. \quad (1.5)$$

The energy of a nucleus' magnetic dipole in the mentioned magnetic field is:

$$E = -\mu_z B_0, \quad (1.6)$$

and by using equation (1.5) we have:

$$E = -m\gamma\hbar B_0. \quad (1.7)$$

This shows that for a nucleus with $2I$ + 1 possible orientations, there are $2I$ + 1 energy states when placed in a magnetic field. These energy states are called the nuclear Zeeman levels. The energy splitting for nuclei with $I = 1/2$ and $I = 1$ is shown in Figure 1.1.

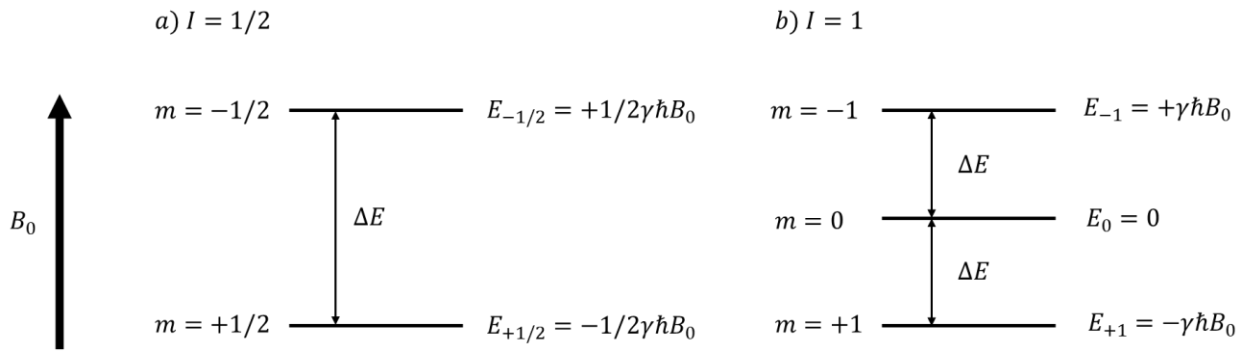

Figure 1.1- Energy level splitting for nuclei with a)$I = 1/2$ (such as ^{1}H or ^{13}C) and b)$I = 1$ (such as ^{2}H or ^{14}N) placed in a magnetic field with magnetic strength of B_0. There are $2I$ + 1 levels for each spin and the spacings between the energy levels are proportional to the gyromagnetic ratios and the strength of the magnetic field.

Quantum mechanics dictates that only transitions in which the magnetic quantum number m changes by 1 are allowed ($\Delta m = \pm 1$). This means that only transitions between adjacent energy levels can happen and the other transitions are forbidden.

The difference of energy between two adjacent energy levels is:

$$\Delta E = \gamma\hbar B_0. \tag{1.8}$$

As is the case in any spectroscopy method, an interaction is needed to cause transitions between the energy levels. These transitions are frequency related:

$$\Delta E = h\nu. \tag{1.9}$$

In NMR experiments transitions between different energy levels are induced by irradiating the nuclei with a B_1 rf field at certain frequency. One can obtain the resonance condition from equations (1.8) and (1.9):

$$\nu = \nu_L = \left|\frac{\gamma}{2\pi}\right| B_0. \tag{1.10}$$

Here ν_L is the so-called Larmor frequency.

1.1.3. Sensitivity of NMR

When a macroscopic sample containing nuclei with non-zero spin quantum number (I) is placed in a strong magnetic field, a splitting between energy levels occurs. Each energy level will have a population and the difference between these populations is what allows the observation of an NMR signal. For nuclei with $I = 1/2$, the population of the upper energy level is usually represented by N_β while the population of the lower energy level is represented by N_α. Figure 1.2 illustrates this phenomenon.

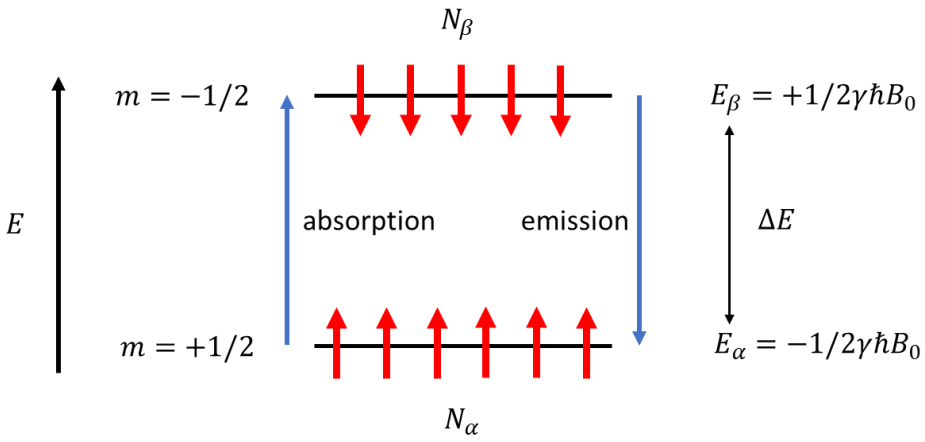

Figure 1.2- Energy level scheme for a system of nuclei with spin $I = 1/2$ placed in a magnetic field. Transitions between two energy levels are possible from lower to higher energy level and reverse which correspond to absorption and emission of energy respectively. These transitions are almost equally probable.

The energy difference is relatively small and transfer between them can happen at room temperature by thermal fluctuations. These transfers lead to so-called flip-flops of nuclear spins. In the case of equal populations ($N_\alpha = N_\beta$) at thermal equilibrium, no signal would be observed. This condition is known as saturation. However, as it can be seen in the Figure 1.2, there is an excess of the lower level's population ($N_\alpha > N_\beta$) and the observed signal's intensity is proportional to the population difference ($N_\alpha - N_\beta$). This distribution of population is described by a statistical Boltzmann distribution which, for the example of $I = 1/2$, is as follows:

$$\frac{N_\beta}{N_\alpha} = e^{-\Delta E/k_B T}. \tag{1.11}$$

Where k_B is the Boltzmann constant and T is the absolute temperature in Kelvin.

Under standard high-field NMR conditions at room temperature, the energy difference ΔE is very small in comparison to the average energy $k_B T$ of the thermal motions. That leads to nearly equal populations of the energy levels with just a little excess in the lower energy level (ground state).

The polarization can be defined as:

$$P = \frac{N_\alpha - N_\beta}{N_\alpha + N_\beta} = \frac{1 - N_\beta/N_\alpha}{1 + N_\beta/N_\alpha}, \tag{1.12}$$

which, in combination with equation (1.11), gives:

$$P = \frac{1 - e^{-\Delta E/k_B T}}{1 + e^{-\Delta E/k_B T}}. \tag{1.13}$$

Considering the mathematical definition:

$$\tanh(x) = \frac{e^x - e^{-x}}{e^x + e^{-x}} = \frac{1 - e^{-2x}}{1 + e^{-2x}}, \tag{1.14}$$

this leads to the general equation:

$$P = \tanh\left(\frac{\Delta E}{2k_B T}\right) = \tanh\left(\frac{\gamma \hbar B_0}{2k_B T}\right), \quad (1.15)$$

which can be simplified when $\Delta E \ll k_B T$ by using the approximation $e^{-x} \approx 1 - x$ to turn into:

$$P = \frac{\Delta E}{2k_B T} = \frac{\gamma \hbar B_0}{2k_B T}. \quad (1.16)$$

It can be observed that the polarization is proportional to γ and B_0 while it is inversely proportional to T.

The higher the gyromagnetic ratio, the higher the polarization. That is in fact one of the reasons why nuclei with larger gyromagnetic ratios provide increased sensitivity compared to nuclei with smaller values of γ. However, one has to pay attention that the gyromagnetic ratios are characteristic values of different nuclei and they cannot be altered to achieve more sensitivity.

Increasing the magnetic field (B_0) has always been one of the solutions to increase NMR sensitivity. That is why production of high field superconducting magnets was such a big step for the NMR community. There are constant efforts to move the boundaries and increase the field as much as possible but there are technological limitations that make this difficult. In addition, above certain fields, the price of the magnets increase drastically. The highest magnetic field currently commercially available is 28.2 T (1.2 GHz for ^{1}H) which leads to $P(^1\text{H}) = 0.0096\%$ at 300 K. An average accessible NMR magnet of 9.4 T (400 MHz for ^{1}H) results in $P(^1\text{H}) = 0.0032\%$ at 300 K.

The final parameter affecting the polarization is temperature (T). Going to low temperatures increases the polarization. For the same magnet of 9.4 T, polarizations of $P(^1\text{H}) = 0.0096\%$ and $P(^1\text{H}) = 0.2287\%$ can be achieved at the temperatures 100 K and 4.2 K respectively. However, decreasing the temperature is not ideal because it also decreases the molecular motions, hence increasing the rotational correlation time (τ_c). A very long τ_c decreases the transverse relaxation time (T_2), consequently leading to broader peaks and loss of resolution. In addition, it increases the long longitudinal relaxation time (T_1) and consequently the experimental time.

The above discussions show that NMR, although a very powerful technique, there is a lot of room to enhance its sensitivity. There are several methods to improve the sensitivity of NMR. One of the most powerful ways to improve the NMR sensitivity is dynamic nuclear polarization (DNP) which is the focus of this work and it is introduced in the following part.

1.2. Dynamic Nuclear Polarization (DNP)

Dynamic nuclear polarization (DNP) consists of transferring high electron spin polarization (the electron having a gyromagnetic ratio of approximately 660 times larger than protons) to target nuclear spins with the help of microwave irradiation which leads to a substantial nuclear polarization enhancement and hence an increase of the sensitivity of NMR spectroscopy.

1.2.1. Historical perspective

In 1953 Overhauser suggested the idea of transferring polarization from electrons to nuclei in metals [31]. This idea was experimentally confirmed by the work of Carver and Slichter [32]. They used lithium metal for their DNP experiments. Soon after Abragam suggested the same effect in nonmetals as well [33]. The next steps in this field were mostly about experimental and theoretical explorations into different DNP processes and mechanisms, starting from the work by Abragam and Proctor in 1958 [34] in which they introduced the DNP mechanism "Solid Effect" (SE). This kind of research was continued well into 1980's. During this period numerous notable works were done by scientists like Provotorov [35, 36], Borghini [37, 38], and Abragam and Goldman [39], to name just a few, that led to discovery and development of another DNP mechanism called "Thermal Mixing" (TM). Another mechanism called "Cross Effect" (CE) was also introduced during this period by Hwang and Hill in 1967 [40].

At this point, the DNP studies seemed to be a field that offered few perspectives for further improvement. There were not many promising and attractive hyperpolarization applications discovered by then, mainly because achieving very low temperatures on the order of a few Kelvins was required to acquire a hyperpolarized signal. However, the frozen static sample didn't offer well-resolved spectra which are needed in most applications. It took a few decades until modern DNP techniques emerged thanks to technical improvements such as high magnetic fields provided by superconducting magnets and, especially, powerful microwave sources which allowed achieving hyperpolarization while spinning a rotor at the magic-angle (to obtain high resolution) at high fields and near liquid nitrogen temperatures (90 < T< 110 K) [41].

Such a setup is called magic angle spinning-DNP (MAS-DNP) and offers an attractive and useful area of DNP that is currently the subject of much new research in view of boosting the sensitivity in solid-state NMR (SSNMR). Wind and co-workers first attempted to implement an MAS-DNP setup in 1985 [42] but lack of high-power microwave sources was an obstacle to extending DNP to higher fields [43]. It took years until MAS-DNP became popular mainly due to the efforts of Griffin and co-workers at MIT who performed many successful MAS-DNP experiments at high magnetic fields using gyrotrons to produce high-power microwaves [44-47].

Another big breakthrough in the field of DNP happened in 2003 where the work by Ardenkjær-Larsen *et al.* [1] demonstrated that hyperpolarization can survive a temperature jump caused by rapid dissolution of a frozen sample at liquid helium temperatures (1.2 < T< 4.2 K) followed by signal acquisition in solution state (typically > 300 K) which yields gains in sensitivity that can be as high as 10^4. This process, which is called dissolution-DNP (d-DNP), is currently the subject of numerous efforts in view of boosting the sensitivity of NMR and magnetic resonance imaging (MRI).

1.2.2. Dissolution-DNP (d-DNP)

Since its invention in 2003 [1], d-DNP has been known as one of the most promising methods to improve the sensitivity of NMR. Although a lot of technical considerations are involved, the

general concept is easy enough to grasp. In d-DNP experiments, samples containing the target molecules are doped with radicals or other paramagnetic polarizing agents (PAs). The enhancement is generated by a transfer of the high electron polarization of the PAs to the target nuclear spins via microwave irradiation at low temperatures ($1.2 < T < 4.2$ K) and high magnetic fields (typically $3.35 < B_0 < 10$ T) [48-50]. The sample is then dissolved and transferred to an NMR spectrometer in liquid state. At this point, any liquid-state NMR pulse sequence can be applied for detection, provided it can be completed before the hyperpolarized nuclei return to thermal equilibrium.

The current d-DNP setup in our lab at ENS Paris is shown in Figure 1.3. An extensive description of each part will follow.

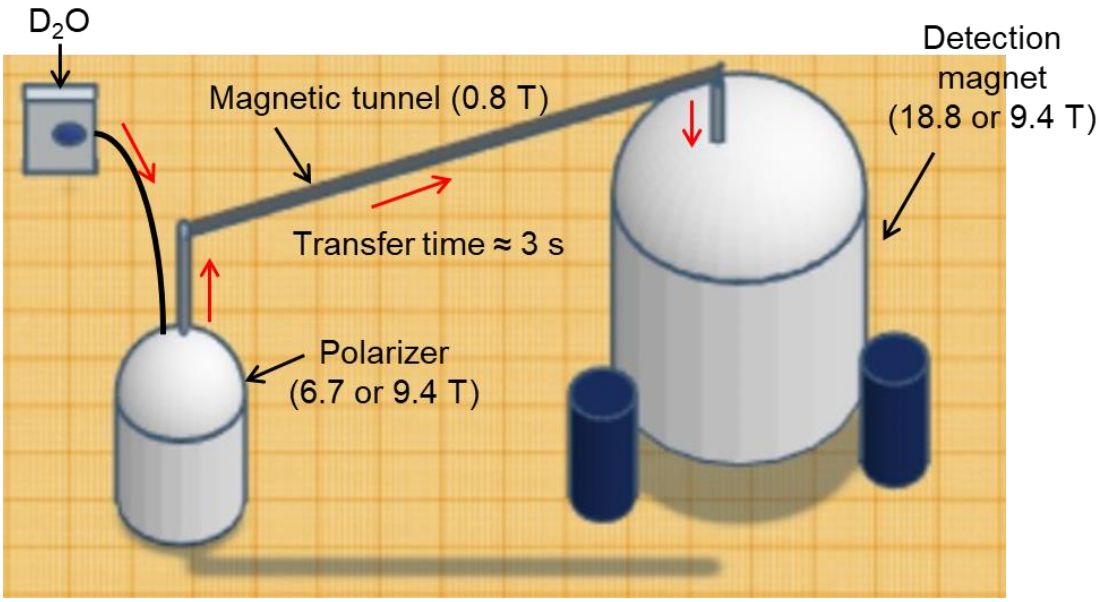

Figure 1.3- General view of the d-DNP setup in our lab. A hyperpolarized frozen sample of ca. 0.05 mL in the polarizer is dissolved with ca. 5 mL overheated D_2O under ca. 1 MPa. The liquid is transferred through a magnetic tunnel with a homogeneous field of 0.8 T. This transfer takes about 3 s and approximately 2.5 mL of solution arrives in the NMR tube inside the spectrometer for detection.

As shown in Figure 1.3, there are two operational polarizers of 6.7 and 9.4 T present in our lab. Each of them can be used in combination with either 18.8 or 9.4 T spectrometers (800 MHz and 400 MHz proton frequency, respectively). The 6.7 T polarizer is a Bruker prototype which needs a separate liquid helium Dewar to cool down. It consumes about 100 L of helium per week. The 9.4 T polarizer is a cryogen-consumption-free polarizer [50] that recycles helium in a closed loop to cool down and liquify the helium.

What follows is a complete d-DNP recipe from the sample preparation until detection in the spectrometer. This process is primarily described for the 6.7 T polarizer but can be easily adopted to the other polarizer at 9.4 T as well with some minor changes. Each part of the setup in Figure 1.3 will be examined in detail with illustrative photos.

1. Sample preparation and insertion: the exact optimum composition of a sample depends on the target nucleus and molecule that is being detected but a standard d-DNP sample (commonly called 'DNP juice') almost always contains 50-70% of a deuterated glassy agent (such as glycerol-d_8 or ethanol-d_6), 20-40% of D_2O, 10% of H_2O, and a suitable polarizing agent. The properties of the electron spin resonance (ESR) spectra of the PAs, such as their linewidths and electron spin-lattice relaxation times (T_{1e}), as well as nanophase separations in the sample, can have dramatic effects on the efficiency of the DNP process [51, 52]. For example, trityl radicals have narrow ESR lines which makes them suitable for direct polarization of ^{13}C, while widely available nitroxide radicals such as TEMPO (2,2,6,6-tetramethylpiperidine 1-oxyl) or TEMPOL (4-Hydroxy TEMPO) are good PAs for ^{1}H due to their broad ESR lines [1, 53-55].
   After preparation, approximately 0.05 mL of the sample is inserted into a PEEK sample container (Figure 1.4a) which is then connected to the sample stick (Figure 1.4b) and inserted into a probe inside the polarizer.

Figure 1.4- a) Low-temperature sample container made of PEEK. b) Sample container connected to the sample stick ready for insertion into the polarizer.

2. Hyperpolarization: as soon as the sample stick is inserted, the sample is cooled down and vitrified. The glassiness of the sample is very important to ensure that the PAs are homogenously distributed since this affects the final polarization. The sample temperature is usually between 4.2 and 1.2 K depending on the kind of experiment being performed. At 6.7 T, electrons have polarizations of 79.1 and 99.9% at 4.2 and 1.2 K, respectively. The large Boltzmann polarization of electrons is transferred to coupled nuclei via microwave irradiation at a frequency suitable for the saturation of electron spin resonance (ESR) transitions [55]. In this apparatus, the microwaves are provided by an ELVA1 source coupled to a Virginia Diodes (VDI) frequency doubler. Microwave frequency

modulation is usually implemented to saturate a large fraction of the EPR spectrum [56]. In addition to radiofrequency (rf) capabilities, a d-DNP probe transfers microwaves from the source through a wave guide to the sample. An overview of a typical d-DNP probe is shown in Figure 1.5.

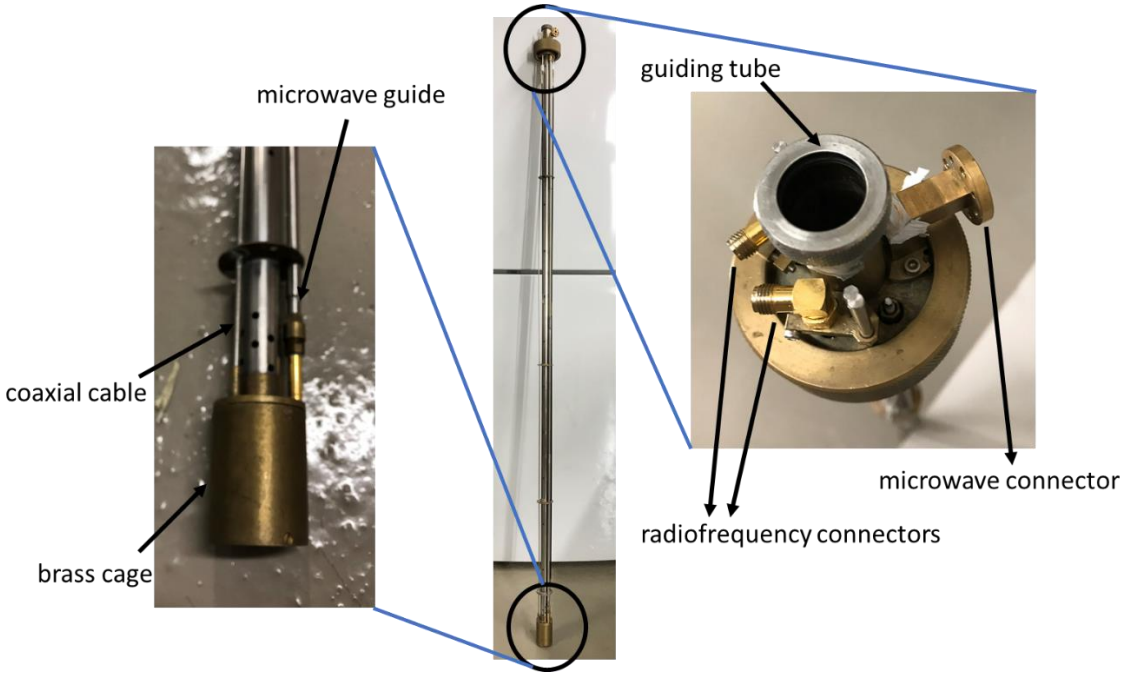

Figure 1.5- A view of a d-DNP probe (middle). The top part is magnified (right) which shows the guiding tube for insertion of the sample stick and rf and microwave connectors. A closer view of the bottom part is also shown (left) where the microwave guide, a coaxial cable, and a brass cage to protect the resonator are revealed.

This probe is placed inside the cryostat of the polarizer. Semi-rigid 50 Ω coaxial cables are used for the rf circuit. In addition to protecting the resonator, the brass cage confines the microwave field inside to have the maximum effect. Figure 1.6 demonstrates a closer look inside the rf components of the probe.

The coaxial cables are going from the top to the bottom of the probe and are connected to the induction coils at the bottom. These induction coils are coupled to the saddle coils mounted on a glass cylinder (Figure 1.6a). When inserting a sample via the sample stick, the sample is placed inside this glass cylinder and the microwave mirror is right in front of it. The sample is exposed both to microwaves and rf pulses at this position. Figure 1.6b shows the saddle coils mounted on the cylinder. Depending on the probe being a single resonance or a double resonance probe, there will be two or four saddle coils placed there. There are either just two coils in front of each other or another two are added perpendicular the previous ones. Because each pair is perpendicular to the other one, they are not coupled together. Each pair has its own induction coil and is tuned at a chosen nuclear frequency with the help of a few small fixed capacitors seen in Figure 1.6b. This type off circuit is tuned as close as possible to the desired nuclear frequencies but

small variations occur due to changes in the temperature and susceptibility of the different samples. Consequently, a tune and match box is designed for each nucleus to carry out the fine adjustment. This box (Figure 1.6c) is placed outside of the cryostat between the preamplifier and the rf connector on top of the probe.

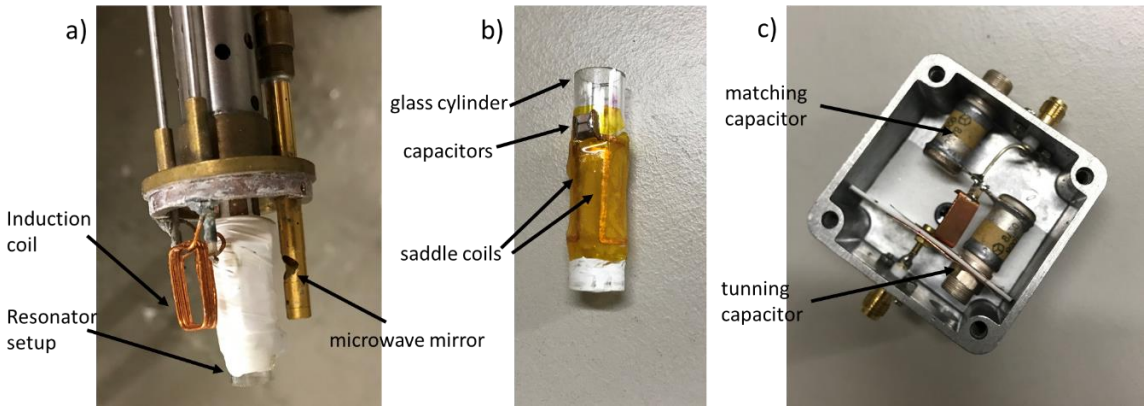

Figure 1.6- Different parts of the rf circuit of the d-DNP probe. a) Components inside the brass cage. b) Magnified look at the resonator's setup. c) Tune and match box for fine adjustments outside the polarizer.

The hyperpolarization level is monitored continuously by small angle pulses (usually between 1° and 5°). As soon as the polarization reaches its peak, the sample is ready for dissolution.

3. Dissolution: approximately 5 mL of D_2O is injected into the so-called pressure cooker shown in Figure 1.7. This device superheats the injected liquid to about 453 K (180 °C) under a pressure of ca. 1 MPa (10 bar). At this time, the dissolution stick attached to the pressure cooker is inserted into the sample stick in the cryostat while the sample stick is lifted about 9 cm so that the sample is not immersed in liquid helium. By pushing a button on the pressure cooker, a burst of hot liquid is projected on to the frozen sample inside the sample container. The flow is pushed with helium gas at about 7 bar. As it is shown in the magnified part of the dissolution stick in Figure 1.7, the liquid comes through the outlet, dissolves the sample and goes through the inlet for transferring to the spectrometer.

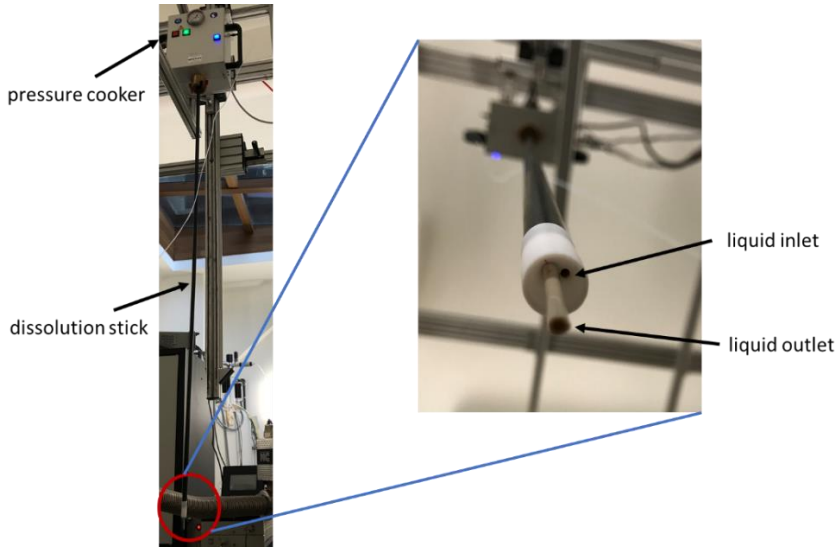

Figure 1.7- The dissolution device consisting of a pressure cooker and dissolution stick. The bottom part of the dissolution tick is magnified for illustration (right).

4. Transfer: the liquid is transferred to the spectrometer through a Teflon tube with 3.2 mm outside diameter and 1.6 mm inside diameter. Transfer time takes about 3 s over about 4 m. This tube is placed inside a permeant magnetic tunnel that extends from the polarizer to the spectrometer. This magnetic tunnel, which has a homogenous field of ca. 0.8 T, shields solutions carrying hyperpolarized nuclear magnetization from rapid relaxation that would occur during transfer through low fields [57]. Figure 1.8 shows one part of the magnetic tunnel. It is assembled according to a Halbach array.

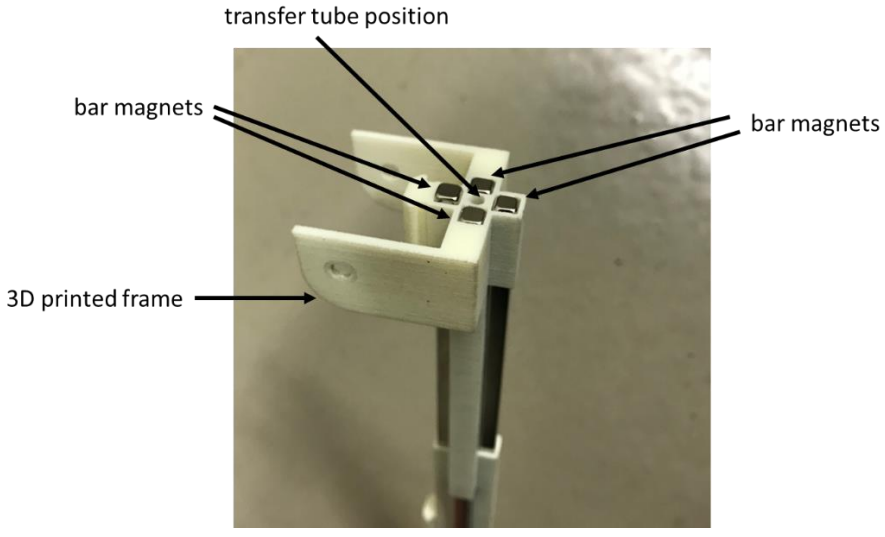

Figure 1.8- A segment of the permanent magnetic tunnel built according to the principles of Halbach arrays with a homogenous field of approximately 0.8 T inside.

5. Detection: approximately 2.5 mL of the solution arrives in the NMR tube after the dissolution. At this point one can start detecting a hyperpolarized signal. The

hyperpolarized signal can last from a few seconds to a few minutes depending on various parameters such as detection pulse angles, the molecule of interest, and the detected nucleus.

The process that was described can be different in some steps from one system to the other. The components may differ as well. However, the general outline of a d-DNP experiment is usually similar to what was discussed.

This method is well established and nowadays has been implemented in many labs. One of its main advantages is that the solution containing the hyperpolarized substance experiences relatively long relaxation times during transfer (ca. 10 s). This is achieved by the high dilution factor of ca. 100x. The dilution decreases the number of close contacts between radicals and nuclei. This increases the relaxation times since dipolar interactions between radicals and nuclei are the main source of relaxation during transfer. On the other hand, the mentioned high dilution factor and accompanying loss in sensitivity is undesirable in many cases such as for biological substances and can be counted as one of the main disadvantages of this setup. Another big disadvantage of this method is solvent limitation. For example, one cannot use organic solvents for dissolution because heating an organic solvent under pressure damages the pressure cooker and in addition the heat capacity of organic solvents are not sufficient to dissolve frozen samples in the polarizer.

Recently another method has been developed which overcomes these disadvantages and is called bullet-DNP. The general concept of bullet-DNP is described in the next section.

1.2.3. Bullet-DNP

In this method that has been introduced by Benno Meier *et al.* [2], the hyperpolarized solid is transferred to a spectrometer where it melts and is dissolved at room temperature before detection. The corresponding setup is shown in Figure 1.9 which gives a general overview. At first glance, this setup is similar to the setup in Figure 1.3, but in practice this setup needs a whole new design for each part of the system from sample insertion to final signal detection.

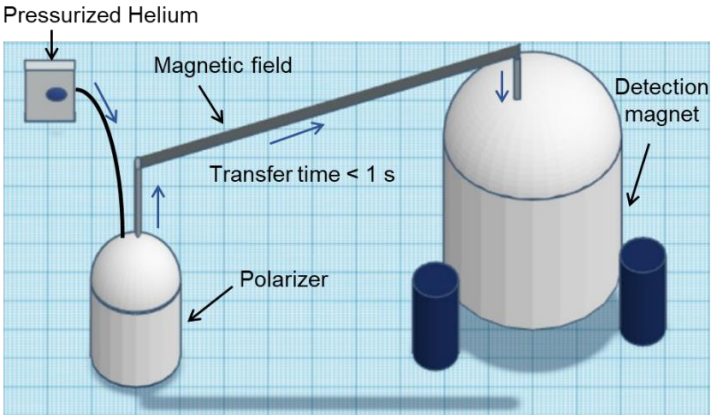

Figure 1.9- General outline of a bullet-DNP setup. The solid sample is transferred as fast as possible to the spectrometer through a magnetic field. It is then dissolved and the signal is detected.

A bullet containing the frozen, hyperpolarized sample is ejected using pressurized helium gas. A magnetic field of at least 0.1 T should protect the path from the polarizer to the spectrometer to limit radical-induced low-field relaxation. In Ref. [2] a solenoid, wound along the entire transfer path, has been used for this purpose, but one can use any construction such as a permanent magnetic tunnel similar to what was described before. Very fast transfer and absolutely avoiding low fields are crucial parts of this system, more so than in traditional d-DNP. This is due to the fact that radicals and hyperpolarized nuclei are in a very compact solid (10-50 µL) which makes relaxation caused by dipolar interactions all the more efficient. The relaxation time during transfer is ca. 1 s. The transfer is then followed up by fast and homogeneous dissolution before detection in the spectrometer. Designing and implementing such a system from ground up is the main part of this research. Details and procedures concerning all the parts of the newly designed bullet-DNP setup currently operational in our lab will be discussed in this work.

The main advantages of the bullet-DNP system are the control on the dilution factor which can be as low as 10x and the possibility of using diverse solvents for dissolution. These advantages open up new possibilities to use d-DNP on samples which are not compatible with traditional setups. For example, it allows one to perform d-DNP on a large class of polymers which are not soluble in water but can be dissolved in organic solvents.

1.3. An overview of the thesis

After this brief introduction it is now time to set the scene for what is about to be presented in the following chapters.

The description of our newly built bullet-DNP setup starts with chapter 2 where the design, production, and characteristics of a low-temperature NMR probe are described in detail. A probe specially designed for such a system was the first crucial step.

Chapter 3 follows up on an interesting observation of a quadrupolar Pake pattern while detecting ^{2}H signals on the newly designed probe at low temperatures in the polarizer. The asymmetry in powder spectra was used as a method to measure deuterium spin temperature in the DNP juice.

In chapter 4, all the other designed parts of the bullet-DNP system are described and the procedure to perform a complete experiment starting from sample preparation and insertion until ejection, transfer, and detection in the spectrometer is discussed in detail. In addition, a few preliminary results of performed dissolution experiments using the system are shown.

Chapter 5 is a separate chapter of its own. It is not related to DNP or to the bullet system. In this chapter the record of NMR as one of the most potent methods for measuring self-diffusion coefficients (D) in liquids is described and then an alternative method of measuring the coefficient of diffusion is put forward as a proof of concept.

Chapter 2

2. A low-temperature broadband NMR probe for multinuclear cross-polarization

2.1. Introduction

Any d-DNP setup requires a few components functioning together in order for the complete process to work. A polarizer with an efficient cryostat that can reach very low temperatures (between 1.2 and 4.2 K) as fast as possible and a reliable microwave source are essential to such setups. Furthermore, one needs a low-temperature NMR probe in the polarizer. The rf circuits of d-DNP probes are usually either single resonance to monitor the progress of polarization of a single nucleus or double resonance in which case one can perform cross-polarization (CP), in addition to observing either of the two nuclei. CP can be used as a powerful method to transfer polarization from nuclei that are rapidly polarized (like ^{1}H) to nuclei that have slower build-up rates (like ^{13}C). This method is explained in more detail later in this chapter.

Apart from the rf circuit, a d-DNP probe has to be suitable for insertion and ejection of a sample while remaining at a low temperature. In the previous chapter it was explained that our traditional d-DNP probes are designed to accommodate the insertion of a sample stick and a dissolution stick to insert and dissolve a sample. Unfortunately, they are not compatible for the insertion and ejection of solid samples (bullet-DNP [2]) and consequently another probe suitable for such a system had to be built.

D-DNP probes are usually designed for one or at most two specific nuclei. Investigation of multiple nuclei commonly requires manufacturing a number of costly probes. In addition, changing the probe is a time-consuming process since a system that works at low temperature must be warmed up, thus increasing the risks of contamination.

In this chapter, we describe a double resonance ^{1}H-X broadband probe adapted for a bullet-DNP system [58]. The X channel can cover a range of nuclei from ^{15}N to ^{23}Na (i.e., from 28.9 to 75.5

MHz at 6.7 T). This probe allows one not only to monitor the build-up of "direct" polarization on both channels, but also to perform CP between ^{1}H and any other nucleus within the range of the X channel. This probe is equipped with a horizontal solenoid coil to generate a homogeneous magnetic B_1 field. Unlike most conventional setups that have at least a few capacitors outside the polarizer for the fine adjustment of tuning and matching, in our case, the complete rf circuit is immersed in the low-temperature cryostat inside the polarizer. The capacitors and inductors can be adjusted by brass rods from the top of the cryostat. Usually, in other designs, one can only change the rf frequency over a range of about 6 MHz to compensate for small changes in tuning that may occur when changing samples with different susceptibilities. With the current design, we managed to tune the X channel over a very wide range of 50 MHz, thus providing a unique low-temperature broadband d-DNP probe. In addition, by moving various parts of the rf circuit from the top of the probe to the heart of the cryostat, energy losses are considerably reduced so that shorter pulse lengths can be achieved with less rf power. Intense radio-frequency fields with amplitudes on the order of 50 kHz or better can be applied simultaneously to both nuclei I (^{1}H) and S (nuclei within the range of X) using rf amplifiers with powers on the order of 90 and 80 W respectively.

2.2. Probe structure

In this section, the design and construction of the probe is described in detail. In addition, the main technical considerations that led to such a design are discussed alongside explanatory figures.

2.2.1. Radio-frequency (rf) circuit design

There are several rf designs that have been used in different d-DNP probes, ranging from internally doubly tuned and matched solenoids [59], externally doubly tuned and matched saddle coils [60], to locally quasi-distributed doubly tuned and matched Alderman-Grant coils [61].

In this probe we used a doubly tuned solenoidal coil with an axis that is roughly perpendicular to the main magnetic field. Solenoid coils generate far more homogeneous magnetic B_1 fields than Helmholtz coils. In addition, only one solenoid coil suffices to have a double resonance circuit. Figure 2.1 shows the schematic layout of the rf circuit used in the probe.

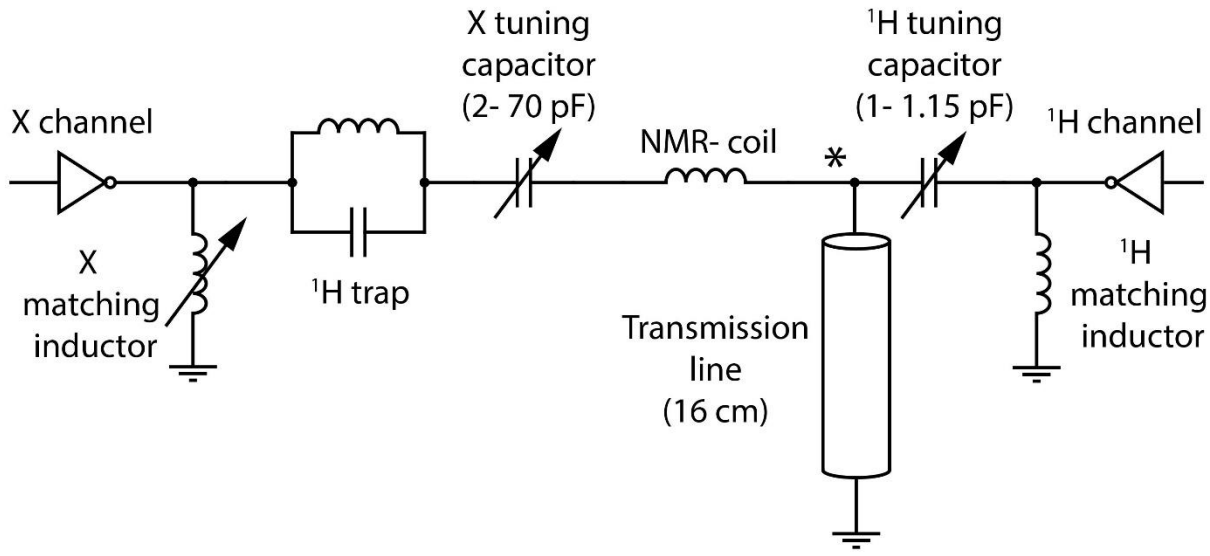

Figure 2.1- The schematic layout of the rf circuit. The transmission line is used in parallel to the main circuit. A combination of home-built and commercial capacitors and inductors is utilized to achieve a double resonance broadband circuit.

Two adjustable capacitors are used for tuning both channels. There is a wide range capacitor (2-70 pF) for the X channel since it must cover a wide range of nuclei and there is a narrow range capacitor (1-1.15 pF) that only accounts for the modifications in tuning of ^{1}H due to changes in susceptibility of different samples. An adjustable inductor is added to match the X channel. However, the inductor for matching ^{1}H is fixed so the proton channel is pre-matched because changes in matching for this channel are negligible. It was matched only once in the beginning and has been the same ever since. The $\lambda/4$ transmission line (λ being the wavelength) makes it possible to have double resonance in a single solenoidal NMR coil and also separates the X channel from the proton channel. This means that pulses applied to the X channel do not reach the proton channel. The LC circuit shown as the ^{1}H trap is performing the same task but from the other side. It does not allow pulses applied by the ^{1}H channel get to the X channel.

Initially, the design was different. It eventually evolved to what is seen in Figure 2.1 over time, due to technical issues that occurred while testing the probe numerous times at room temperature and at low temperatures in the cryostat. The main technical issues which led to the final design are as follows:

1. Initially, a 26 cm long hollow home-built $\lambda/4$ transmission line (λ = 105 cm being the wavelength *in vacuo* corresponding to the ^{1}H Larmor frequency of 285.3 MHz in the 6.7 T polarizer) was used in the system, but preliminary experiments showed that superfluid helium in the hollow space may lead to tuning instabilities. In the current version, a 16 cm long commercial semi-rigid 50 Ω coaxial cable with polyethylene dielectric was used to avoid these instabilities. The change in length corresponds the velocity factor of polyethylene. These two different transmission lines are seen side by side in Figure 2.2.

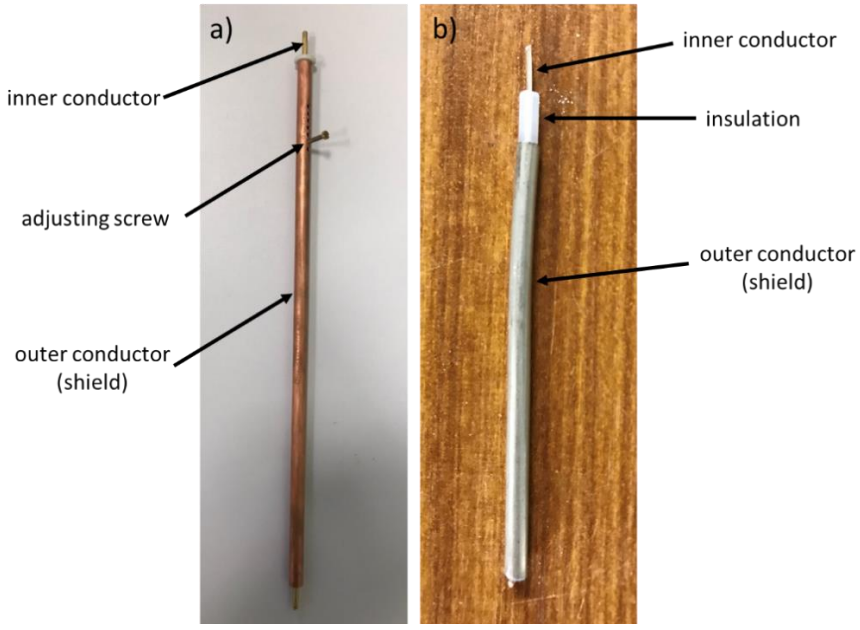

Figure 2.2- a) Home-built $\lambda/4$ transmission line with empty space between the inner and outer conductors. b) Transmission line made of semi-rigid 50 Ω coaxial cable with polyethylene between the inner and outer conductors.

The screw in Figure 2.2a was initially designed in order for the length of $\lambda/4$ transmission line to be adjusted if needed. However, in the end, the fixed length transmission line in Figure 2.2b proved to be more stable.

2. At first, using a $\lambda/4$ transmission line in series with the circuit allowed for good isolation between the two channels (in that case there was no need for a proton trap). But that design suffered from an inherent flaw: a significant fraction of the current from the ^{1}H transmitter was blocked before reaching the NMR coil, thus causing long pulse lengths. Using a transmission line in parallel to the main circuit as in Figure 2.1 solves this problem. It isolates the X channel because the point in the circuit marked by an asterisk (*) acts like a ground point for X frequencies below the proton frequency. However, it has no effect on ^{1}H isolation. That is why also a proton trap is needed.

3. A proton trap that consists of an LC circuit, which is tuned to about 40 MHz below the ^{1}H frequency, isolates the ^{1}H channel from the X channel. If the trap frequency gets too close to ^{1}H frequency that it should stop, the two of them will couple, rendering it impossible for the circuit to be tuned at the desired ^{1}H frequency. Even though the ideal place for the trap would be between the NMR coil and the X tuning capacitor (to prevent large losses in the large X capacitor), the coupling between the coil and the trap caused by their proximity led us to move the trap to the other side of the X tuning capacitor as it is seen in Figure 2.1. The home-bult LC trap is shown in Figure 2.3.

Figure 2.3- Actual view of the home-built ^{1}H trap tuned at approximately 40 MHz below the ^{1}H frequency.

The LC trap is built using a 4.7 pF fixed capacitor in combination with an inductor with 4 turns and diameter of about 7 mm. A normal copper wire of 1 mm diameter with plastic insulation is used to make this trap.

Now we can move from the design of the rf circuit to the construction of the probe itself and to the demonstration of the actual circuit in the probe.

2.2.2. Construction of the probe

The rigidity of the probe comes from 3 stainless steel tubes with inner diameters of 4 mm and outer diameters of 6 mm. Two of them are for injection and ejection of samples and the other one acts as a microwave guide. They are fixed together with the help of a few copper rings that are soldered to the tubes at various intervals. Figure 2.4a shows the structure in its simplest form in the beginning, while Figure 2.4b shows the final structure with assembled rf circuit, a brass cage on the bottom, and a vacuum-tight brass lid on top. Each part will be thoroughly discussed in this section.

Figure 2.4- a) View of the probe in the beginning of its construction. b) A general view of the probe in its final state.

Most of the electronic parts are assembled at the bottom of the probe. Some of the pieces are in the brass cage while the others are outside. Figure 2.5a gives a closer look of the parts outside the cage. Figure 2.5b on the other hand, focuses on the inside of the brass cage.

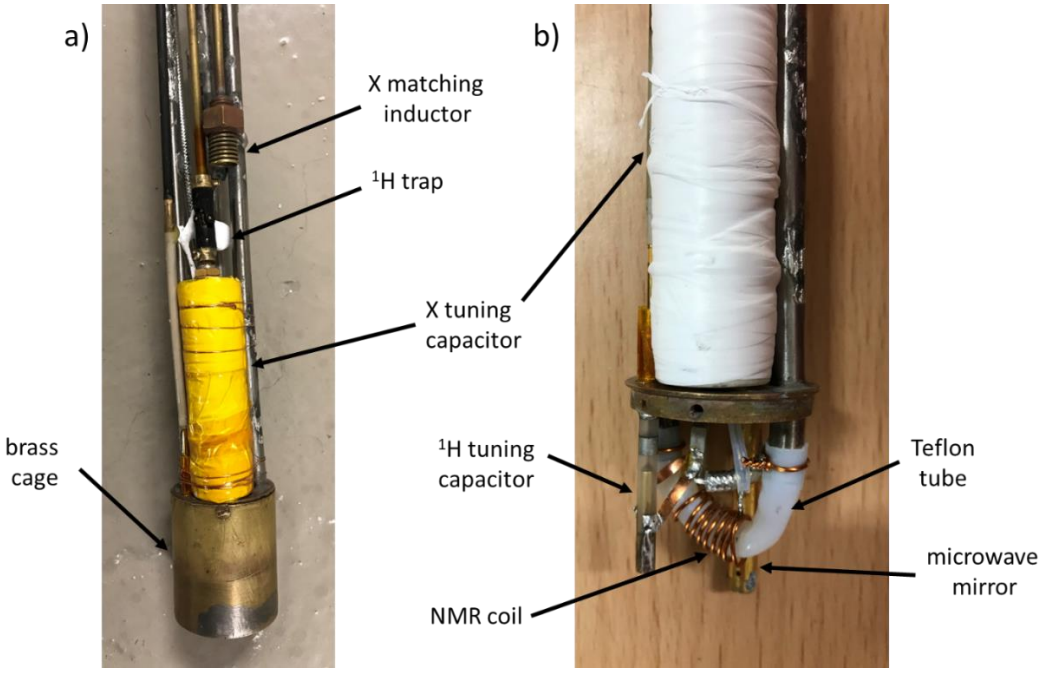

Figure 2.5- Two views of the lower part of the probe that can be immersed in superfluid helium. a) The electronic parts outside of the brass cage. b) Magnified view when the brass cage is removed. The tilted rf coil allows ejection of solid samples.

Note that the coil design is not adapted for dissolution DNP (which in current probes requires vertical access afforded by Helmholtz coils parallel to the magnetic field) but is ideally adapted for bullet-DNP. The tuning and matching circuits include home-built and commercial capacitors that are immersed in superfluid helium at temperatures down to 1.2 K. Care must be taken to avoid oscillations of the superfluid helium in the cryostat. The variable capacitors and inductors can be adjusted by turning brass rods that are isolated by dynamic seals. Sensitive electronic parts are wrapped in Teflon and Kapton tapes to isolate them from other metallic parts. The microwave guide, made of stainless steel, is terminated by a mirror to deflect the beam to the sample in the NMR coil. The parts below the X tuning capacitor, including the coil, microwave mirror, and ^{1}H tuning capacitor are encased in a cylindrical brass cage that confines the microwave field.

The top part of the probe is shown in Figure 2.6. It is important for this part to be vacuum tight because even small amount of air in the polarizer would lead to blockage, requiring the polarizer to be warmed up for the blockage to be removed. The moving rods are surrounded by dynamic seals to prevent this problem.

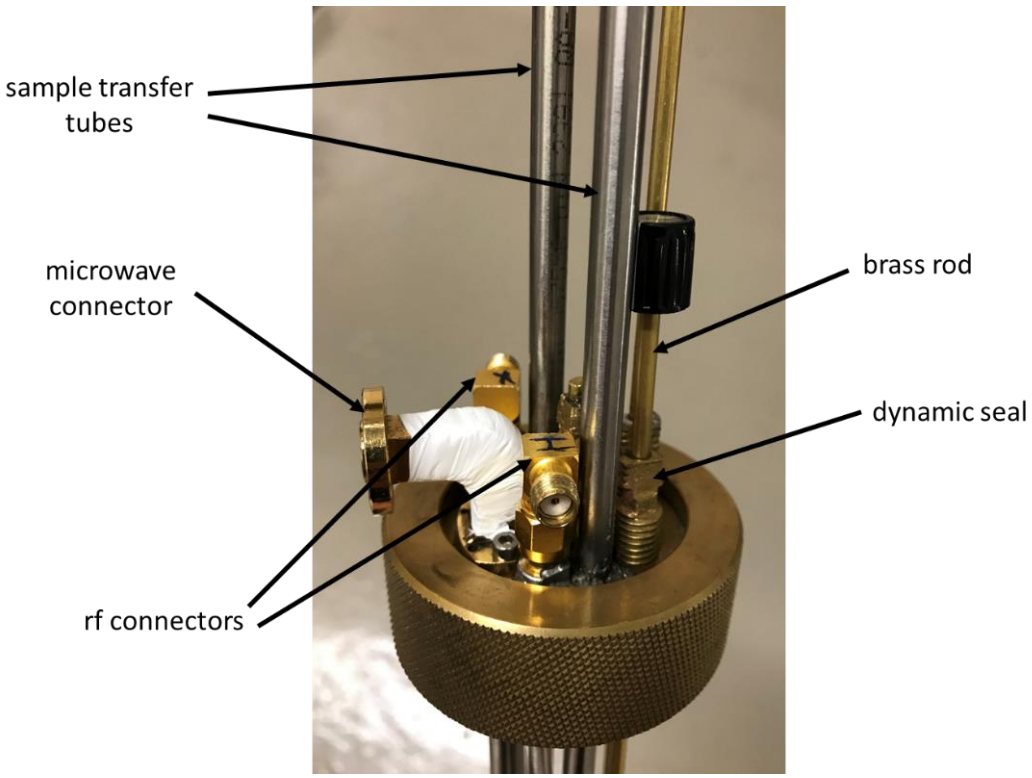

Figure 2.6- Top view of the probe.

Now that the hardware aspects of the probe have been discussed, it is time to demonstrate the actual results acquired by it.

2.3. Preliminary results and specifications

The initial tests were performed outside the polarizer at room temperature by connecting the probe to a Rigol DSA815 spectrum analyzer. Then the probe was inserted into a Dewar with liquid nitrogen for preliminary low temperature tests. Only after successful tuning and matching in liquid nitrogen, the probe was inserted into the polarizer for final tests at liquid helium temperatures. This cycle of tests was performed numerous times until all the technical issues with the rf circuit and moving parts were resolved.

The Q factor and the level of isolation between the two channels are important specifications of a probe that were monitored continuously while modifying the rf components. Table 2.1 reports these values for some important nuclei.

Table 2.1- Specifications of different nuclei at room temperature.

Nucleus	Frequency (MHz)	Q factor	Isolation (dB)
^{1}H	285.3	250	16
^{23}Na	75.5	137	17
^{13}C	71.7	133	17
^{2}H	43.8	81	27
^{17}O	38.7	99	27
^{15}N	28.9	87	27

The Q factor is a measure of the sensitivity of the probe: the higher the Q factor, the higher the sensitivity. Here the Q factor values are between 81 and 250, which is sufficient for d-DNP probes to measure signals of samples in thermal equilibrium in order to calibrate the level of hyperpolarization. Good isolation between the channels allows their independent tuning, and suffices to protect the amplifiers. Insufficient separation between the channels causes the resonance frequency of one channel to move while tuning the other channel. The isolation value of ^{1}H was measured with respect to ^{13}C.

Next, pulse calibrations and signal acquisitions of different important nuclei (with and without hyperpolarization) within the range of the probe, namely, ^{1}H, ^{23}Na, ^{13}C, ^{15}O, and ^{2}H, will be shown. Like in the conventional setup of the Bruker prototype of the polarizer, the microwaves are provided by an ELVA1 source coupled to a Virginia Diodes (VDI) frequency doubler. For positive polarization, the central microwave frequency was set to 187.9 GHz. Frequency modulation was done in a saw-tooth waveform with a modulation frequency of 1 kHz to cover a bandwidth of 200 MHz and saturate a large fraction of the EPR spectrum [56]. For negative polarization, the central frequency was set to 188.38 GHz while the other parameters were kept constant.

Two different samples were used for all measurements. Sample "I" containing 60% ethanol-d_6, 30% D_2O, 10% $H_2{}^{17}O$ and 40 mM TEMPOL and sample "II" containing 50% ethanol-d_6, 40% D_2O, 10% $H_2{}^{17}O$ with 1.5 M sodium acetate (with 99% ^{13}C in the carboxylic position), 1 M urea (with

98% ^{15}N) and 40 mM TEMPOL. For the sake of simplicity, these samples are mainly referred to by their numbers.

Note that ^{15}N is one of the important nuclei within the range of the probe but we couldn't detect a clean ^{15}N signal for technical reasons that we have not yet been able to identify.

2.3.1. ^{1}H spectra

Figure 2.7 shows a "nutation profile" of ^{1}H signals at 4 K, i.e., the signals detected after applying progressively longer rf pulses while keeping the transmitter power fixed at 90 W.

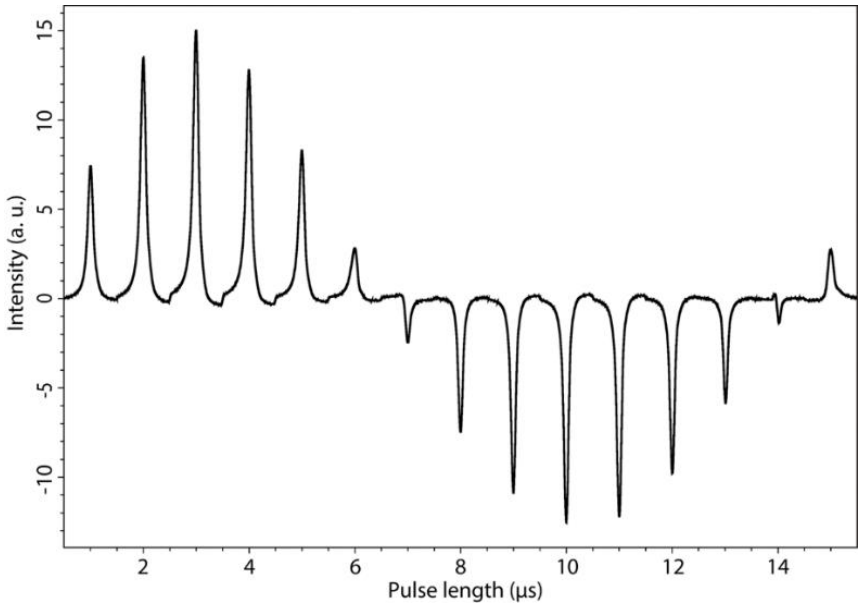

Figure 2.7- Nutation curve showing ^{1}H signals after excitation pulses of increasing duration with 90 W of pulse power at 4 K. The sample contained 60% ethanol-d_6, 30% D_2O, 10% $H_2{}^{17}O$ and 40 mM TEMPOL.

Sample "I" was used to acquire these data. The sinusoidal behavior is almost ideal and proves that the B_1 field is very homogeneous, which is not easily achieved in a d-DNP probe working at such low temperatures. The 90° pulse length is approximately 3 µs at 90 W, corresponding to a B_1 field of 83 kHz.

Figure 2.8 shows the detection of ^{1}H in test sample "II". The spectrum in red was obtained without microwaves, the spectrum in black with positive DNP, and the spectrum in blue with negative DNP.

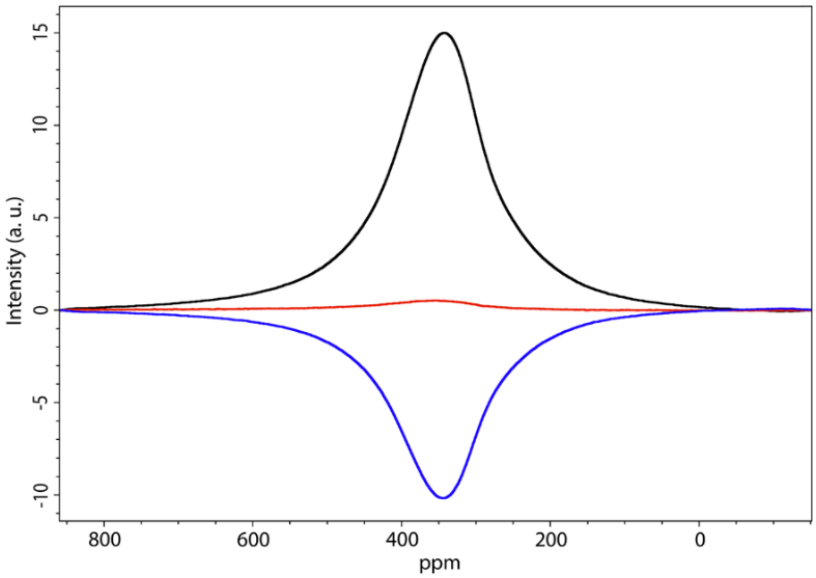

Figure 2.8- ^{1}H spectra at 285.3 MHz with and without DNP at 4 K and 6.7 T. Detection of free induction decays after a 90° pulse of 3 µs. Red: signal without microwave irradiation; black: signal with positive DNP; blue: signal with negative DNP. The sample contained 50% ethanol-d_6, 40% D_2O, 10% $H_2{}^{17}O$ with 1.5 M Sodium Acetate (99% 1-^{13}C), 1 M Urea (98% ^{15}N) and 40 mM TEMPOL.

Figure 2.9 demonstrates the difference in ^{1}H polarization levels at 4 K and 1.2 K using sample "II".

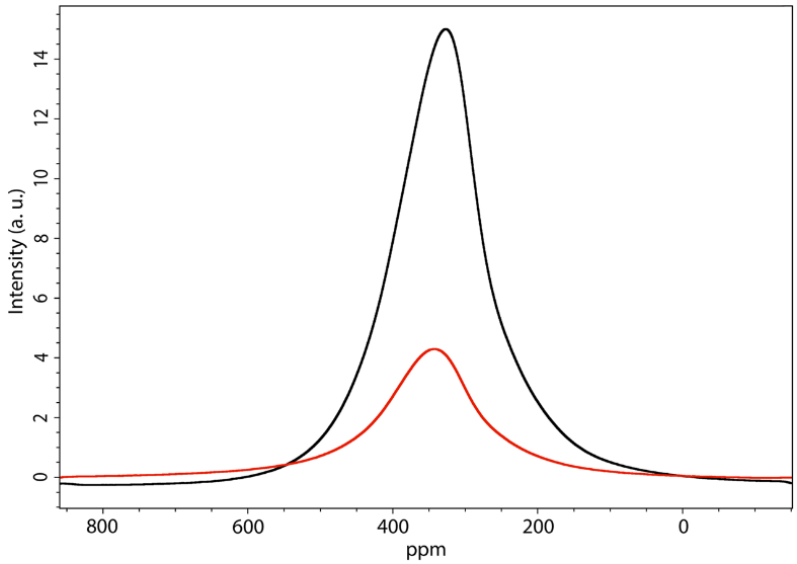

Figure 2.9- The effect of the temperature on ^{1}H DNP: red at 4 K and black at 1.2 K. Signals of ^{1}H excited by a 90° pulse of 3 µs with positive DNP. The sample contained 50% ethanol-d_6, 40% D_2O, 10% $H_2{}^{17}O$ with 1.5 M Sodium Acetate (99% 1-^{13}C), 1 M Urea (98% ^{15}N) and 40 mM TEMPOL.

The gain of the ^{1}H signal (acquired after a 90° pulse) is approximately a factor 4 when lowering the temperature from 4 to 1.2 K while keeping all other parameters constant.

2.3.2. ^{23}Na spectra

Figure 2.10 shows nutation profile of ^{23}Na signals in sample "II" with positive DNP by applying 80 W of pulse power at 4 K.

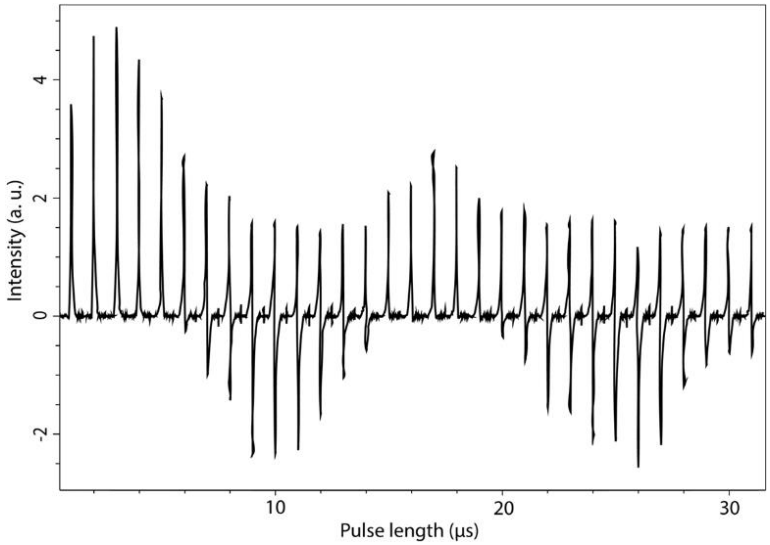

Figure 2.10- Nutation curve showing ^{23}Na signals at 75.5 MHz and 6.7 T with positive DNP after excitation pulses of increasing duration with 80 W of pulse power at 4 K. The sample contained 50% ethanol-d_6, 40% D_2O, 10% $H_2{}^{17}O$ with 1.5 M Sodium Acetate (99% 1-^{13}C), 1 M Urea (98% ^{15}N) and 40 mM TEMPOL.

It is seen that some phase changes occur during the nutation profile but nevertheless, the 90° pulse length of approximately 3 μs at 80 W can be determined from the profile. By using this 90° pulse calibration value, ^{23}Na spectra in Figure 2.11 are obtained without microwaves (red), with positive DNP (black), with negative DNP (blue).

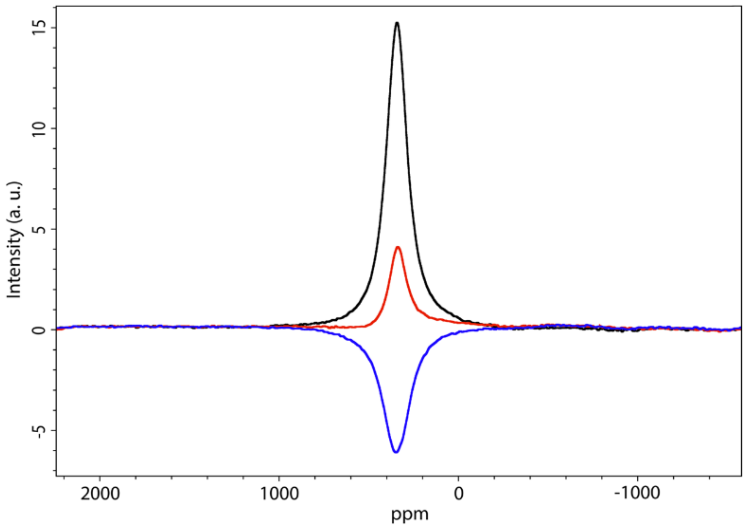

Figure 2.11- ^{23}Na spectra at 75.5 MHz with and without DNP at 4 K and 6.7 T. Signals detected after 90° pulses of 3 μs at 80 W. Red: signal without microwave irradiation; black: signal with positive DNP; blue: signal with negative DNP. The sample contained 50% ethanol-d_6, 40% D_2O, 10% $H_2{}^{17}O$ with 1.5 M Sodium Acetate (99% 1-^{13}C), 1 M Urea (98% ^{15}N) and 40 mM TEMPOL.

2.3.3. ^{13}C spectra

Since in many cases, "direct" polarization build-up rates are very slow at low temperatures (especially for nuclei with low gyromagnetic ratio γ), cross polarization (CP) can be used as a powerful method to transfer polarization from high-γ spins I (like ^{1}H) to low-γ nuclei S (like ^{13}C). Simply stated, both I and S nuclei are excited by 90° pulses, followed by spin lock pulses in the doubly-rotating frame. At this point if the Hartmann-Hahn condition:

$$\gamma_I B_1(I) = \gamma_S B_1(S) \tag{2.1}$$

is fulfilled, the contact between I and S is established and polarization transfer from I to S takes place. Preferably, this process is done in several consecutive cross-polarization contact intervals, which allows one to build up the polarization $P(S)$ of the low-γ nuclei S on a time scale typical for the build-up of the polarization $P(I)$ of the high-γ nuclei. At low temperatures 1.2 < T < 4.2 K, CP from I = ^{1}H to nuclei such as S = ^{13}C, ^{15}N, ^{6}Li, etc. has been demonstrated to be very effective [59, 60, 62-64].

The CP build-up pulse sequence that is used in this work is shown in Figure 2.12.

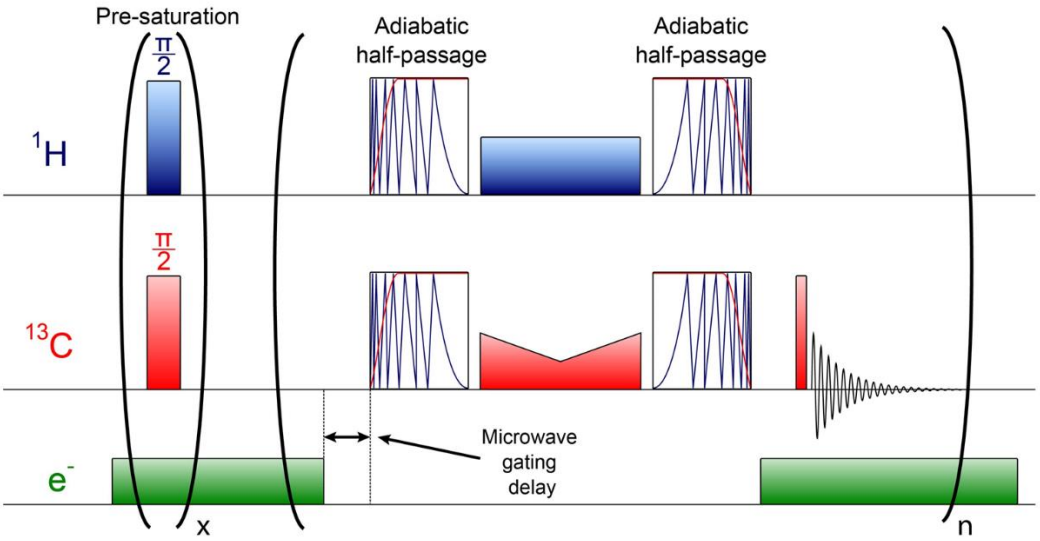

Figure 2.12- Multiple contact CP pulse sequence with microwave gating using an adiabatic half-passage sweep, central contact pulse, and another adiabatic half-passage sweep for both nuclei. The amplitude of the ^{13}C contact pulse is ramped down and up. (Figure courtesy of M. Baudin)

At the very beginning, consecutive 90° pulses with random phases are applied to both channels to destroy the previous polarization to monitor the build-up from the beginning. The microwave is switched off ("gated") prior to cross-polarization to allow the electron spins to return to their ground state, thus extending the lifetimes $T_{1\rho}(I)$ and $T_{1\rho}(S)$ of the spin-locked magnetizations of the I and S spins, and improving the efficiency of cross-polarization [65]. In each contact, nuclei are first excited with adiabatic half-passage sweeps, spin-locked with central contact pulses and

then flipped back with another set of adiabatic half-passage sweeps. The amplitude changes in the ^{13}C contact pulse allow one to decrease the sensitivity of CP to rf field inhomogeneities and offset effects [55, 66]. The build-up is monitored with small flip angle detection pulses (usually between 1° and 5°).

Pulse calibration of ^{13}C was done using sample "II" only for direct positive polarization. The corresponding nutation profile is seen in Figure 2.13. The profile is acquired with constant power of 80 W at 4 K. The 90° pulse length is approximately 5 µs at 80 W.

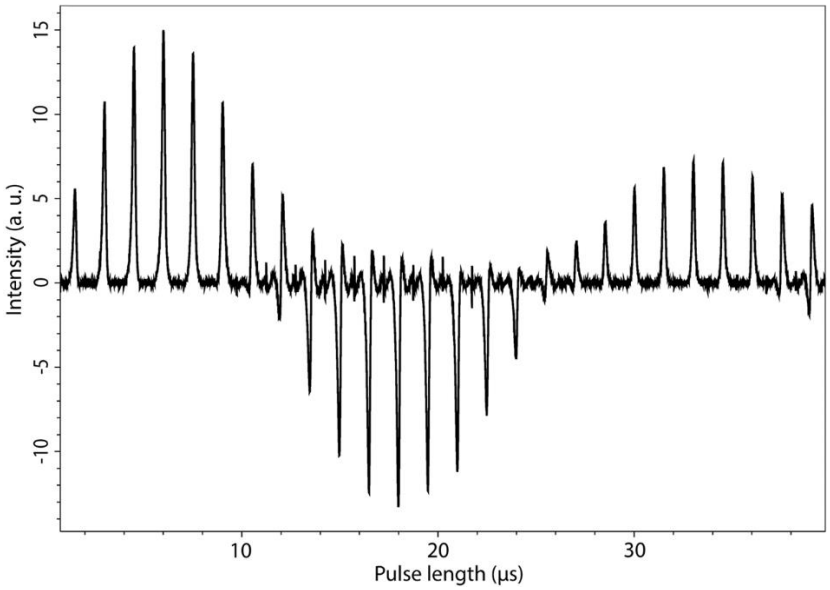

Figure 2.13- Nutation curve showing ^{13}C signals at 71.7 MHz and 6.7 T with positive DNP after excitation pulses of increasing duration with 80 W of pulse power at 4 K. The sample contained 50% ethanol-d_6, 40% D_2O, 10% $H_2{}^{17}O$ with 1.5 M Sodium Acetate (99% 1-^{13}C), 1 M Urea (98% ^{15}N) and 40 mM TEMPOL.

After pulse calibration, an adiabatic cross polarization sequence was used to record the ^{13}C spectra in Figure 2.14. For each spectrum, there was a 20 s waiting period to allow the build-up of the polarization of the ^{1}H nuclei, either with the help of microwaves (black and blue spectra) or to allow their return to thermal equilibrium (red spectrum). A single CP adiabatic contact with an adiabatic sweep of 800 µs, a central interval of 200 µs without frequency sweep, followed by another adiabatic sweep of 800 µs was used to transfer the polarization from ^{1}H to ^{13}C. Then a 90° pulse was followed by the detection of the ^{13}C signal.

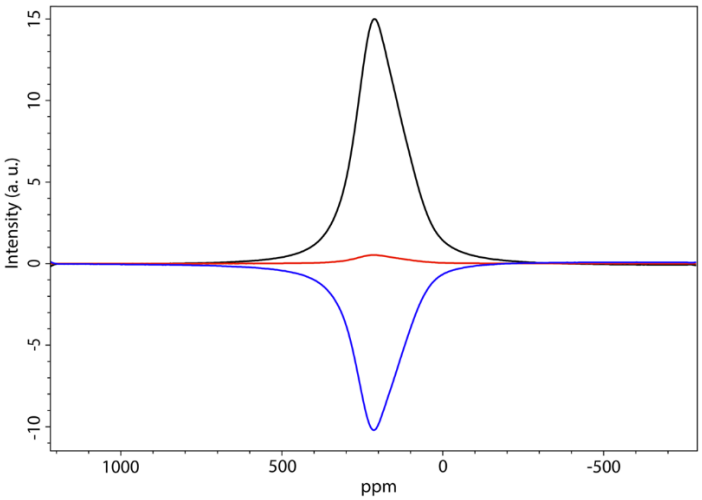

Figure 2.14- ^{13}C spectra at 71.7 MHz with and without DNP at 4 K and 6.7 T. Spectra acquired with a single adiabatic cross-polarization contact from ^{1}H to ^{13}C that consists of an adiabatic sweep of 800 µs, a central interval of 200 µs without frequency sweep, and another adiabatic sweep of 800 µs followed by a 90° pulse of 5 µs and detection. Red: signal without microwave irradiation; black: signal with positive DNP; blue: signal with negative DNP. The sample contained 50% ethanol-d_6, 40% D_2O, 10% $H_2{}^{17}O$ with 1.5 M Sodium Acetate (99% 1-^{13}C), 1 M Urea (98% ^{15}N) and 40 mM TEMPOL.

Figure 2.15 shows the build-up of the polarization $P(^{13}C)$ (integrals of the spectra), recorded by 5° pulses and detection at intervals of 20 s at 4 K and 1.2 K using sample "II".

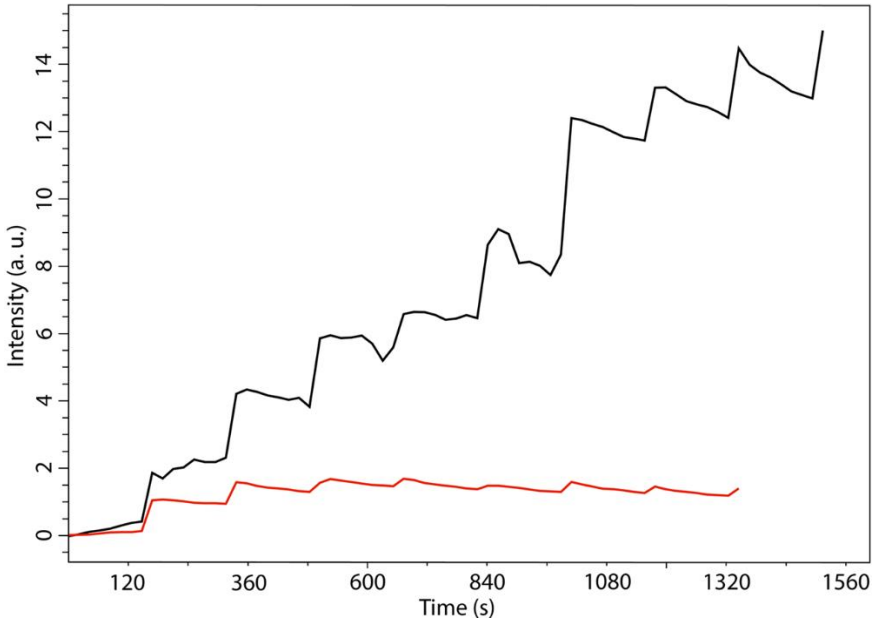

Figure 2.15- The effect of the temperature on DNP: red at 4 K and black at 1.2 K. Signals resulting after multiple-contact cross-polarization from ^{1}H to ^{13}C at intervals of 160 s to build up the polarization $P(^{13}C)$. Adiabatic cross-polarization with an adiabatic sweep of 800 µs, a central interval of 200 µs without frequency sweep, and another adiabatic sweep of 800 µs was applied to both nuclei at intervals of 160 s. The sample contained 50% ethanol-d_6, 40% D_2O, 10% $H_2{}^{17}O$ with 1.5 M Sodium Acetate (99% 1-^{13}C), 1 M Urea (98% ^{15}N) and 40 mM TEMPOL.

Every 8th interval (i.e., every 160 s), an adiabatic cross-polarization contact consisting of an adiabatic sweep of 800 µs, a central interval of 200 µs without frequency sweep, and another adiabatic sweep of 800 µs, considerably enhances $P(^{13}C)$. This effect leads to the steps that are seen in Figure 2.15. These steps are not perfectly regular at 1.2 K (black spectrum) and suffer from perturbations, presumably due to some electrical discharges (arcing). But the signals continuously increase at each step, showing that CP is efficient. The signal intensity is increased by a factor 8 when lowering the temperature from 4 to 1.2 K.

2.3.4. ^{17}O spectra

Observation of the ^{17}O spectrum at 38.7 MHz was more challenging since a simple pulse-acquire sequence leads to a distorted spectrum that suffers from artifacts, which could be due to acoustic ringing. Therefore, an echo sequence of θ° - τ - 180° - τ applied to the central transition of the S = 5/2 was used to detect the nutation profile of ^{17}O shown in Figure 2.16. This was performed on sample "I" by applying constant power of 80 W at 4 K while increasing the duration of pulses. The 90° pulse length is approximately 4.5 µs at 80 W.

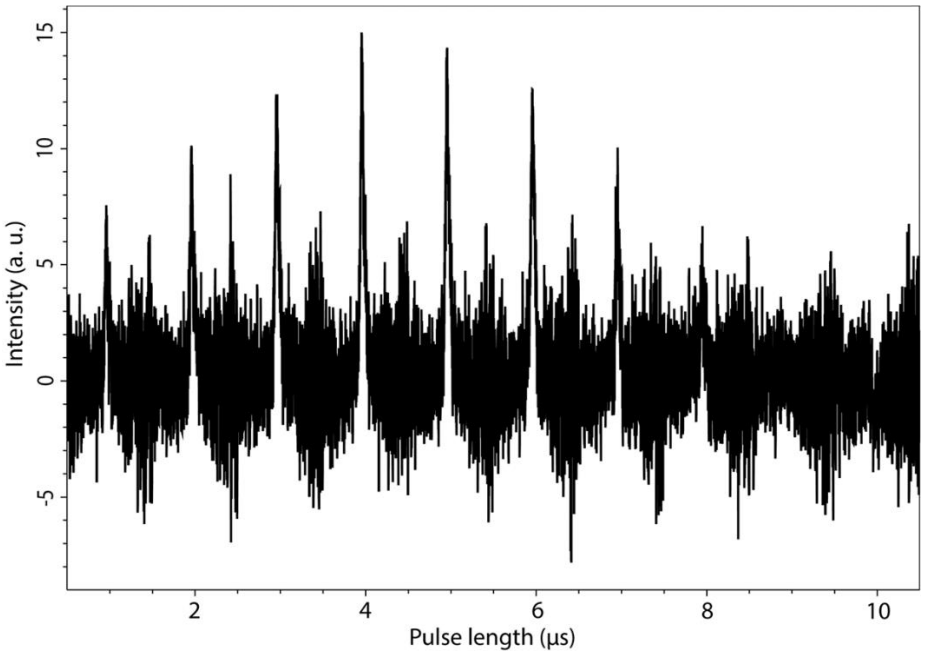

Figure 2.16- Nutation curve showing ^{17}O signals at 38.7 MHz and 6.7 T after excitation pulses of increasing duration with 80 W of pulse power at 4 K. A θ° - τ - 180° - τ echo sequence was used to detect the central transition of the S = 5/2 spin. Sample contained 60% ethanol-d_6, 30% D_2O, 10% $H_2{}^{17}O$ and 40 mM TEMPOL.

The vitrified sample "II" at 4 K led to the detection of spectra in Figure 2.17. Spectra in red, black, and blue are associated with no microwaves, positive DNP, and negative DNP respectively. To acquire the spectra in Figure 2.17, an echo sequence that consists of $90°_x$ - τ - $180°_\varphi$ - τ - detection with φ cycled in 90° increments (EXORCYCLE [3]) was used. Obviously, a part of the signal (which is broadened by inhomogeneous second-order quadrupole interactions) is lost due to decoherence, thus leading to a weak signal-to-noise ratio in comparison to the same type of spectra that was demonstrated previously for other nuclei.

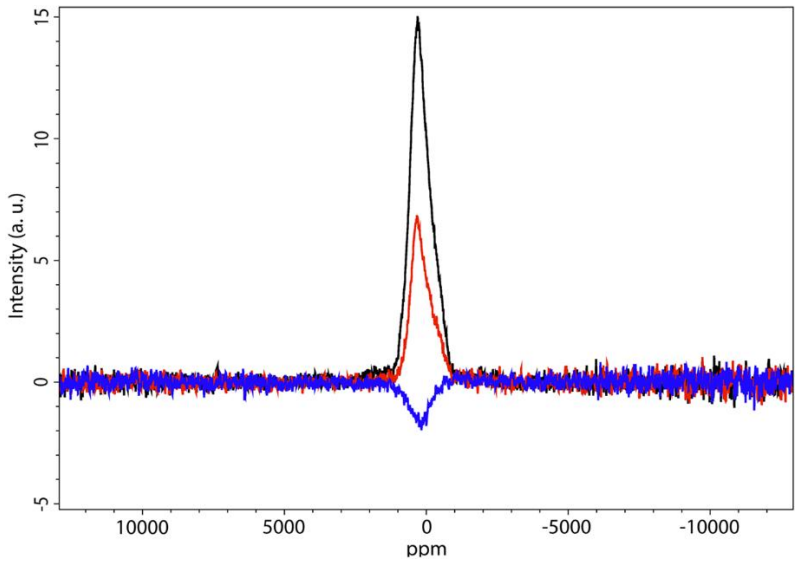

Figure 2.17- ^{17}O spectra at 38.7 MHz with and without DNP at 4 K and 6.7 T. Detection with an echo excited by a 90° - τ - 180° - τ echo sequence applied to the central transition of the S = 5/2 nucleus. Red: signal without microwave irradiation; black: signal with positive DNP; blue: signal with negative DNP. The sample contained 50% ethanol-d_6, 40% D_2O, 10% $H_2{}^{17}O$ with 1.5 M Sodium Acetate (99% 1-^{13}C), 1 M Urea (98% ^{15}N) and 40 mM TEMPOL.

The ^{17}O signal, which is due to the central transition of the spin S = 5/2 that is broadened by second-order quadrupole interactions to ca. 30 kHz, is best observed with an echo excited by a 90° - τ - 180° - τ sequence with τ = 43 µs. In addition to the fact that a part of signal intensity is lost due to decoherence, it is difficult to follow the polarization in real time since one cannot apply a series of pulses with small nutation angles (1° to 5°) to monitor the build-up. An echo pulse sequence was used to acquire the ^{17}O signal without and with microwave irradiation for a duration of two minutes to achieve positive polarization (red and black curves in Figure 2.18a). The modest gain of a factor ε_{Dir} = 2 can be ascribed to the slow direct build-up of the polarization $P(^{17}O)$. In Figure 2.18b, the red curve was again obtained without any microwaves but the black curve shows the advantage of using microwave in combination with cross polarization (CP) from ^{1}H to ^{17}O. After applying 64 pulses with 90° nutation angles and random phases at intervals of 10 ms to saturate both polarizations $P(^1H)$ and $P(^{17}O)$, microwave irradiation is applied for a time τ = 20 s. After this interval, the CP process takes place and the ^{17}O signal is detected as before by the same echo sequence. Comparison of two curves in Figure 2.18b shows an enhancement factor ε_{CP} = 6 in only 20 s, in contrast to the factor ε_{Dir} = 2 obtained in 2 minutes by direct polarization. This is clearly an indication of the efficiency of CP to boost the polarization of ^{17}O. To the best of our knowledge, this is the first time that cross polarization has been applied to ^{17}O in a d-DNP apparatus at 4 K.

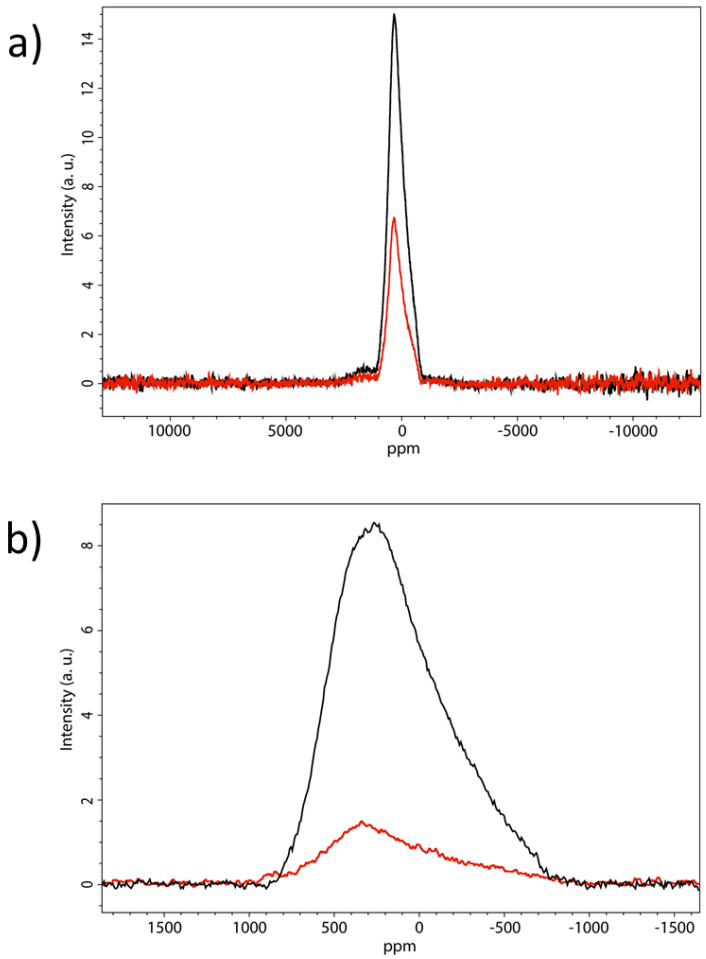

Figure 2.18- Comparison of direct polarization and cross-polarization of ^{17}O signals detected by a 90° - τ - 180° - τ echo sequence at 4 K. a) ^{17}O signals obtained (red) without microwave irradiation and (black) with positive DNP (enhancement of ε = 2). b) ^{17}O signals obtained (red) without microwave irradiation and (black) with a combination of microwave irradiation and cross-polarization from ^{1}H to ^{17}O, which consists of a single contact using an adiabatic sweep of 800 µs, a central interval of 200 µs without frequency sweep, and another adiabatic sweep of 800 µs applied to both nuclei (ε = 6). The sample contained 60% ethanol-d_6, 30% D_2O, 10% $H_2{}^{17}O$ and 40 mM TEMPOL.

As explained before, monitoring the polarization proved to be difficult. Therefore, an alternative method was chosen to provide a proof-of-concept to show the efficiency of CP from ^{1}H to ^{17}O. The interval τ between the presaturation pulses and the CP pulses was increased systematically from 5 to 300 s. In this time interval, the polarization of both $P(^{1}\text{H})$ and $P(^{17}\text{O})$ builds up with positive DNP. As mentioned before, the direct build-up of $P(^{17}\text{O})$ is very slow. The results of these experiments are shown in Figure 2.19. The largest (black) signal is observed for τ = 5 minutes.

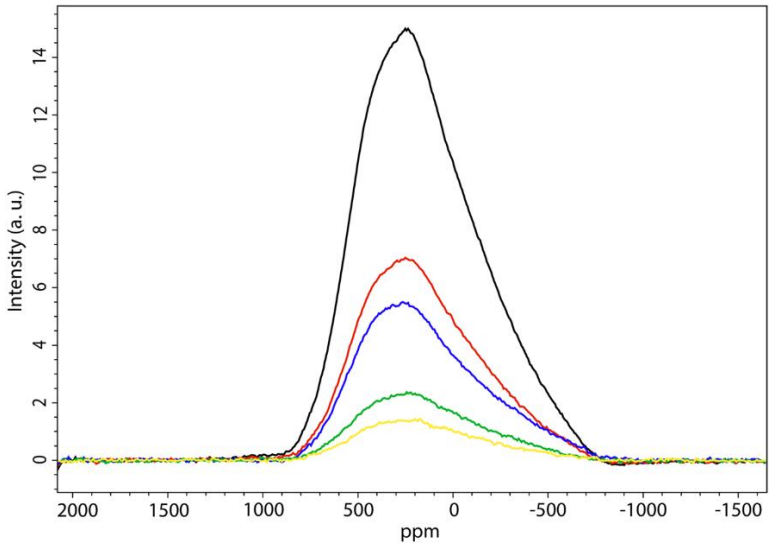

Figure 2.19- Cross-polarized signals of ^{17}O at 4 K and 6.7 T with different waiting times of 5 s (yellow), 10 s (green), 20 s (blue), 60 s (red), and 300 s (black) to allow the ^{1}H polarization to build up before a single contact by adiabatic cross-polarization from ^{1}H to ^{17}O consisting of an adiabatic sweep of 800 µs, a central interval of 200 µs without frequency sweep, and another adiabatic sweep of 800 µs applied to both nuclei. A 90° - τ - 180° - τ echo sequence was used to detect the central transition of the S = 5/2 spin which is broadened by second-order quadrupole interactions. The sample contained 60% ethanol-d_6, 30% D_2O, 10% $H_2{}^{17}O$ and 40 mM TEMPOL.

2.3.5. ^{2}H spectra

Figure 2.20 shows a nutation profile of ^{2}H signals in sample "I" by applying 80 W of rf power while progressively increasing pulse lengths at 4 K. Note that because of the quadrupolar splitting and phase changes, it is difficult to exactly pinpoint the 90° pulse length but it is approximately 4µs at 80 W.

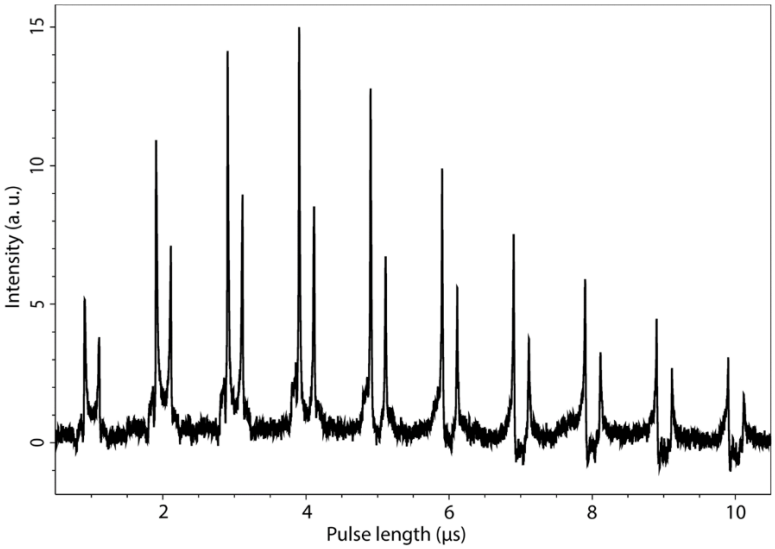

Figure 2.20- Nutation curve showing ^{2}H signals at 43.8 MHz and 6.7 T after excitation pulses of increasing duration with 80 W of pulse power at 4 K. The sample contained 60% ethanol-d_6, 30% D_2O, 10% $H_2{}^{17}O$ and 40 mM TEMPOL.

Figure 2.21 shows the detection of ^{2}H nuclei in sample "II" at 4 K. The spectrum in red was obtained without microwaves, the spectrum in black with positive DNP, and the spectrum in blue with negative DNP.

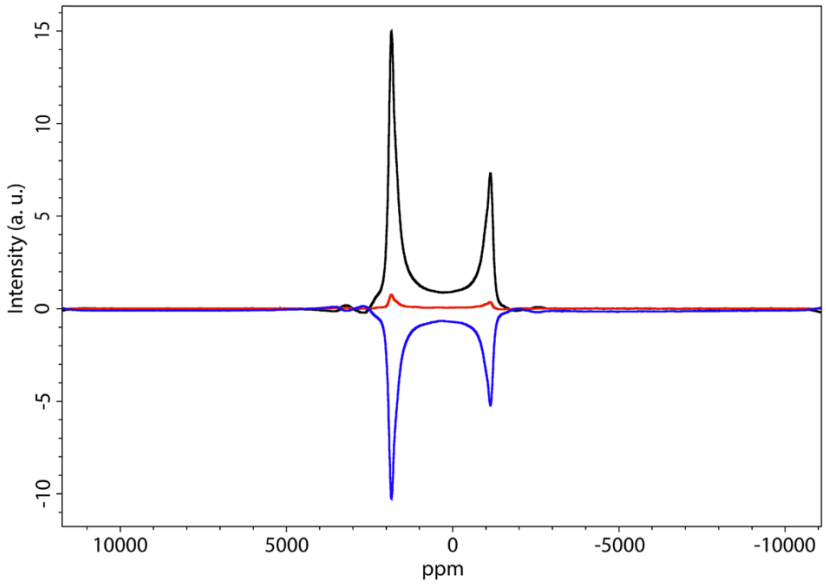

Figure 2.21- NMR spectra of ^{2}H with and without DNP at 4 K and 6.7 T. Detection after a 90° pulse of 4 µs at 43.8 MHz (note the asymmetric amplitudes of the quadrupolar doublet of the S = 1 nucleus). Red: signals without microwave irradiation; black: signals with positive DNP; blue: signals with negative DNP. The sample contained 50% ethanol-d_6, 40% D_2O, 10% $H_2{}^{17}O$ with 1.5 M Sodium Acetate (99% 1-^{13}C), 1 M Urea (98% ^{15}N) and 40 mM TEMPOL.

The ^{2}H spectra shown in Figure 2.21 were recorded with a 90° pulse followed by detection of the free induction decay, without resorting to a quadrupolar echo sequence. The interesting fact about these ^{2}H spectra is the asymmetry of the quadrupolar doublets. There are two intense 'horns' of the powder pattern that are approximately 130 kHz apart, and two outer 'shoulders' that have a distance of about 260 kHz. These values are comparable with the values reported at 154 K by Long, Ebelhäuser and Griffin [4] which are 200 and 400 kHz respectively in a powdered sample of $Ba(ClO_3)_2.2H_2O$.

The observation of this quadrupolar splitting inspired the idea of determining the spin temperature of ^{2}H in the sample, by evaluating the asymmetry of the horns. This will be the subject of chapter 3.

2.4. Chapter conclusions

An efficient broadband double-resonance probe has been developed that is ideal for the bullet-DNP system. This apparatus was used to detect NMR spectra of ^{1}H, ^{23}Na, ^{13}C, ^{2}H, and ^{17}O with direct polarization. In addition, ^{13}C and ^{17}O signals were also detected with cross polarization from ^{1}H. Unlike common designs of d-DNP probes, most of the rf circuit is immersed in superfluid liquid helium. Intense radio-frequency (rf) fields can be applied simultaneously to two nuclei using rf amplifiers with moderate power. A summary of the specifications for different nuclei is given in Table 2.2.

Table 2.2. Specifications and calibration parameters of different nuclei

Nucleus	Frequency (MHz)	Q factor	Isolation (dB)	90° pulse length (μs)	Amplifier power (W)
^{1}H	285.3	250	16	3	90
^{23}Na	75.5	137	17	3	80
^{13}C	71.7	133	17	5	80
^{2}H	43.8	81	27	4	80
^{17}O	38.7	99	27	4.5	80

Chapter 3

3. Spin thermometry

3.1. Introduction

To optimize d-DNP experiments, the nuclear spin polarization $P(S)$, or, equivalently, the spin temperature $T_{spin}(S)$, must be determined twice: once in the polarizer in the solid state, and once in the NMR detection magnet in the liquid state.

In the polarizer, this is usually done by comparing the signal intensities of protons or low-γ nuclei S obtained with and without DNP for 1.2 < T_{sample} < 4.2 K, where the spectra of amorphous frozen solids are very broad, typically 100 kHz for ^{1}H and ^{2}H, and 50 kHz for ^{13}C. Polarization values as high as $P(^{1}H)$ > 90% for protons with direct polarization and $P(^{13}C)$ > 70% for ^{13}C with cross-polarization (CP) in a polarizer with B_0 = 6.7 T have been reported [67].

After dissolution, one can likewise compare signal intensities of protons or low-γ nuclei S in solution, either boosted by DNP or obtained at thermal equilibrium after complete relaxation. The latter signals are many orders of magnitude weaker than the former, so that extensive signal averaging is often required. A more efficient alternative consists in measuring the asymmetries of doublets due to homo- or heteronuclear scalar couplings after dissolution [68-71].

Here, the focus will be on thermometry in the solid state at low spin temperatures. At first, several remarkable studies that have been carried out in this area will be mentioned and then, more specifically, ^{2}H spin thermometry in the context of d-DNP, which is the goal of this chapter, will be discussed.

Because of extensive dipole-dipole couplings, the proton spectra of amorphous frozen d-DNP samples below 4 K have broad shapes with line widths on the order of 100 kHz. These line shapes can become asymmetric at very low spin temperatures, and the sign of the asymmetry changes with the sign of the spin temperature, e.g., after inversion by a 180° pulse [72, 73]. However, it is difficult to determine the precise spin temperature from the analysis of the asymmetry of such broad lines [72, 74-76]. On the other hand, well-resolved dipolar Pake patterns can be observed

in ^{1}H NMR spectra of water molecules that are isolated in suitable matrices such as crystals of barium chlorate monohydrate [77-80].

In 1991, in the work by Andersen et al. [81], the intensities of two lines in the nuclear quadrupole resonance (NQR) of ^{127}I that are split by a weak Zeeman effect were compared. In 1995, Marohn and co-workers detected asymmetric quadrupolar satellites in optically detected ^{71}Ga NMR and could assess the polarization of its nuclear spin S = 3/2 from the asymmetry of the satellites [82]. In a study of the ^{15}N spectra in frozen doubly ^{15}N-labeled N_2O, the four partially overlapping Pake-like patterns were found to depend not only on the dipole-dipole couplings between the two ^{15}N nuclei, but also on the CSA tensors and their relative orientations. A careful analysis allowed the determination of an absolute polarization $P(^{15}\mathrm{N})$ = 10.2% after 37 h of microwave irradiation, without recording a time-consuming spectrum in thermal equilibrium [83]. Recently, an alternative method has been proposed to measure the polarization $P(^{1}\mathrm{H})$ by separately monitoring the Zeeman order S_z and the two-spin order $2I_zS_z$ (I = ^{1}H, S = ^{13}C) under magic-angle spinning conditions at 35 K < T_{sample} < 45 K [84].

In the previous chapter, the deuterium spectra acquired with the newly built probe revealed Pake-like powder patterns caused by the quadrupole interaction. This chapter presents an alternative approach to determine the deuterium polarization $P(^{2}\mathrm{H})$ (or equivalently, the deuterium spin temperature $T_{spin}(^{2}\mathrm{H})$) in the frozen solid prior to transfer and dissolution, by exploiting the asymmetry of quadrupolar doublets of deuterons in partly deuterated samples [85]. Following widespread practice, our frozen sample ("DNP juice") contains 60% ethanol-d_6, 30% D_2O, 10% H_2O and 40 mM TEMPOL. Ethanol-d_6, glycerol-d_8, or DMSO-d_6 prevent the formation of ice crystals that are deleterious for DNP. Note that all deuterated constituents of such frozen mixtures have roughly the same quadrupolar splitting. Methyl groups do not rotate freely below 4.2 K (although methyl groups can undergo fast rotational tunneling in some cases such as γ-picoline [86]), so that the quadrupolar couplings of most deuterated methyl groups are not scaled by motional averaging. There is therefore no need to add any specific molecules that contain deuterium. As we shall demonstrate, the observed powder patterns are asymmetrical because of the violation of the high-temperature approximation, provided that the coherences are excited with small flip angle pulses.

3.2. The effect of pulse flip angles on ^{2}H powder patterns

The use of rf pulses with small flip angles is dictated by the necessity to preserve the hyperpolarization as it builds up under microwave irradiation [72, 76, 87]. Small flip angle pulses have revealed asymmetries in proton spectra at very low spin temperatures [73, 76]. It is well known that the use of 90° pulses completely destroys the hyperpolarization. We performed numerical simulations of these effects on a first-order quadrupolar pattern associated with ^{2}H (spin I = 1), which is a common constituent of 'DNP juice'. The simulated spectra shown in Figure 3.1a were obtained by Fourier transformation of free induction decays excited by ideal excitation pulses with the rf carrier placed in the center of the quadrupolar doublets, assuming that the receiver could be activated immediately after an rf pulse. The nutation angle β was incremented

from 9 to 171° in steps of 9° (from bottom to top). The initial state corresponds to a fully polarized I = 1 spin, where only the $|1,+1\rangle$ state is populated (T_{spin}(^{2}H) = 0 K). For β < 20°, one obtains almost exclusively $|1,+1\rangle \leftrightarrow |1,0\rangle$ coherences, so that the powder pattern comprises mainly one of the two "lobes" or "cusps" of the Pake pattern. When the nutation angle approaches 180°, one obtains mainly the complementary lobe that is due to $|1,-1\rangle \leftrightarrow |1,0\rangle$ coherences. As expected, a symmetrical Pake pattern is obtained when β = 90°, due to the uniform excitation of both single-quantum coherences, regardless of the initial population distribution. At the same time, a 90° pulse leads to the equalization of the populations of all three spin states and therefore destroys the hyperpolarization. Figure 3.1b shows the density matrices and energy level diagrams corresponding to the single-transition spectra shown in blue in Figure 3.1a. The quadrupolar parameters for ^{2}H were assumed to be C_Q = 170 kHz and η_Q = 0 for the quadrupolar coupling constant and the asymmetry parameter, respectively [4]. The ^{2}H chemical shift anisotropy was ignored for simplicity.

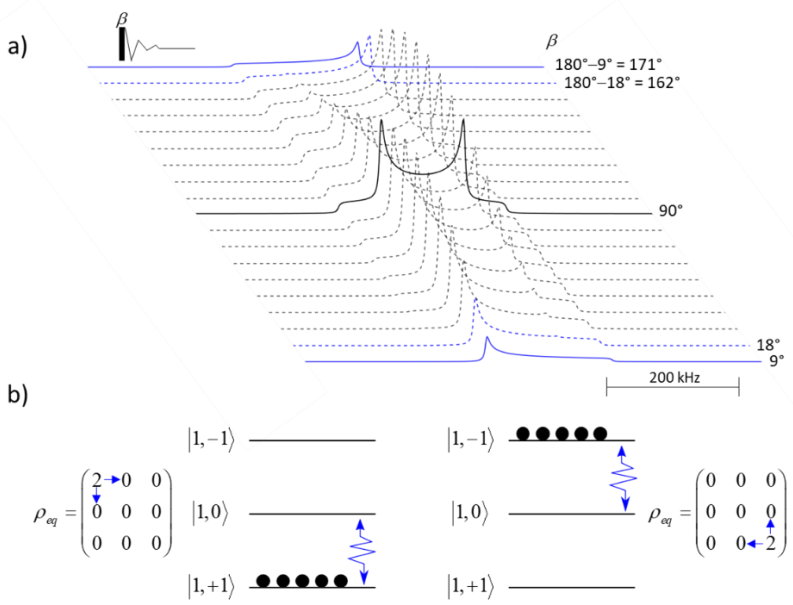

Figure 3.1- a) Numerical simulations of first-order quadrupolar lineshapes of ^{2}H spins in a powder with isotropically distributed crystallites, obtained by Fourier transformation of simulated free induction decays (without any delay between excitation and observation) excited by a single ideal pulse applied in the center of the quadrupolar powder patterns, with variable nutation angles β acting on a fully polarized initial state where only the ground state is populated (T_{spin}(^{2}H) = 0 K). A quasi-pure single-transition spectrum is obtained for β < 20°, corresponding to one of the two 'lobes' or 'cusps' of the Pake pattern. For 160° < β < 180°, the other lobe is favored, while for β = 90°, one obtains a superposition of two symmetrical lobes. The relevant parameters were C_Q = 170 kHz and η_Q = 0, whereas the anisotropic chemical shift was neglected. b) Density matrices and energy level diagrams for the bottom and top (blue) single-transition spectra of (a).

All simulations of Figure 3.1a were calculated with Simpson [88] and involved powder averaging over 4180 crystallite orientations sampled with the ZCW scheme [89-91], named after inventors

Zaremba, Conroy, and Wolfsberg. The ZCW is a method of selecting orientations in order to obtain accurate powder averages [92]. Ideal pulses were assumed in these simulations.

3.3. Experimental measurements

A sample of 300 µL containing 60% ethanol-d_6, 30% D_2O, 10% H_2O, and 40 mM TEMPOL was placed in the solenoidal coil of the home-built low-temperature broadband NMR probe described in chapter 2. The probe was inserted into the 6.7 T polarizer. To acquire the ^2H signals shown in this chapter, the X channel was tuned and matched at 43.8 MHz.

Figure 3.2 shows experimental ^2H spectra obtained with quadrupolar echoes [4, 5] excited by an 18° - τ - 18° - τ sequence combined with phase-cycling in the manner of Exorcycle [3] in order to select the coherence transfer pathway [93] $p = 0 \rightarrow p = +1 \rightarrow p = -1$. Although such small-angle quadrupolar echoes do not achieve complete refocusing of either linear or quadratic inhomogeneities, which is best achieved by using a refocusing pulse [77, 82] with β = 90°, they nonetheless result in reasonably undistorted line shapes that are much easier to interpret than those excited by a pulse-acquire sequence [78]. These echoes remove distortions due to acoustic ringing of the coil during the detection (in addition, they allow one to get rid of background signals, especially present when observing ^1H [79, 80, 94, 95]).

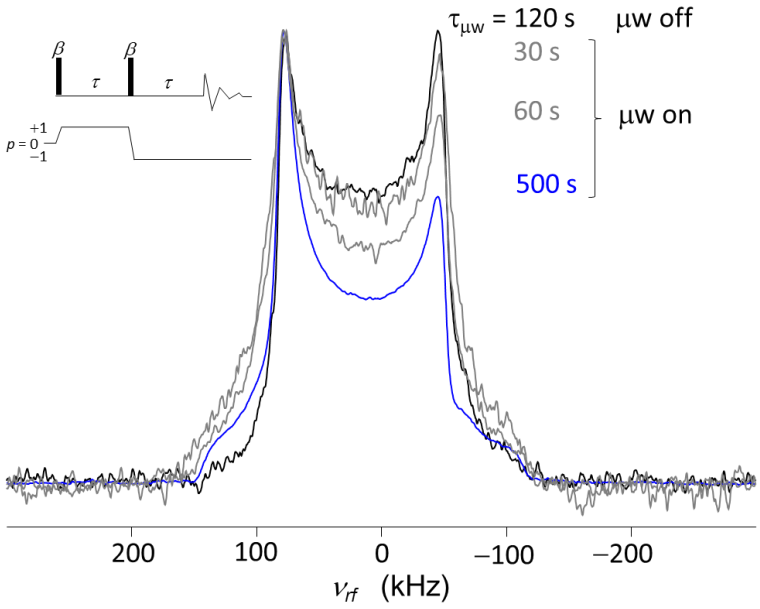

Figure 3.2- Experimental ^2H spectra of a sample consisting of 300 µL of 60% ethanol-d_6, 30% D_2O, 10% H_2O, and 40 mM TEMPOL, obtained with an exorcycled $\beta - \tau - \beta - \tau$ quadrupolar echo sequence with β = 18° in a field B_0 = 6.7 T where $\upsilon_0(^1H)$ = 285.3 MHz and $\upsilon_0(^2H)$ = 43.8 MHz. After activating the microwave irradiation for a duration $\tau_{\mu w}$, a progressively more pronounced asymmetry of the quadrupolar 'Pake pattern' is obtained as the polarization builds up. For sensitivity reasons, the black spectrum without microwave irradiation was acquired by averaging 16 echoes at T_{sample} = 4.0 K with β = 36° (τ_P = 2 µs). All other spectra were acquired at T_{sample} = 1.3 K as a function of the duration of the microwave irradiation $\tau_{\mu w}$ = 30, 60, and 500 s by averaging only 4 phase-cycled echoes with β = 18° (τ_p = 1 µs).

The black spectrum in Figure 3.2 was acquired without microwave irradiation at T_{sample} = T_{spin} = 4.0 K and results in a symmetric quadrupolar pattern. When the sample temperature is lowered to T_{sample} = 1.3 K, and the microwave irradiation with a frequency suitable to induce positive DNP is switched on, a progressive asymmetry of the line shape builds up, revealing the lowering of the spin temperature (T_{spin} << T_{sample}), or, equivalently, the build-up of a hyperpolarized state. As expected, the signal-to-noise ratio also improves as T_{spin} decreases. The highest polarization achieved in this series is shown in blue, whereas spectra obtained at intermediate spin temperatures are shown in grey.

Our sample contains a variety of deuterated groups such as CD_3, CD_2, and OD of ethanol-d_6 (60%) and D_2O (30%). Nonetheless, a single well-defined Pake pattern is obtained in these experiments, indicating that, in the absence of motional narrowing, the quadrupolar parameters are very similar in different molecular environments, at least within the homogeneous line width of ca. 7 kHz. This is also true for the isotropic chemical shifts and isotropic parts of the second-order quadrupole coupling of ^{2}H that typically span ca. 10 ppm (ca. 0.44 kHz at B_0 = 6.7 T) [96]. Numerical fits of the ^{2}H line shape (which will be discussed in the next section) acquired without microwave irradiation yielded C_Q = 170 kHz, η_Q = 0 and a line broadening of 7 kHz, in remarkable agreement with those of isolated ^2H_2O molecules trapped in solid barium chlorate [4]. The broadening may be due in part to homo- and heteronuclear dipolar couplings.

Figure 3.3 shows typical build-up profiles of the integrals of ^{2}H signals under microwave irradiation. A positive enhancement is induced by saturation of the low-frequency lobe of the EPR line of TEMPOL at 187.9 GHz, i.e., of the part of the EPR spectrum that upon saturation leads to a positive enhancement of the nuclear transitions. The top panel of Figure 3.3 indicates how the microwave frequency and amplitude are switched. When the frequency $\upsilon_{\mu w}$ drops to zero, this means that the microwave source is turned off. A single echo excited by a 27° - τ - 27°- τ echo sequence was acquired in each case, since a complete four-step phase cycle cannot be carried out while the polarization builds up. As a result, ideal refocusing of quadrupolar and shift interactions was not achieved in these spectra, thus resulting in somewhat distorted patterns. Nonetheless, the integrals over the powder patterns suffice for the purpose of monitoring the evolution of the hyperpolarization as it builds up over time. The subsequent interruption of the microwave irradiation leads to a loss of hyperpolarization due to a gradual return to the Boltzmann equilibrium at T_{sample}. The microwave frequency was then shifted to 188.38 GHz, i.e., to the high-frequency lobe of the EPR line, resulting in cooling towards negative spin temperatures. Profiles acquired at T_{sample} = 1.3 and 4.0 K, combined with frequency switching at different times to take the different time scales of the build-up curves into account, are shown by continuous and dashed black lines, respectively. The gain in signal-to-noise obtained by lowering the temperature of the sample is evident.

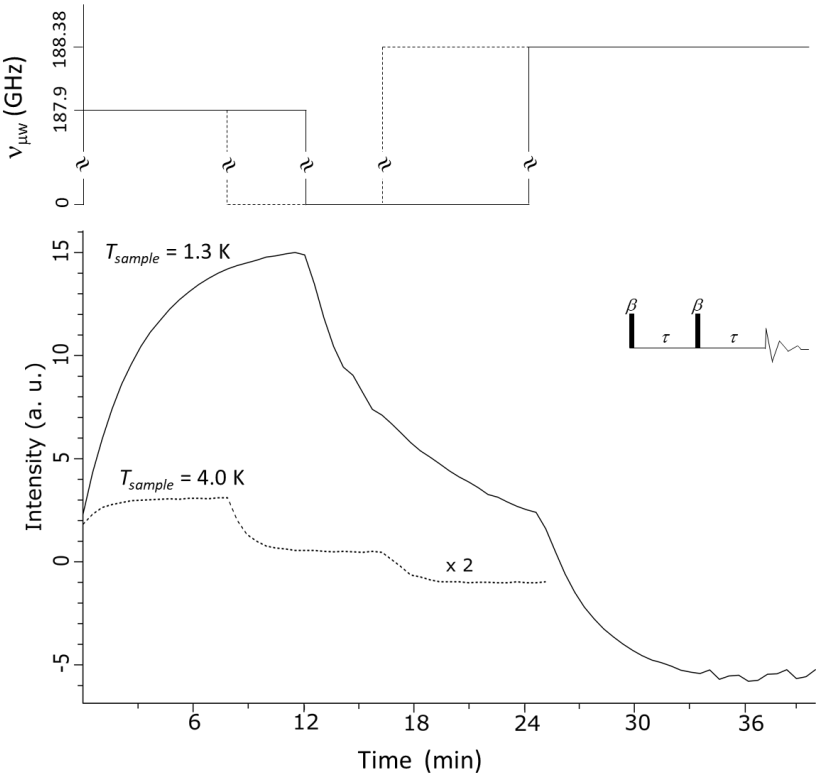

Figure 3.3- Build-up of the integrals of ^{2}H spectra under the effect of microwave irradiation for T_{sample} = 1.3 and 4.0 K, shown by continuous and dashed lines, respectively. In all cases, after an initial pre-saturating train of pulses, a ^{2}H signal was acquired every 30 s, excited by a single $\beta - \tau - \beta - \tau$ echo sequence (without phase cycling) with β = 27° and τ = 15 µs. The top panel indicates the corresponding microwave saturation frequencies at $\upsilon_{\mu w}$ = 187.9 and 188.38 GHz, for positive and negative DNP enhancements, whereas $\upsilon_{\mu w}$ = 0 indicates that the microwave source was turned off. The vertical scale of the integrals measured at T_{sample} = 4.0 K was amplified by a factor of 2.

A summary of all experimental parameters that were used to record the spectra in Figures 3.2 and 3.3 is given in the following.

The microwaves are provided by an ELVA-1 source coupled to a Virginia Diodes (VDI) frequency doubler. Frequency modulation was achieved with a saw-tooth waveform with a modulation frequency of 1 kHz to cover a bandwidth of 200 MHz to saturate a significant fraction of the EPR spectrum [56]. For positive polarization, the central microwave frequency was set to 187.9 GHz. For negative polarization, the central frequency was set to 188.38 GHz while all other parameters were kept constant.

The rf carrier was set in the center of the quadrupolar powder pattern. The rf-field amplitude for deuterium pulses was υ_1 = 50 kHz, corresponding to flip angles β = 18, 27 and 36° for pulse lengths τ_p = 1, 1.5 and 2 µs, respectively. With the exception of the build-up curves of Figure 3.3, where only single echoes were acquired, the β - τ - β_φ - τ echoes were phase cycled in four steps with φ = 0, 90, 180 and 270°. The refocusing time was τ = 15 µs and delays between subsequent

echo sequences were varied between 30 and 500 s. Prior to all experiments, a train of 100 pulses was applied to saturate the ^{2}H nuclei with τ_p = 5 µs (β = 90°) spaced by 100 µs.

3.4. ^{2}H spin temperature determination by numerical simulations

It was shown in chapter 1 that the Boltzmann polarization $P(I)$ of a nuclear spin I with a spin temperature $T_{spin}(I)$ is defined as:

$$P(I) = \tanh[\hbar\gamma_I B_0/(2k_B T_{spin}(I))]. \quad (3.1)$$

If the populations obey a Boltzmann distribution, as they should when in equilibrium with a thermal reservoir at a spin temperature of $T_{spin}(I)$, the density operator ρ_{eq} for a spin I = 1, neglecting the unobservable identity operator, can be concisely expressed as:

$$\rho_{eq} = P(I)I_z + P(I)^2 {I_z}^2. \quad (3.2)$$

Combining equations (3.1) and (3.2) leads to:

$$\rho_{eq} = \tanh[\hbar\gamma_I B_0/(2k_B T_{spin}(I))]I_z + \tanh^2[\hbar\gamma_I B_0/(2k_B T_{spin}(I))]{I_z}^2. \quad (3.3)$$

This density operator can be considered as initial condition for simulations of any spin dynamics by means of the usual Liouville-von Neumann equation $\rho(t) = U(t)\rho(0)U(t)^{-1}$, with $\rho(0) = \rho_{eq}$ for any arbitrary spin temperature.

Figure 3.4a shows the experimental hyperpolarized ^{2}H spectrum shown in the previous section (blue spectrum in Figure 3.2). The striking asymmetry of the two horns of the pattern is highlighted by a blue arrow. Figure 3.4b shows a series of spectra simulated for different values of the polarization $P(^2\text{H})$, assuming 18° - τ - 18°- τ quadrupolar echoes with realistic rectangular rf pulses (υ_1 = 50 kHz) combined with Exorcycle. The simulated spectrum that best reproduces the asymmetry observed in Figure 3.4a is shown in blue, corresponding to a spin temperature $T_{spin}(^2\text{H})$ = 3.5 mK, which amounts to a polarization $P(^2\text{H})$ = 29%. These simulations show that the absolute deuterium spin temperature and polarization can be determined with an accuracy of *ca*. ±0.5 mK and ±4%, respectively. Clearly, the use of echoes with small flip-angle pulses allows one to acquire undistorted deuterium line shapes of hyperpolarized samples. If the conditions for thermal mixing are fulfilled, then different isotopes should have the same spin temperature (e.g., $T_{spin}(^{13}\text{C}) = T_{spin}(^2\text{H})$), provided one does not employ cross polarization. Thermal mixing should prevail if the target molecules dissolved in the DNP juice are isotopically enriched in ^{13}C to facilitate ^{13}C -^{13}C spin diffusion and if the ^{13}C nuclei are abundant enough so that the electron-spin couplings are efficient [97]. In contrast to other DNP mechanisms which can be described by isolated electron-nucleus spin pairs (Overhauser and solid effects) or by a system comprising two electrons and one nucleus (cross effect), thermal mixing is more conveniently described by a thermodynamic model [98]. This occurs for high radical concentrations so that dipolar electron-electron couplings broaden the EPR line shape homogeneously. The TEMPOL concentration of 40 mM utilized in this study is similar to the doping used by Guarin et al. [97] for investigations of DNP enhancements in the thermal mixing regime.

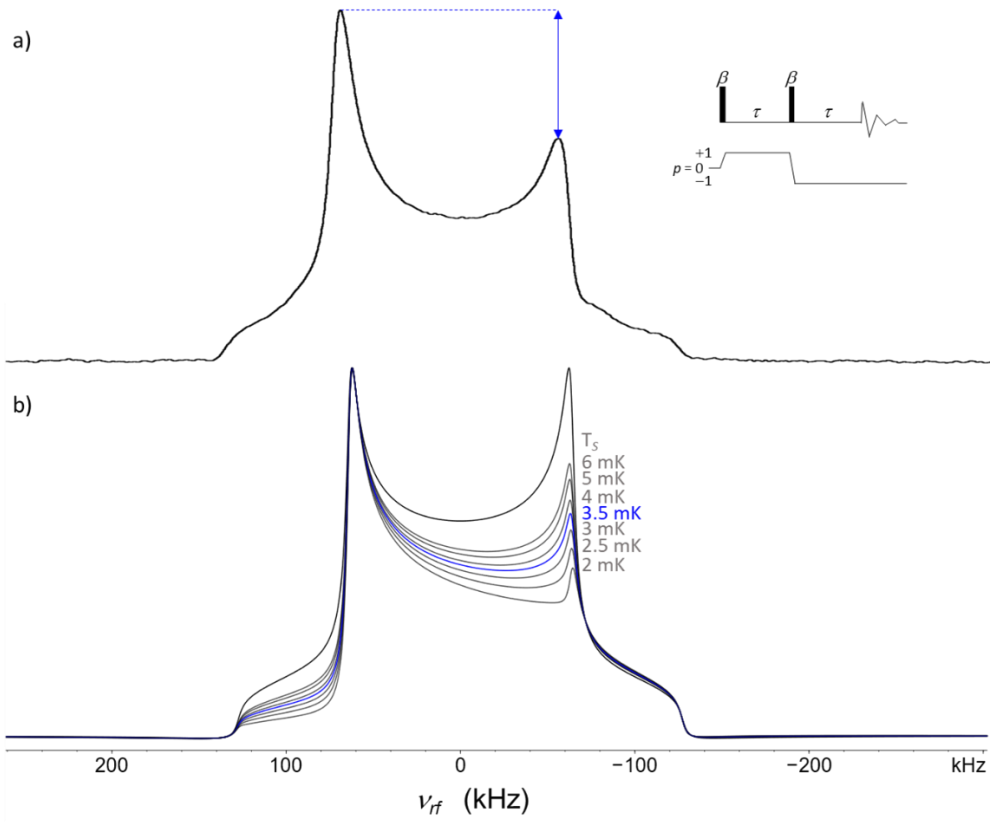

Figure 3.4- a) Hyperpolarized experimental ^{2}H spectrum shown in blue in Figure 3.2. The asymmetry between the 'horns' of the quadrupolar Pake pattern is highlighted by a blue arrow. b) Numerical simulations assuming different spin temperatures T_{spin}. The case that agrees best with the experiment in (a) is highlighted in blue, corresponding to $T_{spin}(^2\text{H})$ = 3.5 ± 0.5 mK or $P(^2\text{H})$ = 29 ± 4%.

Once again, the simulations were calculated with Simpson and involved powder averaging over 4180 crystallite orientations sampled with the ZCW scheme. Rectangular pulses with finite rf amplitudes (υ_1 = 50 kHz) were utilized for the simulations of the exorcycled echoes of Figure 3.4.

In order to extract the spin temperature T_{spin} from a line shape analysis of such asymmetric experimental deuterium spectra, a numerical fit with signals simulated for quadrupolar echoes β - τ - β - τ combined with Exorcycle acting on $\rho_{eq}(T_{spin})$ of equation (3.3) needs to be performed. This ultimately means that the main parameter to be optimized is $\rho_{eq}(T_{spin})$. Other parameters such as the quadrupolar coupling constant C_Q, the asymmetry η_Q, and the homogeneous line width can be estimated from symmetric line shapes obtained with similar 90° - τ - 90°- τ echoes on the same sample, either with or without DNP. Figure 3.5 shows that a more straightforward estimate of the spin temperature may be obtained by simply evaluating the ratio of the peak heights of the two 'horns' of the Pake pattern. The asymmetry of the quadrupolar powder pattern can be expressed by the ratio $(I_{max} - I_{min})/I_{max}$, where I_{max} and I_{min} are the peak heights of the high- and low-frequency 'horns'. The ratios shown in Figure 3.5 were obtained by varying one parameter at the time while leaving all others at their optimal value. The asymmetry

of the peak heights in the experimental spectrum of Figure 3.4a is indicated by a horizontal dashed line in Figure 3.5. The parameters C_Q and η_Q can be easily estimated prior to DNP as discussed above; they not only affect the asymmetry of the two wings of the powder pattern but also alter the splitting between the horns. The rf-field amplitude and the homogeneous line width have little effect on the estimates of T_{spin}. The (conservative) estimate ±0.5 mK of the confidence range is indicated by horizontal dashed lines.

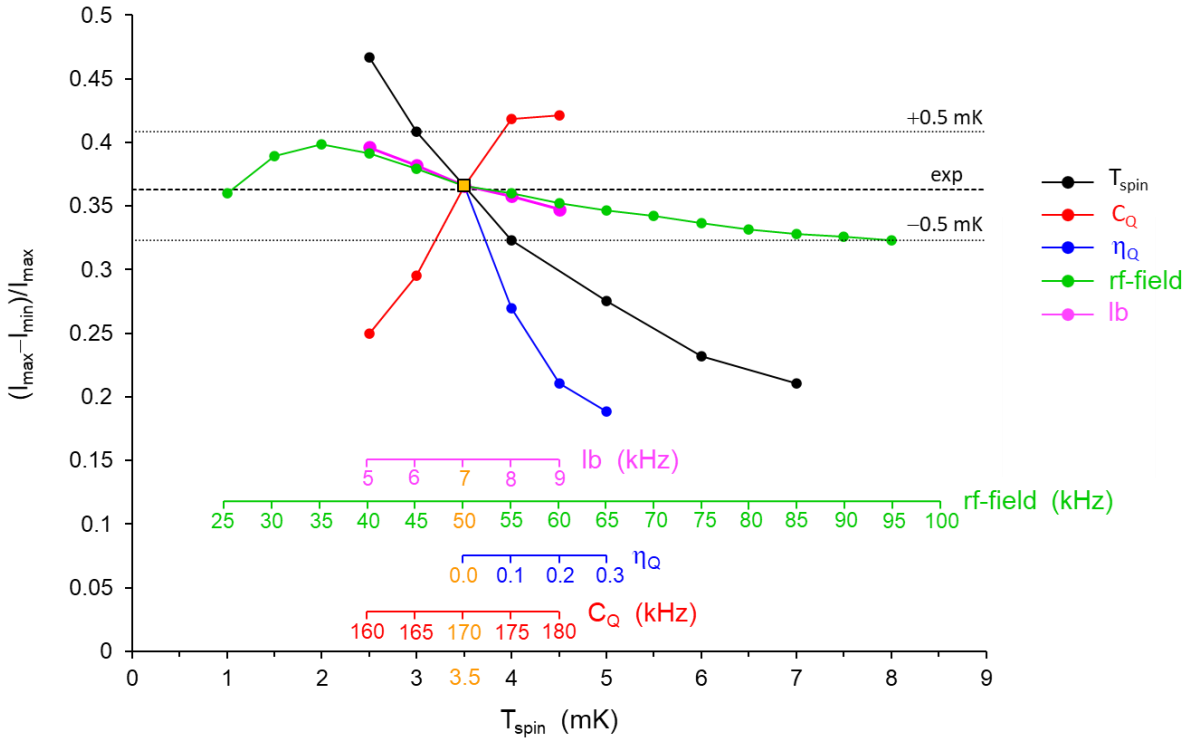

Figure 3.5- Asymmetry of simulated hyperpolarized ^{2}H quadrupolar powder patterns expressed as $(I_{max} - I_{min})/I_{max}$, where I_{max} and I_{min} are the peak heights of the high- and low-frequency 'horns' of Pake patterns obtained by numerical simulations of 18° - τ - 18°- τ quadrupolar echoes combined with Exorcycle for different parameters. Powder averaging was performed over 4180 crystallite orientations and realistic rectangular pulses were taken into account. Black, red, blue, green, and cyan data refer to the spin temperature T_{spin}, the quadrupolar coupling constant C_Q, the asymmetry parameter η_Q, the rf-field strength, and the homogeneous line broadening *lb*, respectively. The experimental value of the asymmetry seen in Figure 3.4a is indicated by a horizontal dashed line. Thin dashed horizontal lines indicate an uncertainty interval of ±0.5 mK. The optimal set of parameters is indicated in orange.

3.5. Chapter conclusions

Dynamic nuclear polarization of samples at low temperatures, typically between 1.2 and 4.2 K, allows one to achieve spin temperatures as low as 2 mK so that for many nuclear isotopes the high-temperature approximation is violated for the nuclear Zeeman interaction. This leads to characteristic asymmetries in powder spectra.

We have investigated the quadrupolar line shapes due to ^{2}H nuclei in a typical frozen DNP juice. The asymmetry of experimental hyperpolarized powder patterns, observed in the presence of microwave irradiation by means of small flip-angle quadrupolar echoes combined with phase-cycling, is in very good agreement with simulations. Quadrupolar echoes excited by small flip-angle pulses do not destroy the hyperpolarization and yield undistorted powder patterns in hyperpolarized solid samples. The comparison of experimental and simulated line shapes allows one to determine the absolute spin polarization or, equivalently, the absolute spin temperature of the deuterium nuclei. If the conditions of thermal mixing are fulfilled, the spin temperatures of different nuclei such as ^{6}Li, ^{13}C, ^{15}N, ^{31}P, etc., should be equal to the spin temperature $T_{spin}(^{2}\mathrm{H})$ of the deuterium nuclei.

Chapter 4

4. A d-DNP setup to eject and transfer frozen solid samples

4.1. Introduction

Building a suitable and efficient low-temperature NMR probe for the new bullet-DNP [2] system was only the first step. There are other parts in such a system that need to be designed and optimized one by one in order for the complete setup to work.

The process starts with sample preparation and continues with the insertion of the sample into the polarizer while avoiding contaminations that may occur because of the introduction of air into the cryostat. Once the polarization is performed, as discussed in chapters 2 and 3, the sample is ejected and transferred to the spectrometer. This transfer is an important aspect and it has to be done as fast as possible while the transfer path is protected by a magnetic field to preserve as much polarization as possible (since the relaxation increases considerably at very low fields). Finally, the solid sample needs to be quickly and homogeneously dissolved upon arrival before NMR detection. A flowchart summarizing all these steps is shown in Figure 4.1.

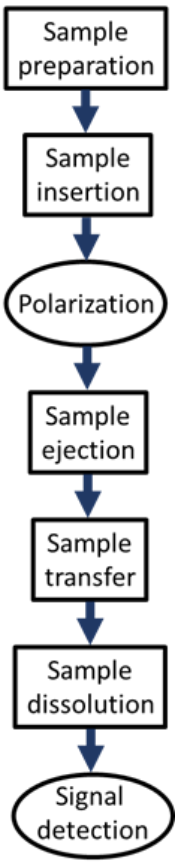

Figure 4.1- A flowchart of all the steps for an operational bullet-DNP setup.

4.2. Sample preparation, insertion and ejection

Since the polarizer is usually at about 4 K when inserting a sample, the leakage of even a small amount of air into the system may lead to a complete blockage inside the probe. If this happens, the probe needs to be taken out of the polarizer, warmed up, and dried before inserting it back again. Consequently, a strict procedure has been developed through trial and error for sample preparation, insertion, and ejection in order to decrease the chance of any contamination.

Since a naked frozen sample proved to be impractical due to fast melting, a frozen sample inside a Teflon cylinder showed promise as the best alternative for our system. Teflon does not contain any protons and hence does not contribute to the proton background signal. Small open-ended hollow Teflon cylinders are cut in a manner that is shown in Figure 4.2a for this purpose. Depending on their length, these cylinders can hold 20- 40 µL of sample. They are cut from Teflon tubes with outer diameter of 2 mm and inner diameter of 1.8 mm.

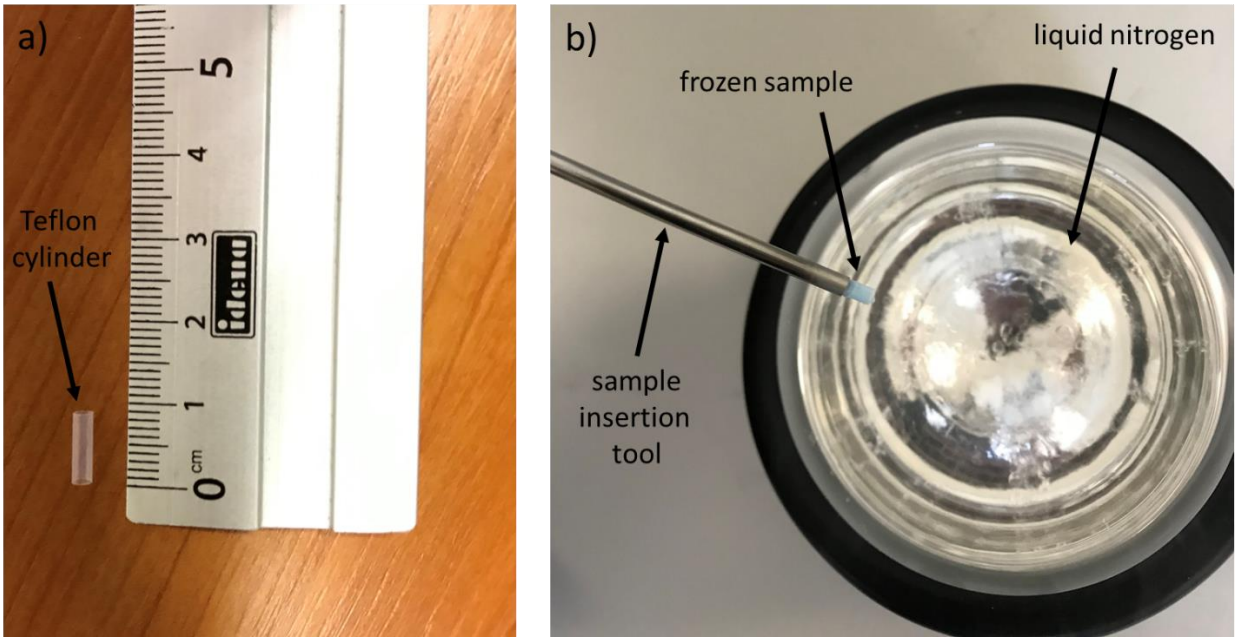

Figure 4.2- a) An empty Teflon cylinder next to a ruler for comparison. b) A frozen sample drawn out of liquid nitrogen and placed in the sample insertion tool.

After the sample ('DNP juice') is injected into a Teflon cylinder shown in Figure 4.2a, it is immediately immersed in liquid nitrogen for vitrification. The frozen sample is then placed in a sample insertion tool shown in Figure 4.2b. The sample insertion tool is a piston-like device that consists of a stainless-steel tube with outer diameter of 3 mm and inner diameter of 2.2 mm and a stainless-steel rod with a diameter of 2 mm. The frozen sample is placed in the tube and kept frozen in liquid nitrogen. This sample insertion tool is then inserted in the probe and the frozen sample is pushed out of the tube with the rod. This process needs to be done quickly, so that the sample does not melt while moving from liquid nitrogen (about 77 K) into the NMR coil (about 4 K).

A device assembled on top of the probe allows for the contamination-free insertion and ejection of the sample. This device is shown in Figure 4.3.

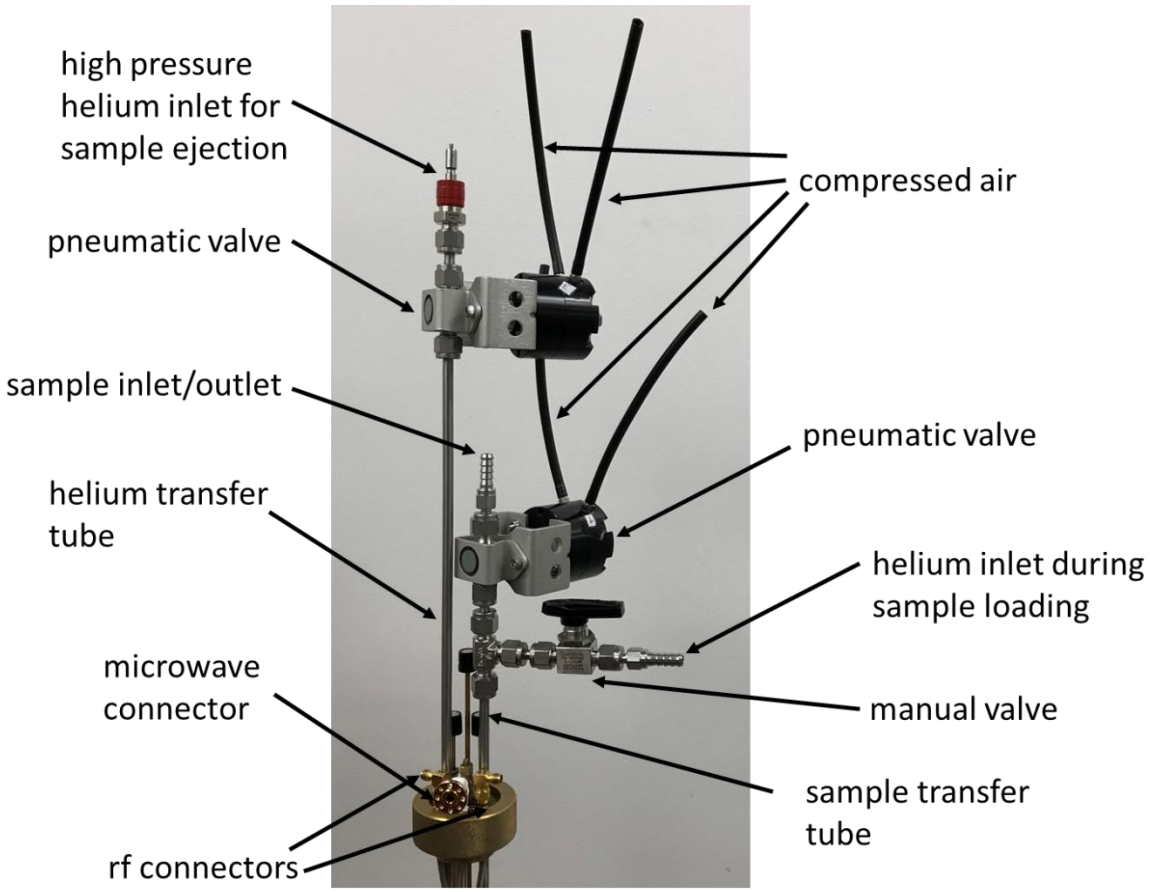

Figure 4.3- Pneumatic system at top of the probe for controlled sample loading, and post-DNP ejection.

Two pneumatic valves are present at the ends of two metal tubes. The shorter tube (right) is for insertion and ejection of the sample while the longer tube (left) serves as an inlet for helium gas to eject the sample. The pneumatic valves are operated by compressed air with minimum 5 bar of pressure that goes through one of the four black flexible tubes shown in Figure 4.3. The flow of compressed air and consequently the operation of the pneumatic valves are managed by a control unit that is described later in this chapter.

The manual helium inlet valve assembled on the sample transfer tube prevents contaminations. A helium gas line is connected to it. At the time of sample insertion, this manual valve is opened and the pneumatic valve on the sample transfer tube is opened right after. At this point, continuous helium flow is going through the “T” junction. This flow, which is going out of the sample transfer tube, prevents air from going in. The sample insertion tube (Figure 4.2) containing the sample is then inserted into the sample transfer tube through the “T” junction. At this point, the sample is pushed out and the empty sample insertion tool is pulled back. The helium flow pushes the sample down into the coil. However, to make sure that the sample is located at the desired position in the coil, a PEEK rod with diameter of 3.2 mm is used. This rod is used as a kind of “plunger”, and is marked with the exact length from the top until the coil.

After the polarization is performed, a pressurized helium line is connected on top of the helium transfer tube (Figure 4.3) in order to eject the sample. This pressure is usually between 6 and 9 bars. When the ejection is triggered, both pneumatic valves are opened and sample is shot out of the sample transfer tube.

4.3. Sample transfer

Fast and reliable transfer of the frozen solid samples from the polarizer to the spectrometer, while sheltering the transfer path with a magnetic field to avoid any zero crossings and low field regions, is an essential part of a bullet-DNP apparatus. This is due to very short relaxation times caused by dipolar interactions between radicals and target nuclei in while the compact sample (10-50 µL) is in the solid state.

A polyethylene tube with inner diameter of 4 mm and outer diameter of 7 mm connects the polarizer to the spectrometer. This tube is placed inside a magnetic tunnel with a homogeneous field of 0.34 T. This magnetic tunnel for transferring solid samples is separate from an already existing magnetic tunnel in our lab for transferring liquids [57]. It is wide enough to accommodate the transfer tube with 7 mm of outer diameter and extends all the way from top of the d-DNP probe to the entrance of the bore of the detection magnet. A picture of the setup with the two magnetic tunnels can be seen in Figure 4.4.

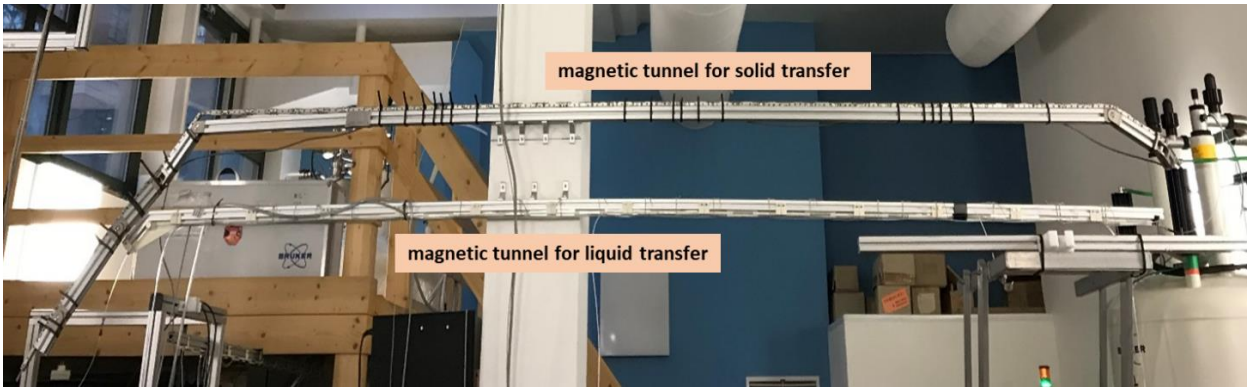

Figure 4.4- The view of two magnetic tunnels in our lab. The upper one is for transferring solids and the lower one is for transferring liquids.

The magnetic tunnel for solid transfer is built according to a Halbach array (Figure 4.5a). Permanent magnets made of N48M alloy with dimensions 0.25 X 1 X 10 cm were used in the array. Two directions of magnetization (Figure 4.5b) for the bar magnets were needed in order to achieve an array with a homogeneous field of 0.34 T inside. The magnets were mounted on aluminum square tubes with dimensions 100 X 1 X 1 cm using epoxy glue (Figure 4.5c). The distance between the polarizer and spectrometer is approximately 4.5 m. As the dimensions of the aluminum square tubes suggest, the magnetic tunnel has been built in several pieces. These pieces of tunnel were then assembled sequentially with minimum space in between on a separately built structure made out of aluminum profiles.

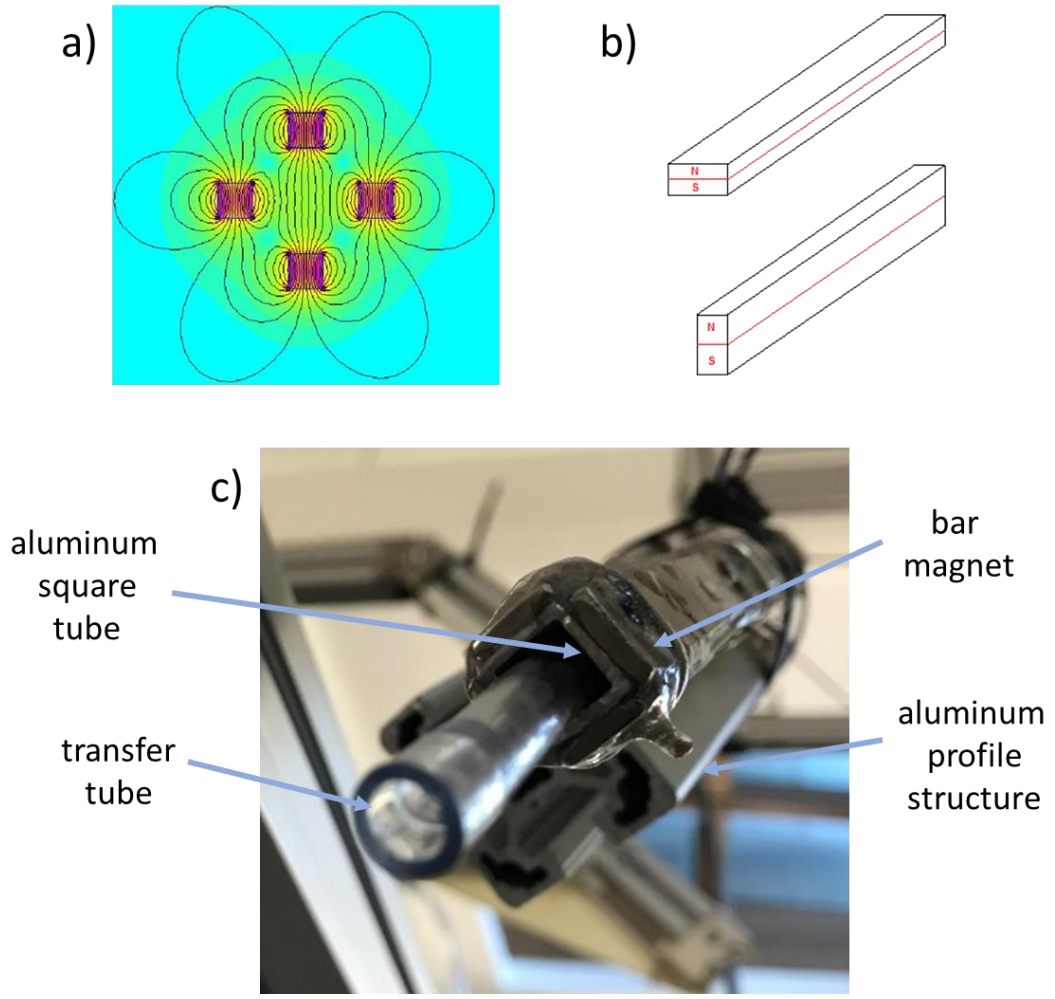

Figure 4.5- a) Halbach array taken from [99]. b) Magnetization direction of the bar magnets used to build the magnetic tunnel. c) Assembled magnetic tunnel and transfer tube mounted on the aluminum profile structure.

In order to measure the sample position and average transfer speed, two optical sensors (TT Electronics) are used. One of these sensors is mounted on top of the d-DNP probe at the entrance of the magnetic tunnel and the other one is set up at the bore entrance of the spectrometer. The optical sensor mounted on the transfer tube is shown in Figure 4.6.

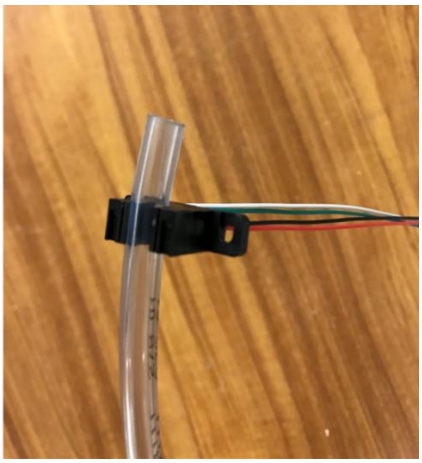

Figure 4.6- One of the two optical sensors for the measurement of the sample position and transfer speed which is fixed around the transfer tube.

When a sample passes through the tube, the light generated by the optical sensor is disrupted and an electric signal is sent out to that effect. This signal is received by a programmable circuit board (Arduino), which is part of a control unit that manages the probe's pneumatic valves in addition to the optical sensors. The Arduino itself is controlled by a graphical user interface (GUI) programmed in MATLAB. Different parts of the home-built control unit are shown in Figure 4.7.

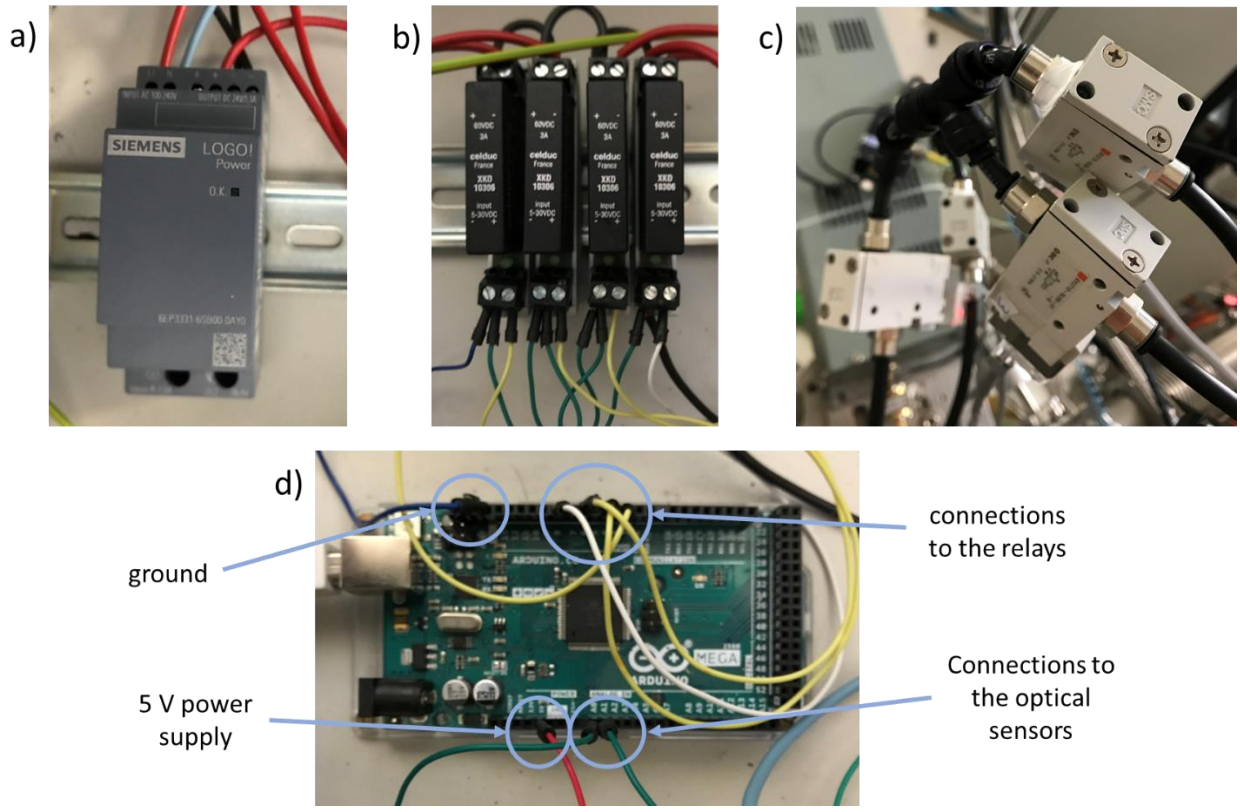

Figure 4.7- Different parts of the control unit. a) 24 V power supply. b) Solid-state relays. c) Solenoid valves. d) Arduino circuit board.

A Siemens 24 V power supply (Figure 4.7a) transforms 240 V AC to 24 V DC which is the required input for the Celduc solid-state relays (Figure 4.7b). Relays are electronic switching devices. There are 4 relays in the current setup (two for each pneumatic valve) and each of these is connected to an SMC solenoid valve (Figure 4.7c). Each of the solenoid valves is connected to a compressed air line attached to the pneumatic valves on top of the probe (Figure 4.3). When a relay is turned on, it will provide 24 V to its corresponding solenoid valve. Consequently, the solenoid valve opens up and compressed air reaches a pneumatic valve and will either open or close it. The relays are connected to an Arduino which controls them and consequently controls the pneumatic valves. This Arduino (Figure 4.7d) also controls and supplies the needed 5 V to the optical sensors described earlier.

4.4. Sample dissolution

According to the optical sensors, it takes 100 to 250 ms for the sample to travel the distance of about 4.5 m between the polarizer and the spectrometer. As soon as the sample has passed the second sensor, the pneumatic valves are automatically closed. At this point, the sample should ideally be quickly and efficiently extracted from the Teflon cylinder and dissolved and mixed in a corresponding solvent. Although such a dissolution system is essential to achieve the best results, we decided to proceed without one for the time being to perform a few preliminary experiments and record a few proof-of-concept spectra. For this purpose, the transfer tube is simply inserted into a 10 mm NMR tube that is placed in the NMR coil of the spectrometer. The sample, and its Teflon vessel, is dropped into a solvent waiting in the NMR tube. This setup is shown in Figure 4.8.

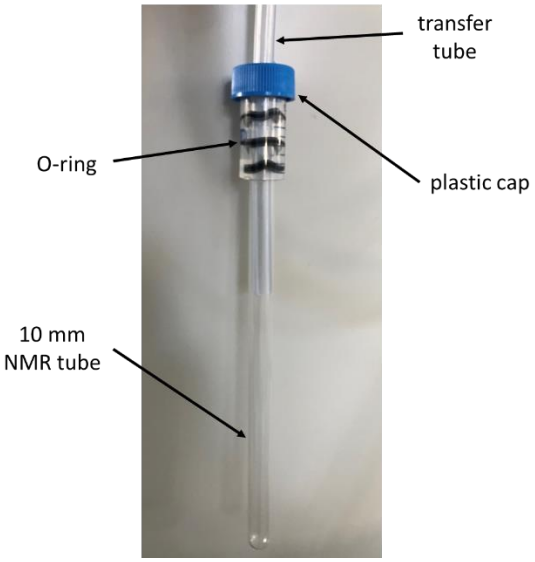

Figure 4.8- The connection of the transfer tube with a 10 mm NMR tube.

A plastic cap is fixed on top of the NMR tube with the help of 3 O-rings to keep the transfer tube in place during the sample transfer.

There are many drawbacks to this setup. The sample stays on top of the solvent in the NMR tube so the melting and mixing is neither fast nor efficient. In addition, the existence of the Teflon cylinder inside the NMR coil distorts the shimming. However, even imperfect measurements with such a setup can provide us with very useful information about the whole system.

Although most of the preliminary results shown in the next section have been recorded with this simple direct setup, towards the end of this research, we designed and implemented a better dissolution system (or at least part of it). A device that we called “bullet catcher” was assembled to stop the Teflon vessel while shooting its content in an NMR tube. This device is shown in Figure 4.9a alongside its schematic drawing (Figure 4.9b) for better illustration.

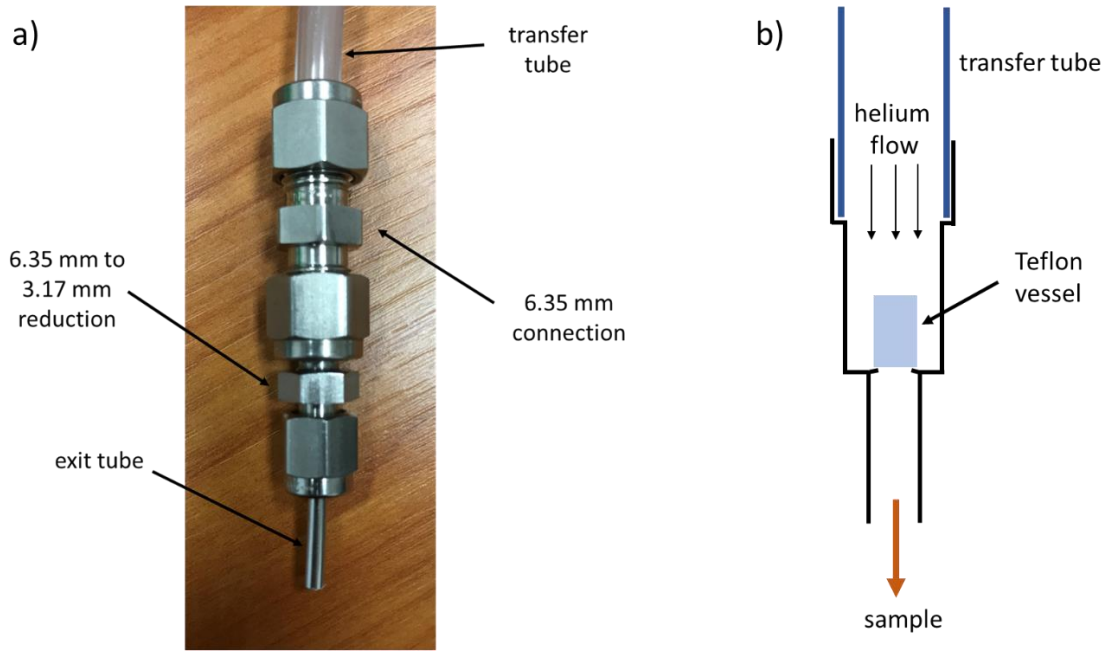

Figure 4.9- a) Actual view and b) a schematic drawing of a cross section of the “bullet catcher” apparatus for an efficient dissolution.

As the sample is pushed through the transfer tube, instead of going directly into the NMR tube, it arrives into the bullet catcher device. It goes through the 6.35 mm connection without any interruption and then the Teflon vessel is stopped at the entrance of the exit tube inside the 6.35 mm to 3.17 mm reduction part. The exit tube is just a standard stainless tube with outer diameter of 3 mm and inner diameter of 2.2 mm. This tube is intentionally slightly deformed at the entrance (inside of the reduction part), to stop the Teflon cylinder (with outer and inner diameters of 2 mm and 1.8 mm respectively) while letting the sample content pass. The content is scattered into the solvent waiting in a 10 mm NMR tube inside the spectrometer for detection. This method keeps the Teflon cylinder outside of the detection coil and expedites the dissolution. However, the strong helium pressure needed to push out the sample content often disturbs the liquid inside the NMR tube.

4.5. Preliminary results

In this section, several spectra showing hyperpolarized signals after dissolution in liquid state are shown. These results are acquired by using the newly built bullet-DNP setup. All the procedures and tools which were described before have been used to detect these spectra. The measurements were performed on an 9.4 T (400 MHz proton frequency) Bruker spectrometer equipped with a 10 mm BBO probe.

To demonstrate the difference between two dissolution methods with direct injection (Figure 4.8) and the bullet catcher (Figure 4.9), two experiments were performed. In both experiments, 25 µL of a sample containing 60% DMSO-d_6, 30% D_2O, 10% H_2O with 1.5 M sodium acetate (with 99% ^{13}C in the carboxylic position) and 10 mM TEMPOL was inserted in the polarizer. In the polarizer, the same CP sequence was performed in both experiments at 4 K. After sample transfer through the magnetic tunnel and dissolution in 1.1 mL D_2O, the ^{13}C spectra were obtained by simple pulse-acquire experiments with 30° rf pulses applied every half a second. The spectra with the largest peak integrals are shown in Figure 4.10. The black spectrum is recorded after direct dissolution and the red spectrum is obtained by using the bullet catcher for dissolution.

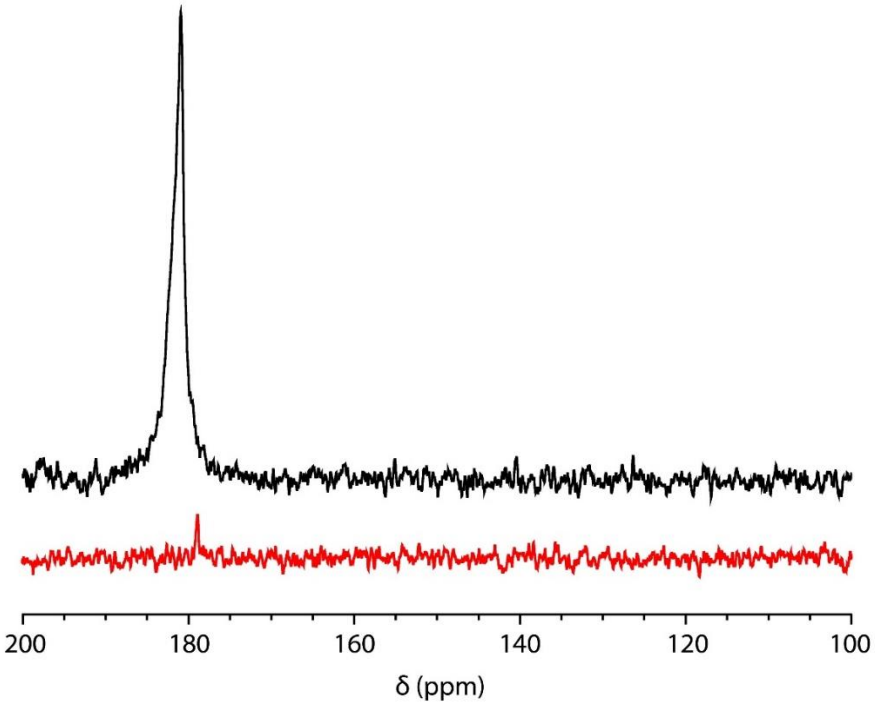

Figure 4.10- NMR spectra of ^{13}C recorded using 30° pulses with direct dissolution (black) and with bullet catcher dissolution (red). The 25 µL samples contained 60% DMSO-d_6, 30% D_2O, 10% H_2O with 1.5 M sodium acetate (with 99% ^{13}C in the carboxylic position) and 10 mM TEMPOL. They were polarized at 4 K, transferred through the magnetic tunnel, and dissolved in 1.1 mL D_2O on arrival.

As can be seen, the bullet catcher is not optimized yet since most of the sample stayed in its exit tube rather than entering the NMR tube (hence the weak signal). However, a comparison of these two spectra reveals some useful information. When using direct dissolution method, the Teflon

cylinder containing sample is dropped on top of 1.1 mL of D_2O inside the NMR coil. This affects the shimming and creates susceptibility differences, causing a slight shift in position of the peak. In addition, the black spectrum is much broader (about 140 Hz) than the red spectrum (about 35 Hz). This could be attributed to the dissolution speed. The sample is not dissolved instantly on arrival. It takes about 7 s for the sample to melt inside the vessel and to slowly diffuse out into the NMR tube. Detection of a compact bolus close to the Teflon cylinder may be the reason behind the width of the peak.

The bullet catcher shows promise in that it gives a narrower peak which is needed to extract useful and complex information from the NMR spectra. An optimized and efficient dissolution system based on the bullet catcher is currently under development in our lab. However, in this work, all the following results were acquired by direct dissolution.

To investigate the efficiency of the magnetic tunnel, two identical experiments were performed with and without the magnetic tunnel. In both experiments, the same vessel was impregnated with 25 µL of sample containing 60% DMSO-d_6, 30% D_2O, 10% H_2O with 1.5 M sodium acetate (with 99% ^{13}C in the carboxylic position) and 5 mM TEMPOL. The samples were hyperpolarized at 4 K to the same level using CP and after sample transfer into an NMR tube containing 1.4 mL D_2O, ^{13}C spectra were recorded by 30° pulses applied every half a second. The spectra with the largest peak integrals are shown in Figure 4.11. The black and red spectra have been obtained after sample transfers with and without the magnetic tunnel, respectively.

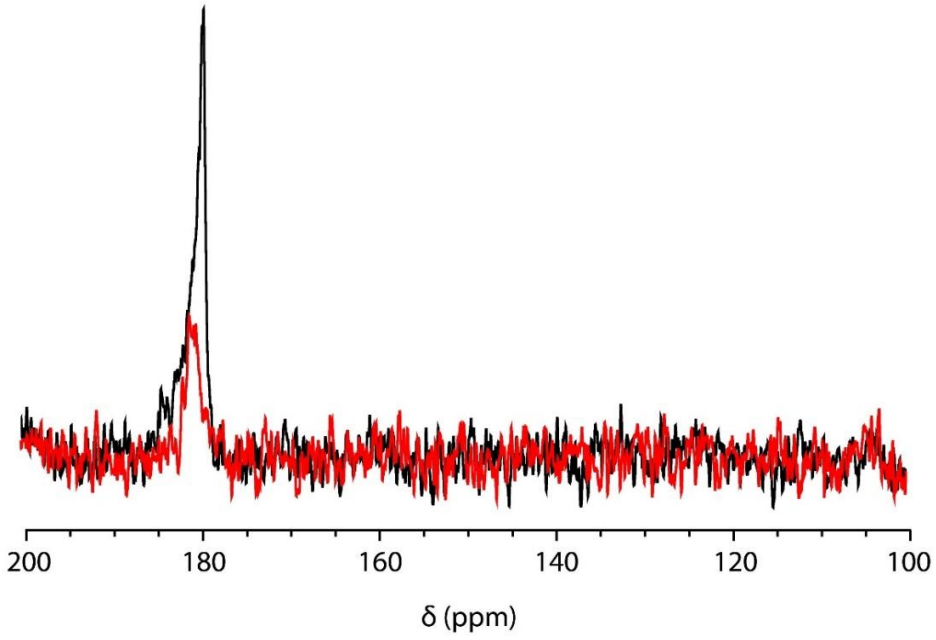

Figure 4.11- NMR spectra of ^{13}C recorded using 30° pulses. The black spectrum is recorded using the magnetic tunnel during transfer while the red spectrum is obtained after sample transfer without the tunnel. The 25 µL samples contained 60% DMSO-d_6, 30% D_2O, 10% H_2O with 1.5 M sodium acetate (with 99% ^{13}C in the carboxylic position) and 5 mM TEMPOL. They were polarized at 4 K and dissolved in 1.4 mL D_2O on arrival.

The magnetic tunnel improved the signal by about a factor of 3. Before building the magnetic tunnel, the hyperpolarized signal after transfer was not strong enough to detect with 10° pulses, and consequently we routinely used 30° pulses to observe a signal. However, application of 30° pulses leads to a fast decay of the polarization. After the implementation of the magnetic tunnel, 10° pulses could be used. The difference of 10° and 30° pulses on the polarization decay is illustrated in Figure 4.12.

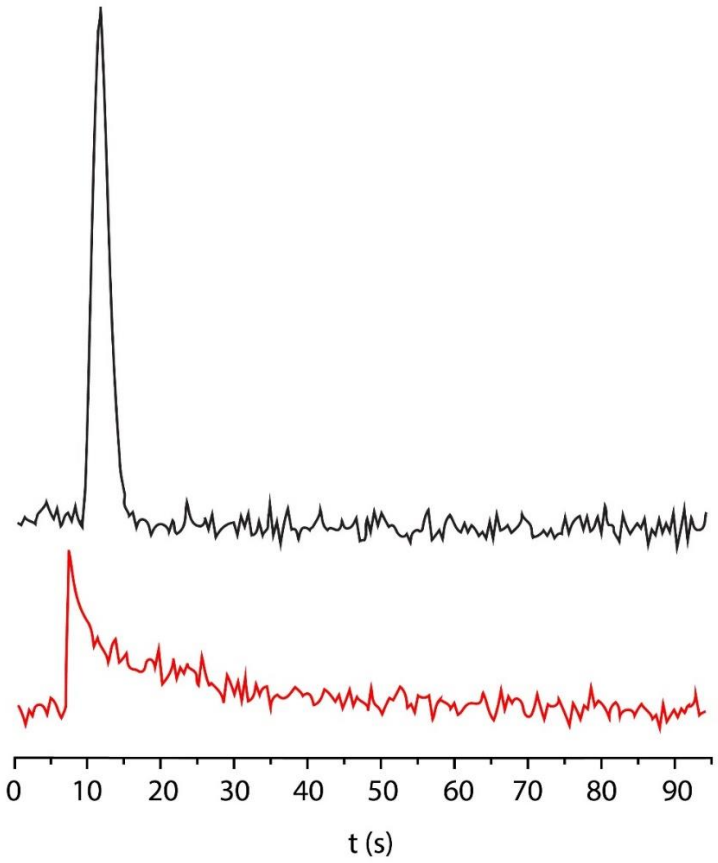

Figure 4.12- The integrals of the ^{13}C spectra obtained at 0.5 s intervals with 30° detection pulses (black) and 10° detection pulses (red). The 25 µL samples contained 60% DMSO-d_6, 30% D_2O, 10% H_2O with 1.5 M sodium acetate (with 99% ^{13}C in the carboxylic position) and 10 mM TEMPOL. They were polarized at 4 K, transferred through the magnetic tunnel, and dissolved in 1.4 mL D_2O on arrival.

At the beginning of the two spectra there is a period when no signal is detected. This is when the detection in the spectrometer has started but the sample has not been ejected yet. When the sample is transferred to the NMR tube, there is a jump in the integrals of the intensities of the spectra obtained at 0.5 s intervals. The black spectrum (30° pulses) shows a fast decay. In about 7 seconds (14 pulses) after the detection of the first signal, the polarization disappears. Even though detection with 10° pulses results in lower intensity signals, they last longer. The red trace shows that even at about 50 s (100 pulses) after the arrival of the sample, hyperpolarized signal

is still detected. The longitudinal relaxation time (T_1) was measured using inversion recovery and is approximately 66 s.

If we take a closer look into the first 5 hyperpolarized signals detected during the experiment that resulted in the red spectrum in Figure 4.12, we see the shape of the peaks evolving. This effect is shown in Figure 4.13.

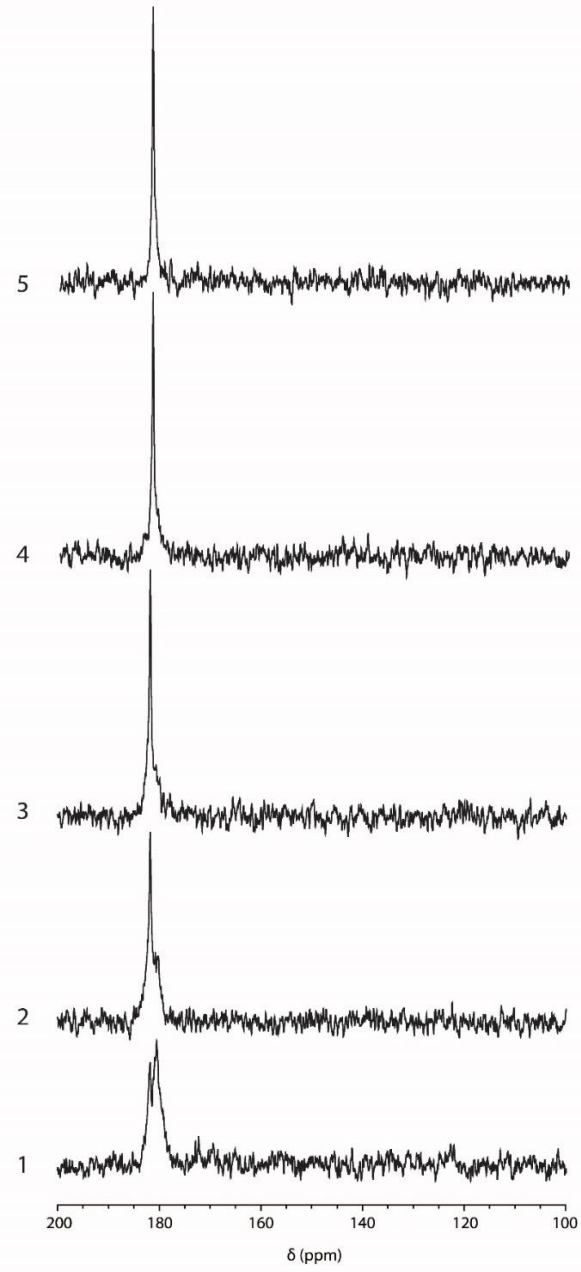

Figure 4.13- The evolution of 5 consecutive ^{13}C signals beginning with the first detected hyperpolarized signal after arrival of the sample. The 25 µL sample contained 60% DMSO-d_6, 30% D_2O, 10% H_2O with 1.5 M sodium acetate (with 99% ^{13}C in the carboxylic position) and 10 mM TEMPOL. It was polarized at 4 K, transferred through the magnetic tunnel, and dissolved in 1.4 mL D_2O on arrival while 10° pulses were used for detection.

In the first spectrum, a peak with two shoulders is observed. The right shoulder is more intense. In the second spectrum, the right shoulder is decreased in intensity while the left shoulder is more intense. This trend continues in third, fourth and fifth spectra. In the fifth spectrum the right shoulder has completely disappeared and the left shoulder is at its highest intensity. This effect is probably caused by the slow dissolution process. Since it only happens at the very beginning, it can be imagined that there are different susceptibilities depending on the state and whereabouts of the sample. This effect illustrates the flaws in the current dissolution process and emphasizes the need of a better dissolution system.

All previous spectra were acquired after dissolution of solid samples that were hyperpolarized in the polarizer at 4 K. As is widely known and shown in chapter 2, polarization at 1.3 K leads to higher levels of polarization. To investigate if the boost in the polarization level in the polarizer translates into a more intense signal after dissolution, two experiments were performed. In both experiments, 25 µL of sample containing 60% DMSO-d_6, 30% D_2O, 10% H_2O with 1.5 M sodium acetate (with 99% ^{13}C in the carboxylic position) and 10 mM TEMPOL was inserted in the polarizer. In the polarizer, the same CP sequence was performed on both of them at different temperatures of 4 K and 1.3 K. After sample transfer through the magnetic tunnel and dissolution in 1.4 mL D_2O, the ^{13}C spectra were obtained by 10° pulses applied every half a second. The spectra with largest peak integrals among them are shown in Figure 4.14. The black and red spectra result from the samples polarized at 1.3 K and 4 K, respectively.

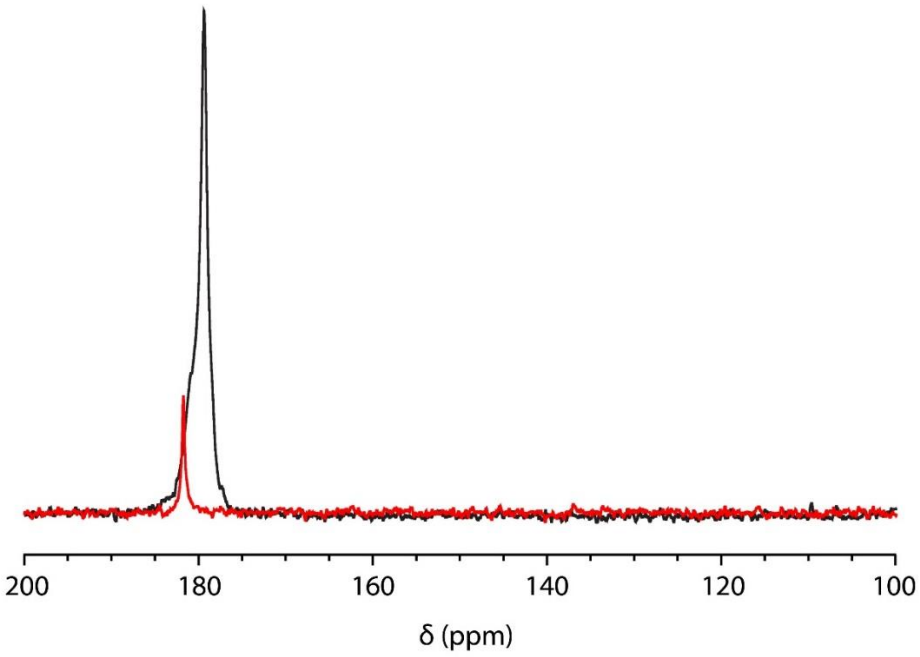

Figure 4.14- NMR spectra of ^{13}C recorded using 10° pulses after sample polarization at 1.3 K (black) and 4 K (red). The 25 µL samples contained 60% DMSO-d_6, 30% D_2O, 10% H_2O with 1.5 M sodium acetate (with 99% ^{13}C in the carboxylic position) and 10 mM TEMPOL. They were transferred through the magnetic tunnel, and dissolved in 1.4 mL D_2O on arrival.

To calculate the enhancement factors achieved in each experiment, the thermal equilibrium signals of each sample after dissolution were accumulated. By integrating the thermal equilibrium peaks and comparing them with the peaks in Figure 4.14, the enhancement factors $\varepsilon_{black} \simeq 188$ and $\varepsilon_{red} \simeq 21$ were calculated for the polarized samples at 1.3 and 4 K, respectively. It appears that for these samples, after dissolution, a gain of about factor 9 was achieved by polarizing at 1.3 K in comparison to 4 K.

In these examples, achieving a higher polarization level in the polarizer by keeping the radical concentration constant, had a positive effect on the signal detection after dissolution. However, performing many experiments with different samples showed that even though one can achieve much higher polarization levels with TEMPOL concentrations increased to 20 and 40 mM, the polarization after dissolution led to lower enhancement factors. This is due to increased relaxation rates during the transfer and dissolution in samples with higher radical concentrations. On the other hand, using 5 mM TEMPOL led to lower enhancement factors because one cannot achieve good polarization levels in the polarizer with such a sample. Ultimately, this is a balancing act and based on our experience, samples with around 10 mM TEMPOL concentrations gave the pest performance.

4.6. Suggestions to improve the system

The preliminary results in the previous section show that the system is operational. One can perform several experiments per day for several weeks without any contamination or other problems. However, the modest enhancement factors, fast relaxation during transfer and detection, and broad and distorted peaks require the setup to be improved before it can be used routinely to study new systems.

A robust and efficient dissolution apparatus has the potential to drastically improve the setup. The bullet catcher tool is a first step but one has to build upon it to make sure all the hyperpolarized substrate is efficiently and rapidly extracted and is well mixed with the solvent. This can probably be achieved by adding a small intermediary container between the bullet catcher and the NMR tube. Everything can be mixed there and then injected into the NMR tube. Since the dissolution is taking place in the intermediary container, one can use smaller amounts of solvents and inject the final solution in a 5 mm instead of the currently used 10 mm NMR tube. Of course, this process has to be done as fast as possible to preserve the polarization as much as possible.

Another suggestion is to protect a larger fraction of the sample pathway with magnetic fields to maximize polarization preservation. Currently the distance between the polarizer and the spectrometer is covered by a magnetic tunnel and the data show that it has a positive effect on the final enhancement. However, there is at least one major low-field section in the pathway which is inside the polarizer. According to the specifications of the polarizer, about 1 m of the pathway inside the polarizer has a magnetic field below 0.1 T. Although technically challenging [2], if one can protect this section with a magnetic field, it would most probably enhance the

preservation of the polarization in the final state. In addition, any potential low-field section inside the bore of the spectrometer may be sheltered as well.

Finally, to get around the relaxation problems that emerge when transferring a solid sample, one could use photo-induced radicals to polarize the substrate. It has been shown that one can create non-persistent radicals by UV (ultraviolet-light) irradiation of a frozen sample containing pyruvic acid at 77 K [100-102]. These radicals can be used to polarize other nuclei in the sample. These radicals are annihilated if the sample temperature goes above about 190 K [100, 103]. Consequently, if the sample's temperature during the transfer goes above this temperature, the relaxation times would increase significantly since the radicals, which are the main source of relaxation, no longer exist in the sample.

4.7. Chapter conclusions

In this chapter, the different parts of the bullet-DNP system (apart from the probe that was already introduced in chapter 2) were presented. There is a unit that controls the pneumatic valves and the optical sensors. The permanent magnetic tunnel that connects the polarizer to the spectrometer helps to protect the polarization during the transfer. The specific procedure to insert the sample into the polarizer with the help of the sample insertion tool while preventing any contamination was discussed in detail. The importance of a robust dissolution system was also elaborated.

Even though the system has not achieved its best performance yet, the preliminary results show great promise. The best enhancement factor achieved until now is $\varepsilon \simeq 188$ which is a modest value but it serves as a proof that the system is working. I believe that by implementing the suggestions made in the previous section, the setup can be significantly improved.

Chapter 5

5. A direct NMR method to measure self-diffusion coefficients in liquids

5.1. Introduction

The translational self-diffusion coefficient (*D*) is an important transport parameter of molecules in liquids [6]. It can reveal chemical information such as molecular masses, aggregation states, or the association of different molecules [7]. There are two major methods to measure self-diffusion coefficients. Radioactive tracer techniques are the traditional way for such measurements. Although they can be very accurate, they suffer from challenging synthetic requirements, long measurement times that may be of the order of days or weeks for a single component, and inherent perturbations of the system under investigation due to isotope substitutions. On the other hand, nuclear magnetic resonance (NMR) techniques are capable of determining self-diffusion coefficients in moderate sample volumes, without isotopic labeling, usually in a matter of minutes [8].

The idea of measuring self-diffusion coefficients by NMR was started with Erwin Hahn's famous paper where he introduced spin echoes (SE) [21] and showed that, due to the inhomogeneity of the static magnetic field, self-diffusion causes an attenuation of echo signals in liquids. The spin echo method for measuring diffusion was further developed by Carr and Purcell [104]. McCall et al. [105] proposed the idea of applying time-dependent pulsed field gradients (PFGs) before and after (but not during) radio-frequency (rf) pulses. This idea was first applied to determine diffusion coefficients by Stejskal and Tanner [106]. Combinations of pulsed magnetic field gradients and spin echo (SE) experiments are referred to as pulsed gradient spin echo (PGSE) techniques. Spin echoes are not only attenuated by transverse (T_2) relaxation but also modulated by homonuclear scalar couplings. Therefore, PGSE techniques in their simplest form are not precise when the echo times needed to observe diffusion are long with respect to T_2 or $1/J$. This led to the idea of combining pulsed field gradients with stimulated echo methods [107], where

the signal is attenuated mainly by longitudinal relaxation (with a more favorable time constant $T_1 \geq T_2$) [108].

An alternative for measuring self-diffusion coefficients relies on the selective inversion of the magnetization of a slice and the observation of its recovery towards thermal equilibrium [109]. In the absence of diffusion, the result would be the same as in a classical non-selective inversion-recovery experiment. However, during the recovery, some of the inverted spins leave the slice while non-inverted spins enter the slice due to diffusion. Consequently, the recovery towards thermal equilibrium is accelerated. The self-diffusion coefficient can be derived from this deviation provided the slice is sufficiently thin. This method also has the advantage of being only marginally affected by T_2.

Here, we propose a direct way of measuring the coefficient of diffusion. The magnetization is inverted in a gradient-resolved slice that is selected perpendicular to a pulsed field gradient applied in one direction. Then, 1D images of that slice (along the direction of the selection gradient) are obtained after a variable diffusion delay. Diffusion coefficients are calculated by comparing the images at different diffusion times. Since diffusion mainly occurs while magnetization is longitudinal, this method also does not depend significantly on T_2. This technique offers a striking way to visualize diffusion because the spreading of the molecules can be observed clearly from one image to another. This is reminiscent of the spreading of a droplet of a dye in a solution, perhaps the most straightforward way of illustrating diffusive phenomena.

5.2. Experimental measurements and considerations

Controlling the experimental conditions during the tests, eliminating unwanted effects such as convection as much as possible, and accurate calibration of the temperature and gradients are important in order to obtain precise *D* values.

The precise calibration of the magnetic field gradient (*G*) is crucial for measuring diffusion by NMR. There are several methods for this purpose, such as the analysis of the shapes of spin echoes [110, 111] or the use of an intentional mismatch of gradient pulses [112]. The calibration with a sample with a precisely known *D* coefficient is a common procedure [113-115]. Using the latter, one has to be vigilant that the diffusion coefficient and the signal intensity of the reference sample should be similar to those of the sample of interest [6]. In the present work, calibration of the magnetic field gradient *G* is done by acquiring 1D images of objects with precisely known sizes and correlating the dimension of the image in frequency units to units of length.

Convection, caused by temperature gradients within the sample, is an important perturbation when measuring diffusion. Slow convection usually leads to an extra signal attenuation in pulsed field gradient (PFG) experiments, resulting in an overestimation of diffusion coefficients unless it is corrected for. Fast convection causes severe signal losses and phase and line shape anomalies [116]. The double-stimulated-echo (DSTE) [117] provides a reliable method to strongly attenuate the effects of convection in traditional experiments. Convection can also be limited by choosing an appropriate sample geometry. Here, the sample that was used for the diffusion

measurements was contained in a small spherical bulb (Figure 5.1a) inside a 5 mm NMR tube. It contains pure H_2O inside the bulb and pure D_2O outside (Figure 5.1b). No buffer to control the pH has been added. The idea is to prevent convection by restricting the volume for the measurements and separate the sample from the environment as much as possible.

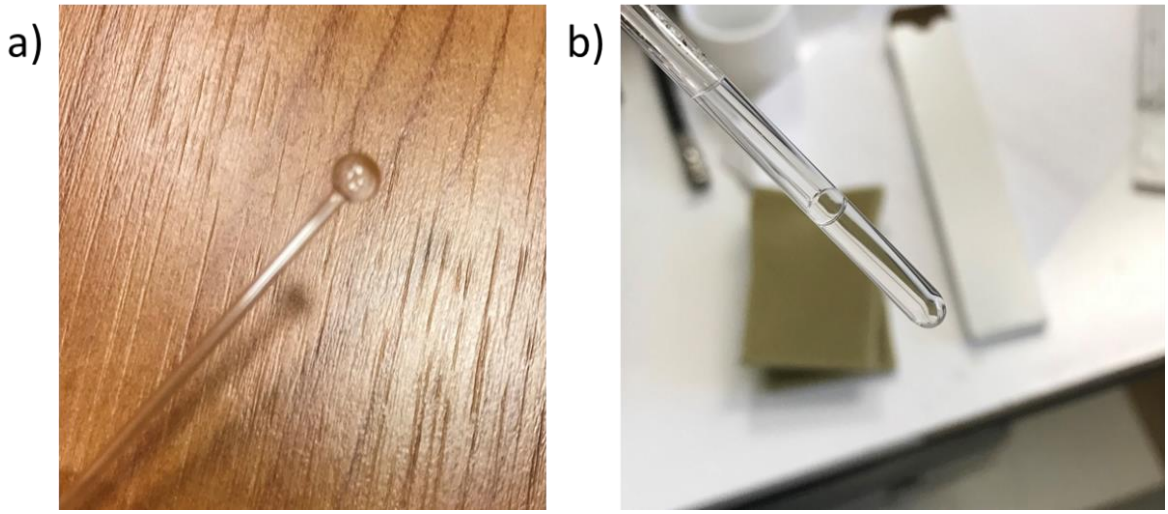

Figure 5.1- a) The empty spherical bulb with stem. b) A sample that is used for diffusion measurements with pure H_2O inside the bulb and pure D_2O outside. The volume of the bulb is approximately 18 µL.

Calibration of gradients is achieved by obtaining 1D images in three orthogonal directions. For *x* and *y* gradients, a concentric tube with a known diameter has been used, while for the *z* gradient a pair of O-rings separated by a precisely known distance has been employed. The temperature of the samples was calibrated by measuring the chemical shift differences of residual protons in a sample of 99.8% deuterated methanol [118].

All measurements were performed at 18.8 T (800 MHz proton frequency) on a Bruker spectrometer equipped with a 5 mm TXI probe with triple axes gradients. The pulse sequence used for determining the diffusion constants is shown in Figure 5.2.

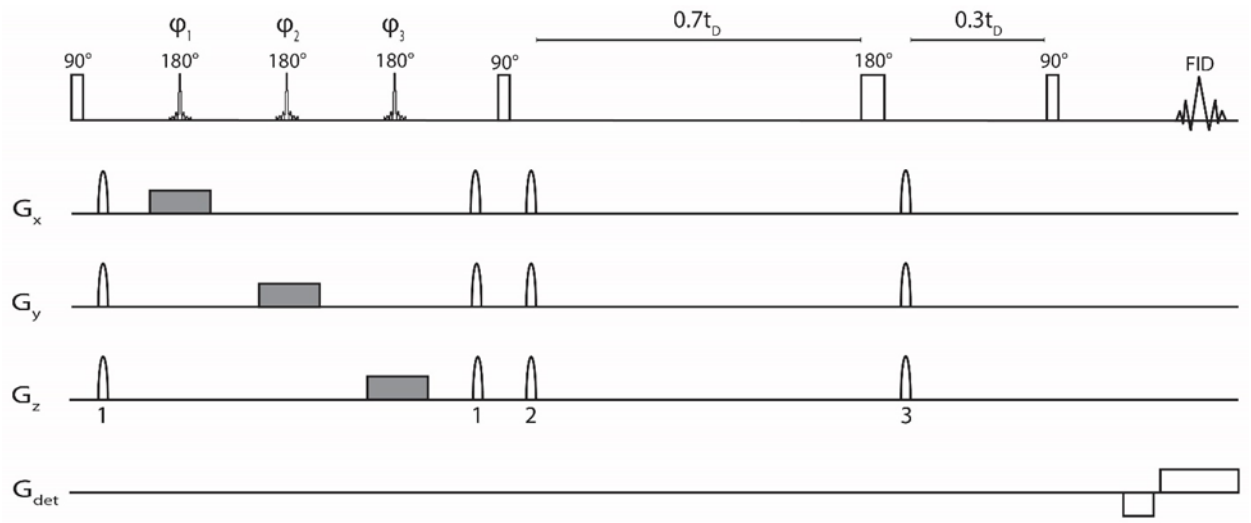

Figure 5.2- Pulse sequence used to select the magnetization in a selected volume and then acquire a 1D image of the projection of the voxel element along an arbitrarily chosen direction after a diffusion time t_D. First a non-selective 90° pulse brings the magnetization in the *xy* plane. A volume element is selected by three consecutive 180° refocusing pulses in the presence of three orthogonal gradients (grey rectangles). These gradients start before the beginning and finish after the end of the rf pulses. The selective 180° pulses are cycled independently as follows φ_1 = [*x*, *y*, *x*, *y*, *x*, *y*, *x*, *y*], φ_2 = [*x*, *x*, *y*, *y*, *x*, *x*, *y*, *y*], and φ_3 = [*x*, *x*, *x*, *x*, *y*, *y*, *y*, *y*], along with the receiver phase φ_{rec} = [*x*, -*x*, -*x*, *x*, -*x*, *x*, *x*, -*x*] to select signals stemming from a cubic voxel. In order to reduce further artifacts, the selection block is bracketed by a pair of two identical gradient pulses generated by a superposition of all three PFGs. The magnetization is brought back to the *z* direction by a second non-selective 90° pulse. During the diffusion delay t_D the magnetization will be attenuated by $\exp(-t_D/T_1)$. At the end of the sequence the magnetization is brought back to the transverse plane by a third non-selective 90° pulse, and a 1D projection along a specific axis of the chosen volume is obtained with a gradient echo. For very long diffusion delays, the magnetization that has grown back to equilibrium is dominant and in practice random subtraction artifacts remain. To limit the return to equilibrium, an inversion pulse, followed by purging gradients to de-phase undesirable transverse magnetization, is inserted at $7/10^{th}$ of the diffusion delay (this fraction has been chosen empirically). The direction of the detection gradient (G_{det}) can be chosen along any desired axis. δt_{det} is the distance between two adjacent data points during signal detection. The bandwidth during detection, which is equal to $1/\delta t_{det}$, needs to cover the frequency range induced by the G_{det}. The positions of G_x, G_y, and G_z can be arbitrarily permutated without changing the result.

After bringing the magnetization in the *xy* plane with a non-selective 90° radio-frequency (rf) pulse, the magnetization of a volume element is inverted three times by the combination of three sequential selective 180° pulses in the manner of point-resolved spectroscopy (PRESS) [119]. Selective 180° pulses with a Reburp profile [120] have been used. The gradients are switched on and off 1 ms before and 1 ms after the selective rf pulses. The magnetization is stored along *z* during the diffusion delay t_D before being rotated again into the *xy* plane. At the end of the sequence, a 1D projection along any desired axis of the inverted volume element is obtained with a gradient echo. Artifacts are removed by phase cycling, spoiler gradients, and an inversion of the magnetization at 70% of the duration of the diffusion delay (see figure caption for details). A 3D volume (instead of a slice of the entire sample) has been selected in order to avoid edge effects.

5.3. Theory

The distribution of the positions of particles that freely and isotropically diffuse in liquids can be described by the well-known self-diffusion equation

$$\frac{\partial P}{\partial t} = D\frac{\partial^2 P}{\partial \xi^2} \tag{5.1}$$

where D is the self-diffusion coefficient and P is the probability to find a molecule at position ξ (which in our experiments can be either x, y, or z) at time t. This equation can be solved [121] with boundary conditions

$$P(\xi, t) \to 0 \; as \; \xi \to \pm\infty$$

and

$P(\xi, 0) = \delta(\xi)$ (idealized sharp initial condition).

The solution of equation 5.1 for diffusion is:

$$P(\xi, t) = \frac{1}{\sqrt{4\pi D t}} \exp\left(-\frac{\xi^2}{4Dt}\right). \tag{5.2}$$

This equation can be re-written as a conditional probability that a molecule moves from an initial position ξ_0 at time t_0 to the position ξ at a later time t:

$$P'(\xi, \xi_0, t, t_0) = \frac{1}{\sqrt{4\pi D(t-t_0)}} \exp\left(-\frac{(\xi-\xi_0)^2}{4D(t-t_0)}\right). \tag{5.3}$$

As time increases, the width of the Gaussian probability distribution increases. For a given time, the width of this distribution is proportional to $\sqrt{D}$. For an arbitrary initial distribution of positions $Q(\xi_0, t_0)$, the distribution at a time t can be obtained by convolution of this distribution $Q(\xi_0, t_0)$ with $P'(\xi, \xi_0, t, t_0)$ of equation 5.3.

By acquiring a series of 1D images obtained in different directions depending on the choice of G_{det} in Figure 5.2 for different diffusion delays $t = t_D$, the broadening of the probability distribution described by equation 5.3 can be followed as a function of time. Convolution of an image obtained for an initial diffusion delay t_{D0} with equation 5.3, using the correct diffusion coefficient and a scaling factor to take into account T_1 relaxation, should match the experimental image registered at a later time t_D. To obtain the best fit for the diffusion coefficient D, instead of convoluting an image in real r space, the signal can be multiplied in k space (using the convolution theorem [122]) after Fourier transform of equation 5.3, which leads to another Gaussian function. The signal registered at the shortest diffusion delay (t_{D0}) is taken as the reference and multiplied with a Gaussian of the form:

$$f = A\exp\left(-\frac{(\xi-\xi_0)^2}{2B^2}\right). \tag{5.4}$$

A and B are parameters fitted to match the signal obtained at several later diffusion delays t_D.

The constant *A* only depends on the relaxation time T_1. It can be discarded in the further analysis. However, the standard deviation *B* is determined by *D* and the diffusion delays t_D.

After Fourier transforming equation 5.4, equalizing the argument of the exponential to the argument of the exponential in equation 5.3, and rearranging and substituting the different terms, one obtains the following equation:

$$B = \left(\frac{1}{\sqrt{2D}\gamma G_{det}\delta t_{det}}\right)\frac{1}{\sqrt{\Delta t_{dif}}}. \qquad (5.5)$$

Here, γ is the gyromagnetic ratio (usually of protons), G_{det} is the strength of the detection gradient, δt_{det} is the distance between two adjacent data points during signal detection, and $\Delta t_{dif} = t_D - t_{D0}$ is the difference between two diffusion delays.

5.4. Results and discussion

Images of a selected slice after diffusion times t_D varying from 1 ms to 9 s were recorded with the pulse sequence in Figure 5.2 for protons in a sample of H_2O. These experiments were done for projections G_{det} along the *x*, *y*, or *z* axis. Figure 5.3 shows representative 1D images along the *x* dimension (i.e., for $G_{det} = G_x$) for 4 different values of t_D.

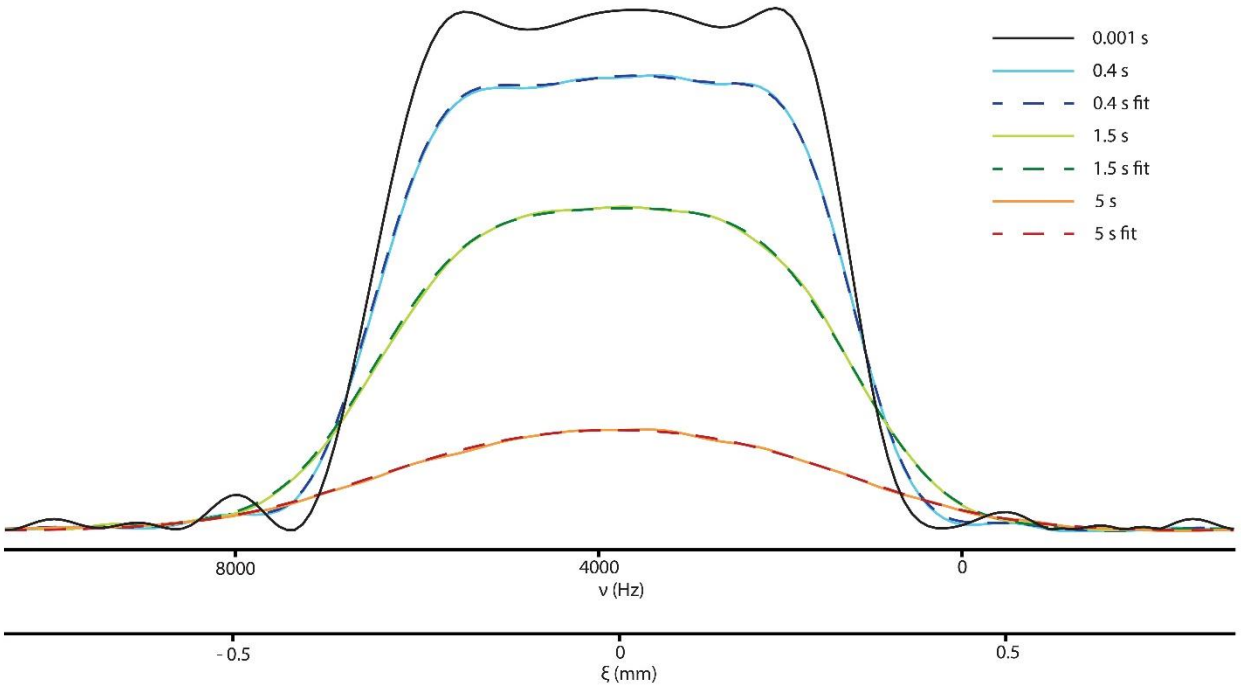

Figure 5.3- Slice images (i.e., 1D projections of our selected volume) of a spherical H_2O sample along the *x* direction after t_D = 0.001, 0.4, 1.5, and 5 s showing the spread of the molecules due to diffusion at *T* = 25 °C. The results of the fit as described in the main text are shown with dashed lines. Reburp pulse durations were 2 ms. Gradient strengths during slice selection and acquisition were 20% and 40% of the maximum gradient strength, respectively. The inner diameter of the spherical H_2O sample is *ca.* 3.2 mm, while the width of the selected slice is *ca.* 0.7 mm.

The effects of diffusion are readily grasped in Figure 5.3. For the smallest value of t_{D0} = 1 ms, the profile is very similar to the refocusing profile of the Reburp pulse. As t_D increases, the profile becomes wider and smoother which clearly shows the diffusion of the molecules. The intensity decreases not only due to diffusion (which keeps the surface constant) but also due to relaxation.

As set out in the theory section, one can obtain the self-diffusion coefficient D by comparing images with different diffusion delays t_D. The image at the shortest delay is chosen as the initial reference distribution. Then for all other delays, the best fit of the standard deviation B is obtained by multiplying the signal of the reference distribution with equation 5.4. For a given temperature and a given direction of the projections G_{det} along the x, y, or z axes, the diffusion coefficient has been obtained by a weighted fit of the standard deviation B versus $1/\sqrt{\Delta t_{dif}}$ (according to equation 5.5). The weighted fit takes into account the errors which are obtained from the diagonal of the covariance matrices for the Gaussian fit for each diffusion delay. Figure 5.4 shows a plot of B versus Δt_{dif} for one representative set of measurements for a gradient G_{det} = G_x at 25 °C. The results of the fit for t_D = 0.4, 1.5, and 5 s are shown in Figure 5.3 by dashed lines superimposed on the experimental data.

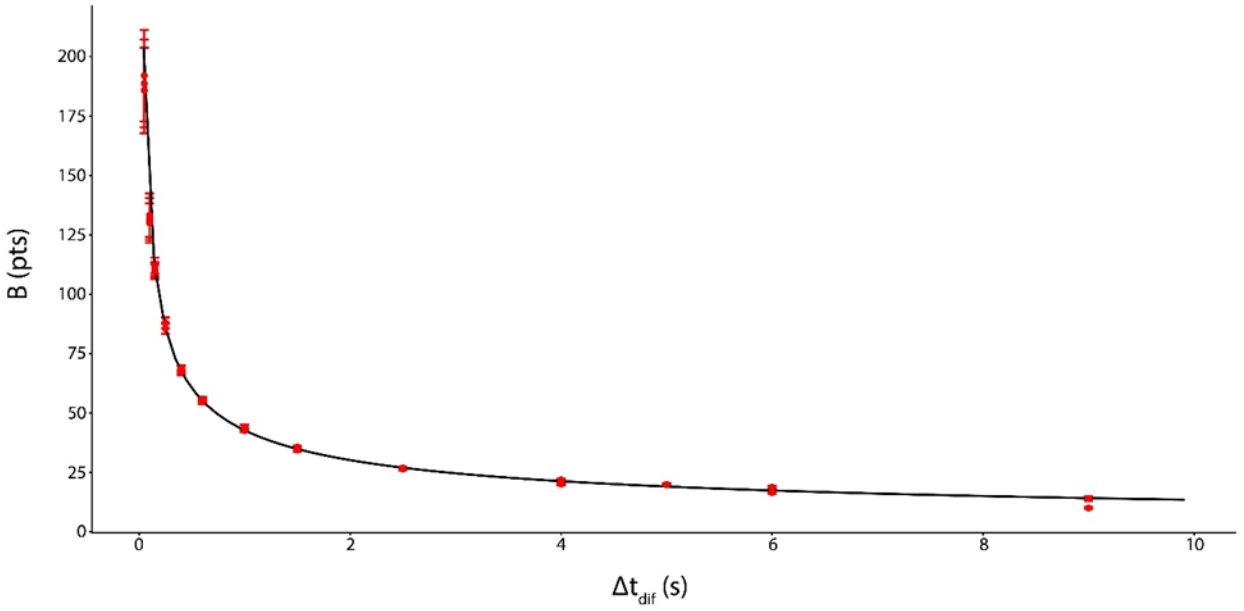

Figure 5.4- A plot of the standard deviation B (see equation 5.4) versus $\Delta t_{dif} = t_D - t_{D0}$ based on slice selection with a gradient $G_{det} = G_x$ at 25 °C. The continuous line shows the best fit according to equation 5.5, resulting in a diffusion constant of 2.552 x 10^{-9} $m^2.s^{-1}$.

The measurements at different diffusion delays have been repeated two or three times. The errors increase for long delays t_D (when the signal-to-noise ratio is low) and for very short delays when the molecules have not had the time to diffuse significantly (i.e., when the Gaussian function of equation 5.4 is very flat during the detection time which is equal to $N_{det}\delta t_{det}$, with N_{det} being the total number of complex detection points).

As previously mentioned, the most commonly used method for determining *D* relies on a preliminary calibration of the gradient strength with a sample of precisely known *D*-value. The *D*-values of samples of interest are then calculated based on the preliminary gradient calibration. We shall refer to this method as *self-reference*-calibration. Here, we calibrated *G* by acquiring 1D images of objects with precisely known distances and then attribute the size of the image in frequency units to the real distance in units of length. We shall call this method *image*-calibration. The benefit of the latter is that gradient calibration and diffusion measurements are independent of each other. Table 5.1 shows the *maximum* gradient strength values calculated with the two different methods and their differences.

Table 5.1- Maximum gradient strength calibration with the *self-reference* and the *image* methods and their differences.

	G_{image} (T.m^{-1})	$G_{self\text{-}reference}$ (T.m^{-1})	Difference (%)
G_x	0.499	0.525	5.2
G_y	0.505	0.534	5.7
G_z	0.667	0.710	6.4

The $G_{self\text{-}reference}$ values were calculated using one set of experiments at 25 °C, as shown in Figure 5.4 for each gradient direction and the *D*-value from Holz et al. [114] of 2.299 x 10^{-9} m^2.s^{-1} for water at 25 °C.

The diffusion constants using the gradient strengths G_{image} from the *image*-calibration method are significantly higher, as shown in Table 5.2. The maximum gradient strength corresponds to the strength of the gradient when the highest available gradient current is applied.

Table 5.2- Self-diffusion coefficient value of water at 25 °C obtained with the slice selection method described in Figure 5.2 by calibrating the gradient strengths by *image*-calibration, i.e., from objects of known geometry.

	$D/10^{-9}$ (m^2.s^{-1})
$G_{det} = G_x$	2.562 ± 0.007
$G_{det} = G_y$	2.595 ± 0.013
$G_{det} = G_z$	2.616 ± 0.009
Ref. [114]	2.299
Ref. [123]	2.36 ± 0.04
Ref. [113]	2.51 ± 0.01

The experimental errors in Table 5.2 come from the dispersion of 4 independent sets of measurements (each set containing 2 or 3 repetitions at 13 diffusion delays as shown in Figure 5.4). These errors are very small and are probably negligible compared to systematic errors that may be due to gradient non-linearities and calibration errors, or to errors in temperature control.

To demonstrate the feasibility of the proposed method for different liquids, complementary experiments were performed at different temperatures for H_2O and Dimethyl sulfoxide (DMSO).

The results for both *self-reference* and *image* methods for gradient calibration are shown in Table 5.3 alongside literature values for comparison. For these experiments, all images were recorded with $G_{det} = G_x$.

Table 5.3- Self-diffusion coefficients D of H_2O and DMSO at different temperatures. All images were recorded with $G_{det} = G_x$.

		This work using G_{image} calibration	This work using $G_{self\text{-}reference}$ calibration	Holz et al. [114] (error limits of < 1%)
Liquid	T (°C)	$D/10^{-9}$ ($m^2.s^{-1}$)	$D/10^{-9}$ ($m^2.s^{-1}$)	$D/10^{-9}$ ($m^2.s^{-1}$)
H_2O	15	1.965 ± 0.020	1.776 ± 0.020	1.766
	30	2.835 ± 0.020	2.562 ± 0.020	2.597
	40	3.554 ± 0.020	3.212 ± 0.020	3.222
DMSO	25	0.817 ± 0.020	0.738 ± 0.020	0.730
	35	0.987 ± 0.020	0.892 ± 0.020	0.889

The errors in Table 5.3 were estimated from the average errors reported in Table 5.2. Depending on the gradient calibration method (*self-reference* or *image* calibration), the diffusion coefficients D are either equal to those reported by Holz et al. [114] or consistently about 10% higher (note that the calculated value of the diffusion coefficient D depends on the square of the gradient strength).

5.5. Chapter conclusions

An alternative method of measuring self-diffusion coefficients (D) is proposed. The values of D obtained with this method are reproducible and consistent for different liquids at different temperatures. In addition to being almost independent of T_2, the method has the advantage to be direct and intuitive. The diffusion phenomenon can be observed and followed directly in one-dimensional images. Applications to restricted diffusion, extension of the method to separate different diffusing species, and the measurement of flow are prospective subjects that could be investigated in the near future.

Conclusions and perspectives

This dissertation contains two separate subjects. The largest part is about the design, production, and implementation of the bullet-DNP system. An efficient broadband double-resonance probe that has been especially developed for this system is described in detail and its capabilities are put to test by detecting NMR spectra of ^{1}H, ^{23}Na, ^{13}C, ^{2}H, and ^{17}O with direct polarization. In addition, ^{13}C and ^{17}O signals were also detected with cross polarization from ^{1}H. The observation of characteristic asymmetries in powder spectra of ^{2}H pushed us to further investigate the quadrupolar line shapes due to ^{2}H nuclei in a typical frozen DNP juice in order to determine the absolute spin polarization or, equivalently, the absolute spin temperature of the deuterium nuclei. The measurement of the spin temperature of other nuclei present in the DNP juice and comparing the values with the deuterium spin temperature T_{spin}(^{2}H) that is determined by our proposed method, could be an interesting next step, which could provide insights into the polarization mechanisms.

Apart from the probe, all other parts of the bullet-DNP system are described and the procedure to perform a complete experiment, starting from sample preparation and insertion until ejection, transfer, and detection in the spectrometer is discussed in detail. Several preliminary results showing hyperpolarized signals detected after dissolution are presented in this work. However, these results should primarily be considered as a proof-of-concept. The reproducibility of these results and the errors attributed to them need to be investigated further before inferring definitive conclusions. A few suggestions are made to improve the current system. These suggestions include building a robust and efficient dissolution apparatus, protect a larger fraction of the sample pathway with magnetic fields to maximize the preservation of the polarization, and to explore the possibility of using non-persisting radicals created by UV irradiation.

The second part of this thesis is about measuring self-diffusion coefficients in liquids. Traditionally, in NMR, self-diffusion coefficients are determined by detecting the attenuation of signals as a function of the gradient amplitude in gradient echo sequences. In this thesis, an alternative method is put forward in which the diffusion process is followed directly by recording 1D images of a selected slice at different intervals. In addition to being almost independent of T_2, this method has the advantage to be direct and intuitive and it results in diffusion coefficients that are consistent with earlier studies of H_2O and DMSO at different temperatures. A few examples of prospective subjects that could be investigated to continue this project are applications to restricted diffusion, extension of the method to separate different diffusing species, and the measurement of flow.

References

[1] J.H. Ardenkjær-Larsen, B. Fridlund, A. Gram, G. Hansson, L. Hansson, M.H. Lerche, R. Servin, M. Thaning, K. Golman, Increase in signal-to-noise ratio of > 10,000 times in liquid-state NMR, Proceedings of the National Academy of Sciences of the United States of America, 100 (2003) 10158.

[2] K. Kouřil, H. Kouřilová, S. Bartram, M.H. Levitt, B. Meier, Scalable dissolution-dynamic nuclear polarization with rapid transfer of a polarized solid, Nature Communications, 10 (2019) 1733.

[3] G. Bodenhausen, R. Freeman, D.L. Turner, Suppression of artifacts in two-dimensional *J* spectroscopy, Journal of Magnetic Resonance, 27 (1977) 511-514.

[4] J.R. Long, R. Ebelhäuser, R.G. Griffin, ^{2}H NMR Line Shapes and Spin−Lattice Relaxation in $Ba(ClO_3)_2{\cdot}2H_2O$, The Journal of Physical Chemistry A, 101 (1997) 988-994.

[5] O.W. Sørensen, G.W. Eich, M.H. Levitt, G. Bodenhausen, R.R. Ernst, Product operator formalism for the description of NMR pulse experiments, Progress in Nuclear Magnetic Resonance Spectroscopy, 16 (1984) 163-192.

[6] M. Holz, H. Weingartner, Calibration in accurate spin-echo self-diffusion measurements using ^{1}H and less-common nuclei, Journal of Magnetic Resonance, 92 (1991) 115-125.

[7] R. Evans, G. Dal Poggetto, M. Nilsson, G.A. Morris, Improving the Interpretation of Small Molecule Diffusion Coefficients, Analytical Chemistry, 90 (2018) 3987-3994.

[8] P. Stilbs, Fourier transform pulsed-gradient spin-echo studies of molecular diffusion, Progress in Nuclear Magnetic Resonance Spectroscopy, 19 (1987) 1-45.

[9] R. Frisch, O. Stern, Über die magnetische Ablenkung von Wasserstoffmolekülen und das magnetische Moment des Protons. I, Zeitschrift für Physik, 85 (1933) 4-16.

[10] I. Estermann, O. Stern, Über die magnetische Ablenkung von Wasserstoffmolekülen und das magnetische Moment des Protons. II, Zeitschrift für Physik, 85 (1933) 17-24.

[11] W. Gerlach, O. Stern, Der experimentelle Nachweis der Richtungsquantelung im Magnetfeld, Zeitschrift für Physik, 9 (1922) 349-352.

[12] E.D. Becker, A Brief History of Nuclear Magnetic Resonance, Analytical Chemistry, 65 (1993) 295A-302A.

[13] I.I. Rabi, J.R. Zacharias, S. Millman, P. Kusch, A New Method of Measuring Nuclear Magnetic Moment, Physical Review, 53 (1938) 318-318.

[14] J.M.B. Kellogg, I.I. Rabi, N.F. Ramsey, J.R. Zacharias, The Magnetic Moments of the Proton and the Deuteron. The Radiofrequency Spectrum of H_2 in Various Magnetic Fields, Physical Review, 56 (1939) 728-743.

[15] F. Bloch, W.W. Hansen, M. Packard, Nuclear Induction, Physical Review, 69 (1946) 127-127.

[16] F. Bloch, Nuclear Induction, Physical Review, 70 (1946) 460-474.

[17] F. Bloch, W.W. Hansen, M. Packard, The Nuclear Induction Experiment, Physical Review, 70 (1946) 474-485.

[18] E.M. Purcell, H.C. Torrey, R.V. Pound, Resonance Absorption by Nuclear Magnetic Moments in a Solid, Physical Review, 69 (1946) 37-38.

[19] E.L. Hahn, An Accurate Nuclear Magnetic Resonance Method for Measuring Spin-Lattice Relaxation Times, Physical Review, 76 (1949) 145-146.

[20] E.L. Hahn, Nuclear Induction Due to Free Larmor Precession, Physical Review, 77 (1950) 297-298.

[21] E.L. Hahn, Spin Echoes, Physical Review, 80 (1950) 580-594.

[22] R.R. Ernst, W.A. Anderson, Application of Fourier Transform Spectroscopy to Magnetic Resonance, Review of Scientific Instruments, 37 (1966) 93-102.

[23] W.P. Aue, E. Bartholdi, R.R. Ernst, Two-dimensional spectroscopy. Application to nuclear magnetic resonance, The Journal of Chemical Physics, 64 (1976) 2229-2246.

[24] J. Jeener, G. Alewaeters, “Pulse pair technique in high resolution NMR” a reprint of the historical 1971 lecture notes on two-dimensional spectroscopy, Progress in Nuclear Magnetic Resonance Spectroscopy, 94-95 (2016) 75-80.
[25] H. Friebolin, Basic one- and two-dimensional NMR spectroscopy, WILEY-VCH, Weinheim, 2011.
[26] J. Keeler, Understanding NMR spectroscopy, (2010).
[27] C.P. Slichter, Principles of magnetic resonance, Springer, Berlin; London, 2011.
[28] R.R. Ernst, G. Bodenhausen, A. Wokaun, Principles of nuclear magnetic resonance in one and two dimensions, Clarendon Press ; Oxford University Press, Oxford [Oxfordshire]; New York, 1987.
[29] M.H. Levitt, Spin dynamics : basics of nuclear magnetic resonance, John Wiley & Sons, Chichester, England; Hoboken, NJ, 2011.
[30] M.J. Duer, Introduction to solid-state NMR spectroscopy, Blackwell Science, Oxford, 2008.
[31] A.W. Overhauser, Polarization of Nuclei in Metals, Physical Review, 92 (1953) 411-415.
[32] T.R. Carver, C.P. Slichter, Experimental Verification of the Overhauser Nuclear Polarization Effect, Physical Review, 102 (1956) 975-980.
[33] A. Abragam, Overhauser Effect in Nonmetals, Physical Review, 98 (1955) 1729-1735.
[34] A. Abragam, W.G. Proctor, Une Nouvelle Methode De Polarisation Dynamique Des Noyaux Atomiques Dans Les Solide, Comptes rendus de l'Académie des Sciences, 246 (1958) 2253-2256.
[35] B.N. Provotorov, A quantum-statistical theory of cross relaxation, Soviet Physics JETP, 15 (1962) 611-614.
[36] B.N. Provotorov, Magnetic resonance saturation in crystals, Soviet Physics JETP, 14 (1962) 1126-1131.
[37] M. Borghini, Spin-Temperature Model of Nuclear Dynamic Polarization Using Free Radicals, Physical Review Letters, 20 (1968) 419-421.
[38] M. Borghini, Nuclear spin relaxation and dynamic polarization versus electron spin-spin relaxation, Physics Letters A, 26 (1968) 242-244.
[39] A. Abragam, M. Goldman, Principles of dynamic nuclear polarisation, Reports on Progress in Physics, 41 (1978) 395-467.
[40] C.F. Hwang, D.A. Hill, New Effect in Dynamic Polarization, Physical Review Letters, 18 (1967) 110-112.
[41] V.A. Atsarkin, Dynamic nuclear polarization: Yesterday, today, and tomorrow, Journal of Physics: Conference Series, 324 (2011) 012003.
[42] R.A. Wind, M.J. Duijvestijn, C. van der Lugt, A. Manenschijn, J. Vriend, Applications of dynamic nuclear polarization in ^{13}C NMR in solids, Progress in Nuclear Magnetic Resonance Spectroscopy, 17 (1985) 33-67.
[43] A.B. Barnes, G.D. Paëpe, P.C. van der Wel, K.N. Hu, C.G. Joo, V.S. Bajaj, M.L. Mak-Jurkauskas, J.R. Sirigiri, J. Herzfeld, R.J. Temkin, R.G. Griffin, High-Field Dynamic Nuclear Polarization for Solid and Solution Biological NMR, Applied Magnetic Resonance, 34 (2008) 237-263.
[44] D.A. Hall, D.C. Maus, G.J. Gerfen, S.J. Inati, L.R. Becerra, F.W. Dahlquist, R.G. Griffin, Polarization-enhanced NMR spectroscopy of biomolecules in frozen solution, Science, 276 (1997) 930-932.
[45] A.B. Barnes, B. Corzilius, M.L. Mak-Jurkauskas, L.B. Andreas, V.S. Bajaj, Y. Matsuki, M.L. Belenky, J. Lugtenburg, J.R. Sirigiri, R.J. Temkin, J. Herzfeld, R.G. Griffin, Resolution and polarization distribution in cryogenic DNP/MAS experiments, Physical Chemistry Chemical Physics, 12 (2010) 5861-5867.
[46] M. Rosay, L. Tometich, S. Pawsey, R. Bader, R. Schauwecker, M. Blank, P.M. Borchard, S.R. Cauffman, K.L. Felch, R.T. Weber, R.J. Temkin, R.G. Griffin, W.E. Maas, Solid-state dynamic nuclear polarization at 263 GHz: spectrometer design and experimental results, Physical Chemistry Chemical Physics, 12 (2010) 5850-5860.
[47] R.G. Griffin, T.F. Prisner, High field dynamic nuclear polarization—the renaissance, Physical Chemistry Chemical Physics, 12 (2010) 5737-5740.
[48] W. de Boer, Dynamic orientation of nuclei at low temperatures, Journal of Low Temperature Physics, 22 (1976) 185-212.

[49] D.G. Crabb, W. Meyer, Solid polarized targets for nuclear and particle physics experiments, Annual Review of Nuclear and Particle Science, 47 (1997) 67-109.
[50] M. Baudin, B. Vuichoud, A. Bornet, G. Bodenhausen, S. Jannin, A cryogen-consumption-free system for dynamic nuclear polarization at 9.4 T, Journal of Magnetic Resonance, 294 (2018) 115-121.
[51] L. Lumata, Z. Kovacs, A.D. Sherry, C. Malloy, S. Hill, J. van Tol, L. Yu, L. Song, M.E. Merritt, Electron spin resonance studies of trityl OX063 at a concentration optimal for DNP, Physical Chemistry Chemical Physics, 15 (2013) 9800-9807.
[52] E.M.M. Weber, G. Sicoli, H. Vezin, G. Frébourg, D. Abergel, G. Bodenhausen, D. Kurzbach, Sample Ripening through Nanophase Separation Influences the Performance of Dynamic Nuclear Polarization, Angewandte Chemie International Edition, 57 (2018) 5171-5175.
[53] J. Wolber, F. Ellner, B. Fridlund, A. Gram, H. Jóhannesson, G. Hansson, L.H. Hansson, M.H. Lerche, S. Månsson, R. Servin, M. Thaning, K. Golman, J.H. Ardenkjær-Larsen, Generating highly polarized nuclear spins in solution using dynamic nuclear polarization, Nuclear Instruments and Methods in Physics Research Section A: Accelerators, Spectrometers, Detectors and Associated Equipment, 526 (2004) 173-181.
[54] J.H. Ardenkjaer-Larsen, S. Macholl, H. Jóhannesson, Dynamic Nuclear Polarization with Trityls at 1.2 K, Applied Magnetic Resonance, 34 (2008) 509-522.
[55] A. Bornet, S. Jannin, Optimizing dissolution dynamic nuclear polarization, Journal of Magnetic Resonance, 264 (2016) 13-21.
[56] A. Bornet, J. Milani, B. Vuichoud, A.J. Perez Linde, G. Bodenhausen, S. Jannin, Microwave frequency modulation to enhance Dissolution Dynamic Nuclear Polarization, Chemical Physics Letters, 602 (2014) 63-67.
[57] J. Milani, B. Vuichoud, A. Bornet, P. Mieville, R. Mottier, S. Jannin, G. Bodenhausen, A magnetic tunnel to shelter hyperpolarized fluids, Review of Scientific Instruments, 86 (2015) 024101.
[58] B. Aghelnejad, G. Bodenhausen, S. Marhabaie, A Low-Temperature Broadband NMR Probe for Multinuclear Cross-Polarization, ChemPhysChem, 20 (2019) 2830-2835.
[59] S. Jannin, A. Bornet, S. Colombo, G. Bodenhausen, Low-temperature cross polarization in view of enhancing dissolution Dynamic Nuclear Polarization in NMR, Chemical Physics Letters, 517 (2011) 234-236.
[60] M. Batel, M. Krajewski, A. Däpp, A. Hunkeler, B.H. Meier, S. Kozerke, M. Ernst, Dissolution dynamic nuclear polarization efficiency enhanced by Hartmann–Hahn cross polarization, Chemical Physics Letters, 554 (2012) 72-76.
[61] J.M.O. Vinther, V. Zhurbenko, M.M. Albannay, J.H. Ardenkjær-Larsen, Design of a local quasi-distributed tuning and matching circuit for dissolution DNP cross polarization, Solid State Nuclear Magnetic Resonance, 102 (2019) 12-20.
[62] J. Milani, B. Vuichoud, A. Bornet, R. Melzi, S. Jannin, G. Bodenhausen, Hyperpolarization of nitrogen-15 nuclei by cross polarization and dissolution dynamic nuclear polarization, Review of Scientific Instruments, 88 (2017) 015109.
[63] A.J. Perez Linde, A. Bornet, J. Milani, B. Vuichoud, R. Melzi, S. Jannin, G. Bodenhausen, Cross polarization from ^{1}H to quadrupolar ^{6}Li nuclei for dissolution DNP, Physical Chemistry Chemical Physics, 16 (2014) 24813-24817.
[64] A. Bornet, R. Melzi, S. Jannin, G. Bodenhausen, Cross Polarization for Dissolution Dynamic Nuclear Polarization Experiments at Readily Accessible Temperatures $1.2 < T < 4.2$ K, Applied Magnetic Resonance, 43 (2012) 107-117.
[65] A. Bornet, A. Pinon, A. Jhajharia, M. Baudin, X. Ji, L. Emsley, G. Bodenhausen, J.H. Ardenkjaer-Larsen, S. Jannin, Microwave-gated dynamic nuclear polarization, Physical Chemistry Chemical Physics, 18 (2016) 30530-30535.

[66] S. Hediger, B.H. Meier, N.D. Kurur, G. Bodenhausen, R.R. Ernst, NMR cross polarization by adiabatic passage through the Hartmann—Hahn condition (APHH), Chemical Physics Letters, 223 (1994) 283-288.
[67] S. Jannin, A. Bornet, R. Melzi, G. Bodenhausen, High field dynamic nuclear polarization at 6.7 T: Carbon-13 polarization above 70% within 20 min, Chemical Physics Letters, 549 (2012) 99-102.
[68] S. Schäublin, A. Höhener, R.R. Ernst, Fourier spectroscopy of nonequilibrium states, application to CIDNP, overhauser experiments and relaxation time measurements, Journal of Magnetic Resonance, 13 (1974) 196-216.
[69] J. Tropp, Multiplet Asymmetry and Multi-Spin Order in Liquid-State NMR Spectra of Hyperpolarized Compounds, Proceedings of the International Society for Magnetic Resonance in Medicine, 18 (2010) 1026.
[70] J.Y.C. Lau, A.P. Chen, Y.-P. Gu, C.H. Cunningham, A calibration-based approach to real-time in vivo monitoring of pyruvate C_1 and C_2 polarization using the J_{CC} spectral asymmetry, NMR in Biomedicine, 26 (2013) 1233-1241.
[71] B. Vuichoud, J. Milani, Q. Chappuis, A. Bornet, G. Bodenhausen, S. Jannin, Measuring absolute spin polarization in dissolution-DNP by Spin PolarimetrY Magnetic Resonance (SPY-MR), Journal of Magnetic Resonance, 260 (2015) 127-135.
[72] P. Kuhns, O. Gonen, J.S. Waugh, Proton spin-spin and spin-lattice relaxation in $CaSO_4 \cdot xH_2O$ below 1 K, Journal of Magnetic Resonance, 82 (1989) 231-237.
[73] D. Mammoli, N. Salvi, J. Milani, R. Buratto, A. Bornet, A.A. Sehgal, E. Canet, P. Pelupessy, D. Carnevale, S. Jannin, G. Bodenhausen, Challenges in preparing, preserving and detecting *para*-water in bulk: overcoming proton exchange and other hurdles, Physical Chemistry Chemical Physics, 17 (2015) 26819-26827.
[74] A. Abragam, M. Chapellier, J.F. Jacquinot, M. Goldman, Absorption lineshape of highly polarized nuclear spin systems, Journal of Magnetic Resonance, 10 (1973) 322-346.
[75] C.M. Edwards, D. Zhou, N.S. Sullivan, Unusual low-temperature effects on the NMR line shapes in solid hydrogen, Physical Review B, 34 (1986) 6540-6542.
[76] J.S. Waugh, O. Gonen, P. Kuhns, Fourier transform NMR at low temperatures, The Journal of Chemical Physics, 86 (1987) 3816-3818.
[77] D. Carnevale, S.E. Ashbrook, G. Bodenhausen, Solid-state NMR measurements and DFT calculations of the magnetic shielding tensors of protons of water trapped in barium chlorate monohydrate, RSC Advances, 4 (2014) 56248-56258.
[78] D. Carnevale, S. Chinthalapalli, G. Bodenhausen, Exciting Wide NMR Spectra of Static Solid Samples with Weak Radiofrequency Fields, Zeitschrift für Physikalische Chemie, 231 (2017) 527-543.
[79] D. Carnevale, P. Pelupessy, G. Bodenhausen, Cross-term Splittings Due to the Orientational Inequivalence of Proton Magnetic Shielding Tensors: Do Water Molecules Trapped in Crystals Hop or Tunnel?, The Journal of Physical Chemistry Letters, 10 (2019) 3224-3231.
[80] D. Carnevale, S. Marhabaie, P. Pelupessy, G. Bodenhausen, Orientation-Dependent Proton Relaxation of Water Molecules Trapped in Solids: Crystallites with Long-Lived Magnetization, The Journal of Physical Chemistry A, 123 (2019) 9763-9769.
[81] P.M. Andersen, N.S. Sullivan, M. Rall, J.P. Brison, Asymmetry of field-perturbed NQR spectra: A new ultra-low temperature thermometer?, Physica B: Condensed Matter, 169 (1991) 453-454.
[82] J.A. Marohn, P.J. Carson, J.Y. Hwang, M.A. Miller, D.N. Shykind, D.P. Weitekamp, Optical Larmor Beat Detection of High-Resolution Nuclear Magnetic Resonance in a Semiconductor Heterostructure, Physical Review Letters, 75 (1995) 1364-1367.
[83] N.N. Kuzma, P. Håkansson, M. Pourfathi, R.K. Ghosh, H. Kara, S.J. Kadlecek, G. Pileio, M.H. Levitt, R.R. Rizi, Lineshape-based polarimetry of dynamically-polarized $^{15}N_2O$ in solid-state mixtures, Journal of Magnetic Resonance, 234 (2013) 90-94.

[84] T. Sugishita, Y. Matsuki, T. Fujiwara, Absolute ^{1}H polarization measurement with a spin-correlated component of magnetization by hyperpolarized MAS-DNP solid-state NMR, Solid State Nuclear Magnetic Resonance, 99 (2019) 20-26.
[85] B. Aghelnejad, S. Marhabaie, M. Baudin, G. Bodenhausen, D. Carnevale, Spin Thermometry: A Straightforward Measure of Millikelvin Deuterium Spin Temperatures Achieved by Dynamic Nuclear Polarization, The Journal of Physical Chemistry Letters, (2020) 3219-3225.
[86] B. Meier, J.-N. Dumez, G. Stevanato, J.T. Hill-Cousins, S.S. Roy, P. Håkansson, S. Mamone, R.C.D. Brown, G. Pileio, M.H. Levitt, Long-Lived Nuclear Spin States in Methyl Groups and Quantum-Rotor-Induced Polarization, Journal of the American Chemical Society, 135 (2013) 18746-18749.
[87] S. Chinthalapalli, A. Bornet, D. Carnevale, S. Jannin, G. Bodenhausen, Homonuclear decoupling for spectral simplification of carbon-13 enriched molecules in solution-state NMR enhanced by dissolution DNP, Physical Chemistry Chemical Physics, 18 (2016) 11480-11487.
[88] M. Bak, J.T. Rasmussen, N.C. Nielsen, SIMPSON: A General Simulation Program for Solid-State NMR Spectroscopy, Journal of Magnetic Resonance, 147 (2000) 296-330.
[89] S.K. Zaremba, Good lattice points, discrepancy, and numerical integration, Annali di Matematica Pura ed Applicata, 73 (1966) 293-317.
[90] H. Conroy, Molecular Schrödinger Equation. VIII. A New Method for the Evaluation of Multidimensional Integrals, The Journal of Chemical Physics, 47 (1967) 5307-5318.
[91] V.B. Cheng, H.H. Suzukawa, M. Wolfsberg, Investigations of a nonrandom numerical method for multidimensional integration, The Journal of Chemical Physics, 59 (1973) 3992-3999.
[92] M. Edén, Computer simulations in solid-state NMR. III. Powder averaging, Concepts in Magnetic Resonance Part A, 18A (2003) 24-55.
[93] G. Bodenhausen, H. Kogler, R.R. Ernst, Selection of coherence-transfer pathways in NMR pulse experiments, Journal of Magnetic Resonance, 58 (1984) 370-388.
[94] D. Carnevale, V. Vitzthum, O. Lafon, J. Trébosc, J.-P. Amoureux, G. Bodenhausen, Broadband excitation in solid-state NMR of paramagnetic samples using Delays Alternating with Nutation for Tailored Excitation ('Para-DANTE'), Chemical Physics Letters, 553 (2012) 68-76.
[95] D. Carnevale, A.J. Perez Linde, G. Bauer, G. Bodenhausen, Solid-state proton NMR of paramagnetic metal complexes: DANTE spin echoes for selective excitation in inhomogeneously broadened lines, Chemical Physics Letters, 580 (2013) 172-178.
[96] M. Chan-Huot, S. Wimperis, C. Gervais, G. Bodenhausen, L. Duma, Deuterium MAS NMR Studies of Dynamics on Multiple Timescales: Histidine and Oxalic Acid, ChemPhysChem, 16 (2015) 204-215.
[97] D. Guarin, S. Marhabaie, A. Rosso, D. Abergel, G. Bodenhausen, K.L. Ivanov, D. Kurzbach, Characterizing Thermal Mixing Dynamic Nuclear Polarization via Cross-Talk between Spin Reservoirs, The Journal of Physical Chemistry Letters, 8 (2017) 5531-5536.
[98] F. Jähnig, A. Himmler, G. Kwiatkowski, A. Däpp, A. Hunkeler, S. Kozerke, M. Ernst, A spin-thermodynamic approach to characterize spin dynamics in TEMPO-based samples for dissolution DNP at 7 T field, Journal of Magnetic Resonance, 303 (2019) 91-104.
[99] A. Dupre, Miniaturised NMR sensor, 2012.
[100] A. Capozzi, T. Cheng, G. Boero, C. Roussel, A. Comment, Thermal annihilation of photo-induced radicals following dynamic nuclear polarization to produce transportable frozen hyperpolarized ^{13}C-substrates, Nature Communications, 8 (2017) 15757.
[101] T.R. Eichhorn, Y. Takado, N. Salameh, A. Capozzi, T. Cheng, J.-N. Hyacinthe, M. Mishkovsky, C. Roussel, A. Comment, Hyperpolarization without persistent radicals for in vivo real-time metabolic imaging, Proceedings of the National Academy of Sciences, 110 (2013) 18064.
[102] A. Capozzi, J.-N. Hyacinthe, T. Cheng, T.R. Eichhorn, G. Boero, C. Roussel, J.J. van der Klink, A. Comment, Photoinduced Nonpersistent Radicals as Polarizing Agents for X-Nuclei Dissolution Dynamic Nuclear Polarization, The Journal of Physical Chemistry C, 119 (2015) 22632-22639.

[103] M.I. Guzmán, A.J. Colussi, M.R. Hoffmann, Photogeneration of Distant Radical Pairs in Aqueous Pyruvic Acid Glasses, The Journal of Physical Chemistry A, 110 (2006) 931-935.
[104] H.Y. Carr, E.M. Purcell, Effects of Diffusion on Free Precession in Nuclear Magnetic Resonance Experiments, Physical Review, 94 (1954) 630-638.
[105] D.W. McCall, D.C. Douglass, E.W. Anderson, Self-Diffusion Studies by Means of Nuclear Magnetic Resonance Spin-Echo Techniques, Berichte der Bunsengesellschaft für physikalische Chemie, 67 (1963) 336-340.
[106] E.O. Stejskal, J.E. Tanner, Spin Diffusion Measurements: Spin Echoes in the Presence of a Time-Dependent Field Gradient, The Journal of Chemical Physics, 42 (1965) 288-292.
[107] J.E. Tanner, Use of the Stimulated Echo in NMR Diffusion Studies, The Journal of Chemical Physics, 52 (1970) 2523-2526.
[108] D. Burstein, Stimulated echoes: Description, applications, practical hints, Concepts in Magnetic Resonance, 8 (1996) 269-278.
[109] S. Leclerc, G. Trausch, J.M. Escanyé, D. Canet, NMR measurement of self-diffusion coefficients by slice selection, The Journal of Chemical Physics, 121 (2004) 405-408.
[110] J.S. Murday, Measurement of magnetic field gradient by its effect on the NMR free induction decay, Journal of Magnetic Resonance, 10 (1973) 111-120.
[111] D.M. Lamb, P.J. Grandinetti, J. Jonas, Fixed field gradient NMR diffusion measurements using bessel function fits to the spin-echo signal, Journal of Magnetic Resonance, 72 (1987) 532-539.
[112] M.I. Hrovat, C.G. Wade, Absolute measurements of diffusion coefficients by pulsed nuclear magnetic resonance, The Journal of Chemical Physics, 73 (1980) 2509-2510.
[113] N.J. Trappeniers, C.J. Gerritsma, P.H. Oosting, The self-diffusion coefficient of water, at 25°C, by means of spin-echo technique, Physics Letters, 18 (1965) 256-257.
[114] M. Holz, S.R. Heil, A. Sacco, Temperature-dependent self-diffusion coefficients of water and six selected molecular liquids for calibration in accurate ^{1}H NMR PFG measurements, Physical Chemistry Chemical Physics, 2 (2000) 4740-4742.
[115] K. Krynicki, C.D. Green, D.W. Sawyer, Pressure and temperature dependence of self-diffusion in water, Faraday Discussions of the Chemical Society, 66 (1978) 199-208.
[116] P. Kiraly, I. Swan, M. Nilsson, G.A. Morris, Improving accuracy in DOSY and diffusion measurements using triaxial field gradients, Journal of Magnetic Resonance, 270 (2016) 24-30.
[117] A. Jerschow, N. Müller, Suppression of Convection Artifacts in Stimulated-Echo Diffusion Experiments. Double-Stimulated-Echo Experiments, Journal of Magnetic Resonance, 125 (1997) 372-375.
[118] M. Findeisen, T. Brand, S. Berger, A ^{1}H-NMR thermometer suitable for cryoprobes, Magnetic Resonance in Chemistry, 45 (2007) 175-178.
[119] P.A. Bottomley, Spatial Localization in NMR Spectroscopy in Vivo, Annals of the New York Academy of Sciences, 508 (1987) 333-348.
[120] H. Geen, R. Freeman, Band-selective radiofrequency pulses, Journal of Magnetic Resonance, 93 (1991) 93-141.
[121] R. Metzler, J. Klafter, The random walk's guide to anomalous diffusion: a fractional dynamics approach, Physics Reports, 339 (2000) 1-77.
[122] R.N. Bracewell, The Fourier transform and its applications, Second edition. New York: McGraw-Hill, 1978.
[123] C.R. Becker, L.R. Schad, W.J. Lorenz, Measurement of diffusion coefficients using a quick echo split NMR imaging technique, Magnetic Resonance Imaging, 12 (1994) 1167-1174.

RÉSUMÉ

La spectroscopie par résonance magnétique nucléaire (RMN) est une technique universelle qui a la capacité de caractériser une grande variété de molécules et qui peut donner un aperçu de processus chimiques. Cependant, cette méthode spectroscopique souffre d'un manque de sensibilité. La polarisation nucléaire dynamique par dissolution (d-DNP) fait actuellement l'objet de nombreux développements pour augmenter la sensibilité de la RMN.

Les sondes d-DNP sont généralement conçues pour un ou deux noyaux spécifiques. L'étude de plusieurs différentes noyaux nécessite généralement la fabrication de multiples sondes coûteuses. De plus, le changement de sonde est un processus chronophage puisque le système fonctionnant à basse température (généralement entre 1,2 et 4,2 K) doit être réchauffé, augmentant en plus les risques de contamination. Ici, une sonde est décrite pour la d-DNP, conçue non seulement pour l'observation directe d'une large gamme de noyaux S tels que ^{1}H, ^{13}C, ^{2}H, ^{23}Na et ^{17}O, mais également pour la polarisation croisée entre $I = {}^{1}$H et divers noyaux S. Contrairement à la plupart des sondes conventionnelles, les circuits d'accord et d'adaptation sont partiellement immergés dans l'hélium superfluide à des températures allant jusqu'à 1,2 K. Des champs de radiofréquence (rf) intenses avec des amplitudes de l'ordre de 50 kHz peuvent être appliqués simultanément aux noyaux I et S utilisant des amplificateurs rf d'une puissance de l'ordre de 90 W.

Cette sonde est idéalement conçue pour la « DNP par projectile » qui est une nouvelle méthode pour transporter l'échantillon du polarisateur au spectromètre. Dans ce procédé, un échantillon polarisé est transféré à l'état solide, puis dissous après le transfert, plutôt que d'être dissous dans le polariseur, comme dans la configuration DNP de dissolution conventionnelle. La « DNP par projectile » a l'avantage de réduire considérablement le facteur de dilution et offre la possibilité d'utiliser des solvants organiques pour la dissolution. Cette méthode a été développée avec un insert qui évite la contamination, une éjection rapide de l'échantillon, la construction d'un tunnel magnétique avec un champ homogène proche de 0,34 T pour préserver la polarisation lors du transfert de l'échantillon, et le début de l'assemblage d'un système de dissolution efficace pour dissoudre les projectiles avec des quantités réglables de liquide dans l'alésage de l'aimant du spectromètre.

La polarisation nucléaire dynamique des échantillons à basses températures, généralement entre 1,2 et 4,2 K, permet d'atteindre des températures de spin aussi basses que 2 mK. Dans ces conditions, l'approximation à haute température est violée pour l'interaction nucléaire Zeeman. Cela conduit à des asymétries caractéristiques dans les spectres de poudre. Nous montrons que les formes des spectres dues aux couplages quadrupolaires des spins de deutérium qui sont présents dans pratiquement tous les solvants utilisés pour de telles expériences (‘sauce pour la DNP’) permettent la détermination rapide mais précise de la température de spin du deutérium ou, de manière équivalente, de la polarisation du deutérium. L'observation des échos quadrupolaires excités par des impulsions aux petits angles de nutation permet de surveiller l'accumulation et la décroissance de la polarisation positive ou négative du deutérium.

La RMN est établie comme l'une des méthodes les plus efficaces pour la mesure du coefficient d'auto-diffusion (D), qui est une propriété de transport importante des molécules dans les liquides. Une méthode alternative est proposée comme preuve de concept dans laquelle le processus de diffusion est suivi directement par l'enregistrement d'images 1D à différents intervalles. Bien que cette méthode ne soit pas destinée à remplacer les méthodes établies de la mesure de la diffusion, elle exploite une idée simple qui aboutit à des coefficients de diffusion cohérents obtenus à différentes températures pour H_2O et DMSO.

MOTS CLÉS

D-DNP, RMN, Diffusion, Thermométrie de spin, Polarisation croisée, Transfert d'échantillons hyperpolarisés solides

ABSTRACT

Nuclear magnetic resonance (NMR) spectroscopy is a powerful technique that has the capability to characterize a wide variety of molecules and can give insights into chemical processes. However, this spectroscopic method suffers from a lack of sensitivity. Dissolution dynamic nuclear polarization (d-DNP) is currently at the core of many new developments in view of boosting the sensitivity of NMR.

D-DNP probes are usually designed for one or at most two specific nuclei. Investigations of multiple nuclei usually requires manufacturing a number of costly probes. In addition, changing the probe is a time-consuming process since a system that works at low temperatures (usually between 1.2 and 4.2 K) must be warmed up, thus increasing the risks of contamination. Here, an efficient apparatus is described for d-DNP, designed not only for microwave-enhanced direct observation of a wide range of nuclei S such as ^{1}H, ^{13}C, ^{2}H, ^{23}Na, and ^{17}O, but also for cross-polarization (CP) from $I = {}^{1}$H to such S nuclei. Unlike most conventional designs, the tuning and matching circuits are partly immersed in superfluid helium at temperatures down to 1.2 K. Intense radio-frequency (rf) fields with amplitudes on the order of 50 kHz or better can be applied simultaneously to both nuclei I and S using rf amplifiers with powers on the order of 90 W.

This probe is ideally made for “bullet-DNP” which is a new d-DNP method that has recently been gaining importance. In this method, a polarized sample is transferred to a spectrometer in the solid state and dissolved after the transfer, rather than being dissolved in the polarizer, as in conventional dissolution DNP. The bullet-DNP setup has the advantage of significantly decreasing the dilution factor and provides the possibility to use organic solvents for dissolution. This setup is developed further with the development of a contamination-free insert and fast ejection of the sample, the construction of a magnetic tunnel with a homogeneous field near 0.34 T to preserve the polarization during the transfer of the solid sample from the polarizer to the spectrometer, and the beginning of the assembly of an efficient dissolution system to dissolve the bullets with adjustable amounts of liquid in the bore of the spectrometer magnet.

Dynamic nuclear polarization of samples at low temperatures, typically between 1.2 and 4.2 K, allows one to achieve spin temperatures as low as 2 mK, so that for many nuclear isotopes the high-temperature approximation is violated for the nuclear Zeeman interaction. This leads to characteristic asymmetries in powder spectra. We show that the line shapes due to the quadrupolar couplings of deuterium spins present in virtually all solvents used for such experiments (‘DNP juice’) allows the quick yet accurate determination of the deuterium spin temperature or, equivalently, the deuterium polarization. The observation of quadrupolar echoes excited by small flip-angle pulses allows one to monitor the build-up and decay of the positive or negative deuterium polarization.

NMR is established as one of the most potent methods of measuring self-diffusion coefficients (D) which is an important transport property of molecules in liquids. An alternative method is put forward as a proof of concept in which the diffusion process is followed directly by recording 1D images at different intervals. While this method is not meant to replace established methods of measuring diffusion, it exploits a simple idea which results in consistent diffusion coefficients obtained at different temperatures for H_2O and DMSO.

KEYWORDS

D-DNP, NMR, Diffusion, Spin thermometry, Cross polarization, Transfer of solid hyperpolarized samples